ISSN 1068-3755, Surface Engineering and Applied Electrochemistry, 2007, Vol. 43, No. 1, pp. 1–10. © Allerton Press, Inc., 2007.
Original Russian Text © A.I. Dikusar, I.A. Ivanenkov, B.P. Saushkin, S.A. Silkin, S.P. Yushchenko, 2007, published in Elektronnaya Obrabotka Materialov, 2007, Vol. 43, No. 1, pp. 4–15.

ELECTRICAL SIZING OF MATERIALS

High-Speed Anode Dissolution of Heat-Resistant Chrome–Nickel Alloys Containing Tungsten and Rhenium: I. Chloride Solutions

A. I. Dikusar[a, b], I. A. Ivanenkov[c], B. P. Saushkin[c], S. A. Silkin[b], and S. P. Yushchenko[a, b]

[a] *Institute of Applied Physics, Academy of Sciences of Moldova, ul. Akademiei 5, Chisinau, MD-2028 Moldova*
[b] *Pridnestrovskii Shevchenko Gos. University, ul. 25 Oktyabrya 128, Tiraspol', Moldova*
[c] *MATI–RGTU Tsiolkovskii Russian State University of Technology, Berezhkovskaya nab. 14, Moscow, 109240 Russia*

Received October 26, 2006

Abstract—The results of a study on the anode dissolution of two heat-resistant chrome–nickel alloys containing tungsten (12 wt %) as well as tungsten and rhenium (8 wt % of W and 6 wt % of Re) are described. The experiments took place in 2 M NaCl at a current density of up to 40 μ/cm^2 using a rotating disk electrode. It is shown that the alloy with the greater tungsten content dissolves at a lower rate (due to the formation and accumulation of insoluble oxides layers on the surface) and at a current density lower than the maximum anode current density for the basic component (nickel, and, probably, cobalt) of the anodic dissolution. Transpassive dissolution takes place under conditions of thermokinetic instability of the electrode process. In this case, a decreasing dependence of the current efficiency on the current density is observed, and the dissolution rate is independent of the tungsten concentration in the alloy. In the region of the maximum anode currents and the transition from one area of dissolution to another, abnormal anode dissolution takes place due to chemical oxidation of intermediate products by oxidizers—anode-dissolution products or solution components. The results of varying the chemical composition on surfaces depending on the treatment mode are presented.

DOI: 10.3103/S1068375507010012

1. INTRODUCTION

High-speed anode dissolution of high-temperature Ni–Cr-based alloys is widely used in technology used for the electrochemical dimensional processing (ECDP) of such alloys. Being multiphase materials, the specified alloys (containing nickel and chromium in addition to various amounts of alloying elements such as Al, Ti, W, Nb, Co, etc.) show a whole spectrum of properties during their dissolution via an anode at high current densities. Under certain conditions, the alloys typically experience so-called "abnormal" anode dissolution at which their ionization rate exceeds the Faraday rate while taking into account the stable degree of oxidation of the components passing into solution. Despite the fact that many features of the anode dissolution of these materials are well-known (see, for example, reviews [1–3]), small alterations in alloy composition can dramatically change, not only their physicomechanical, but their electrochemical properties as well.

In this paper, the electrochemical features of high speed anode dissolution of heat-resistant chrome–nickel alloys containing tungsten and rhenium are described. Investigation of these properties is not only of academic interest, but also is of importance for solving certain applied problems [3, 4]. In addition, features of the dissolution of the indicated materials provide an example of how a macroscopic inhomogeneity in the surface of an alloy affects its anode-dissolution rate for high current densities (see also [5]).

2. EXPERIMENTAL

We investigated the anode dissolution of two chrome–nickel alloys, whose composition is presented in Table 1. The composition and morphology of the alloys was determined both before and after processing by scanning electron microscopy (SEM) and by local *X*-ray spectral microanalysis using a TESCAN scanning electron microscope and the INCA Energy EDX

Table 1. Composition of investigated alloys (wt %)

Alloys	Ni	Cr	W	Re	Co	Ti	Al	C	Si	Electrochemical equivalent, g/(A h)
ZhS-6U	56.5 ± 0.8	9.1 ± 0.7	12.1 ± 2.0	–	9.5 ± 0.4	2.6 ± 0.5	5.5 ± 0.1	4.5 ± 0.6	–	0.79*/0.89
Alloy I	62.1 ± 0.1	4.8 ± 0.1	7.8 ± 0.5	5.6 ± 0.7	10.1 ± 0.4	–	5.0 ± 0.3	3.7 ± 0.2	0.9 ± 0.1	0.89*/0.95

* In the numerator—the results of calculation with the formation of Cr(VI), in the denominator—calculations with the formation of Cr(III).

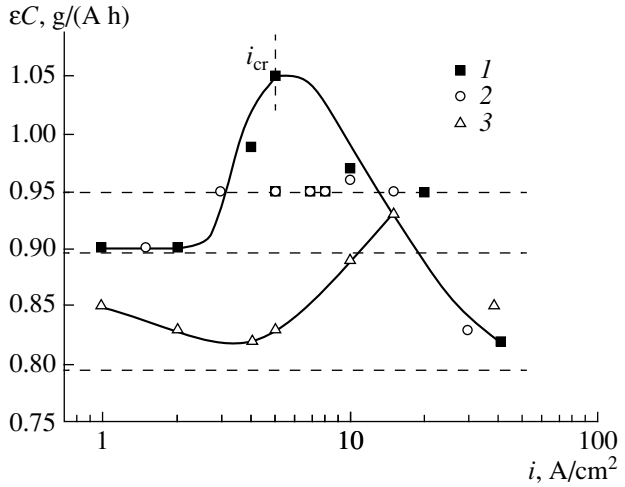

Fig. 1. Dependence of the specific dissolution rate of alloy I (*1*, *2*) and the ZhS-6U alloy (*3*) in 2 M NaCl at the RDE rotation velocities of: (*1*, *3*) 1260 and (*2*) 2500 rpm.

system for determining chemical composition. The method used for composition analysis consisted of measuring the local concentration of elements for an area of ~1–2 μm^2 at a depth to 2 μm. The analysis was carried out at three points on each sample. We calculated the average values for each series of measurements, these are listed in Table 1, together with their standard deviations.

On the basis of the obtained averages, we determined the electrochemical equivalent of an alloy from the following degrees of oxidation of components passing into the solution: Ni(II), Cr(VI), W(VI), Re(VI), Co(II), Ti(IV), and Al(III). In this case, we used the charge-summation method [1, p. 12], which is also reflected in Table 1. Because chromium can be dissolved as Cr(III) under the conditions used, we list values which were calculated using the chromium ionization of the lowest degree of oxidation (Cr(III)) in the same table.

High-speed anode dissolution of the ZhS-6U alloy was studied previously [6] as it applies to ECDP problems, while alloy I (containing rhenium) was investigated for the first time. Tungsten-containing high-temperature alloys were also investigated previously in [7–11].

For the high-speed anode dissolution of metals including high-temperature alloys, mutual influence of the processes of heat transfer and electrode kinetics [12] are the thermokinetic effects that play the major roles. To take them into account, it is necessary to analyze thermal effects, and in particular, to calculate the heat-transfer coefficients at the electrode–solution interface, which is possible when using a rotating disk electrode (RDE) [12]. For this reason, we used the RDE method in this study.

Samples from the indicated alloys ~3 mm in diameter were exposed to anode dissolution in 2 M NaCl using RDE rotation velocities varying from 250 to 2500 rpm and current densities from 0.1 to ~40 A/cm^2 in a cell with a volume of ~250 ml with separated anode and cathode spaces. The specific dissolution rate of an alloy (in g/(A h)) under galvanostatic conditions was determined for the total transmitted charge $Q = 0.023$ A h from the metal-weight loss. It varied for the preset Q from ~19 to ~23 mg. The measurements were carried out using current densities from 1 to ~40 A/cm^2.

The relationship between electrode-potential changes and time was measured by the procedure described in detail in [12] also under galvanostatic conditions using a saturated silver-chloride electrode as a reference. The polarization (galvanostatic) curves were plotted from these measurements in the current-density interval from 0.1 to 10 A/cm^2.

After processing at a preset level of transmitted charge (0.023 A h), we investigated the surface morphology using scanning electron microscopy and determined the chemical composition of the surface layer using EDX analysis.

Surface oxidation took place during anode dissolution, especially at high current densities. The oxide layers formed were inhomogeneous. Therefore, the measurements were performed separately for the "basic" (weakly oxidized) and "oxide" (strongly oxidized) phases. We measured the element content for the "basic" and "oxide" phases three times for each sample. From this data we then calculated the average concentration values of the elements in the surface layer after anode dissolution.

3. RESULTS AND DISCUSSION

3.1 Effects of Current Density, Alloy Composition, and Hydrodynamic Conditions on the Specific Dissolution Rate

According to the Faraday law, the dissolution rate for a given current density is determined from the following relation:

$$V = \frac{\varepsilon C i}{\rho}, \qquad (1)$$

where i is the current density, ρ is the metal density, C is the electrochemical equivalent of the alloy, and ε is the current efficiency. The quantity εC (measured experimentally), called the practical electrochemical equivalent (or specific dissolution rate), is, as a rule, a function of the current density ($\varepsilon C = f(i)$) and of other dissolution conditions (e.g., hydrodynamic conditions, solution composition, its pH, etc.). The experimental dependences obtained in this work for the solution under investigation (2 M NaCl) and a bulk temperature of electrolyte equal to 20°C are shown in Fig. 1.

Over a wide range of densities, the εC value is much higher for a rhenium-containing alloy; however, for $i >$ 15 A/cm^2, its values virtually coincide for both alloys (Fig. 1). The reasons for an essential distinction in the

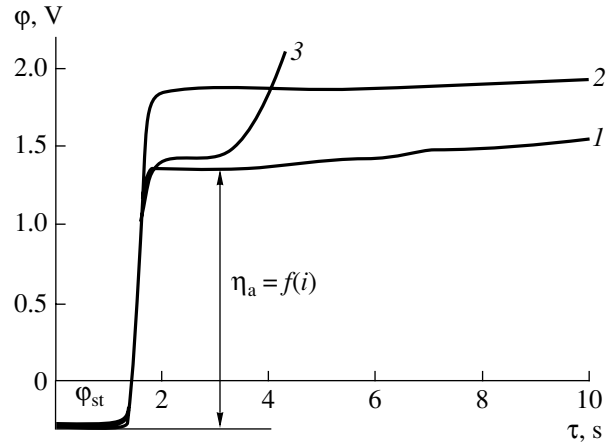

Fig. 2. Variation of the anode-dissolution potential of the alloy I for a current density of 5 A/cm^2 and RDE rotation velocities (*1*) 1940, (*2*) 1260, and (*3*) 250 rpm. φ_{st} is the stationary potential of the de-energized electrode.

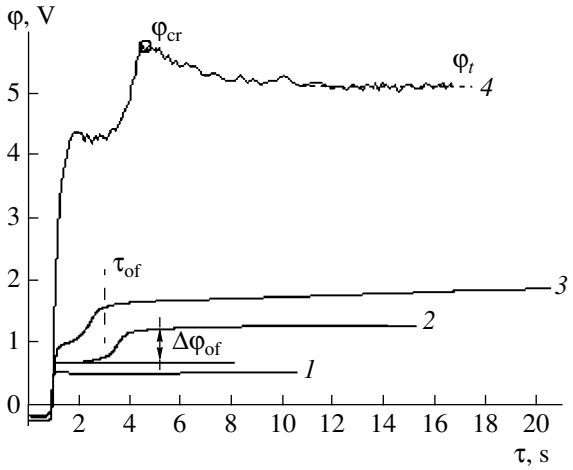

Fig. 3. Variation of the anode-dissolution potential of the ZhS-6U alloy at the current densities: (*1*) 0.3, (*2*) 0.7, (*3*) 3, and (*4*) 10 A/cm^2. The RDE rotation velocity is 1260 rpm.

specific dissolution rates for $i < 15$ A/cm^2 are considered below; however, on the basis of the results shown in Fig. 1, it can be concluded that if tungsten is partially replaced by rhenium in an alloy the alloy is then much better suited to anode processing over a wide current-density range.

For rhenium-containing alloys, the εC values were measured at different RDE rotation velocities. It can be seen that for relatively low current densities (1–2 A/cm^2) the εC values at different stirring rates (i), coincide, and (ii), are close to the values calculated on the assumption that nickel and cobalt are ionized in the form of bivalent ions, while chromium, tungsten, and rhenium are ionized to the highest degree of oxidation. For high current densities (to $i = i_{cr} \sim 5$ A/cm^2), the specific dissolution rate increased and, at relatively small RDE rotation velocities, it exceeded the calculated rate even under the assumption that chromium occurs as Cr(III). At higher rotation velocities, the rate coincided with that calculated under the assumption that nickel and cobalt are ionized as bivalent ions, and chromium—as Cr(III) (Fig. 1).

The peak value of εC was achieved for $i = i_{cr}$. In calculating i_{cr}, the following assumptions were made: (i) $i = i_{cr}$ is established because the surface concentration of dissolution products equals the saturation concentration on the basic component—nickel (and, possibly, simultaneously on both nickel and cobalt); (ii) the surface temperature exceeds the bulk temperature.

In calculating i_{cr} within the framework of these assumptions, we used the dependences of i_{ult} (the maximum anode current density at which the saturation concentration of iron and nickel dissolution products is achieved) on RDE rotation velocity obtained in [13] for iron and in [14] for nickel.

It was possible to assume that the value of i_{ult} for this chloride-ion concentration and stirring rate is the same for cobalt because in [13, 14], a dependence on the chloride-ion concentration was found rather than a dependence on the nature of the metal, and as well there was no dependence seen on the solution acidity.

The surface-temperature increment in comparison with the bulk situation was calculated from the equation in [12]:

$$\Delta T_s = \frac{i(\eta_a + \pi)}{\alpha}, \qquad (2)$$

where η_a is the overvoltage for the anode process, π is the Peltier coefficient, and α is the RDE heat-transfer coefficient. The value of α for the RDE with the rotation velocity used was taken from [12, p. 59] (α = 0.63 W/(cm^2 deg) at a rotation velocity of 1260 rpm). Then, taking the anode-overvoltage magnitude η_a (~2.1 V for $i = 5$ A/cm^2, see below) into account and accepting that $\eta_a \gg \pi$, we obtain $\Delta T \sim 17$°C. Under the assumption that the surface concentrations of the dissolution products of the basic components—nickel (and cobalt) achieve the saturation concentration, the value i_{ult} should be equal to 5 A/cm^2 at $n = 1260$ rpm, taking into account as well that the quantity i_{ult} from [13, 14] is equal to 3.5 A/cm^2 for 2 M NaCl at $n = 1000$ rpm and 20°C, and accepting that the relation between the growth of i_{ult} and temperature is ~ 1.5% per degree [12]. It is obvious that i_{cr} is the maximum current density of the anode dissolution of nickel (and, possibly, of both nickel and cobalt). It is exactly under these conditions that the peak value of εC, is achieved, which decreases with increasing stirring rate and current density.

3.2 Results of Polarization Measurements

In Figs. 2 and 3, we show the φ–τ curves for the tungsten- and rhenium-containing alloys (Fig. 2) at dif-

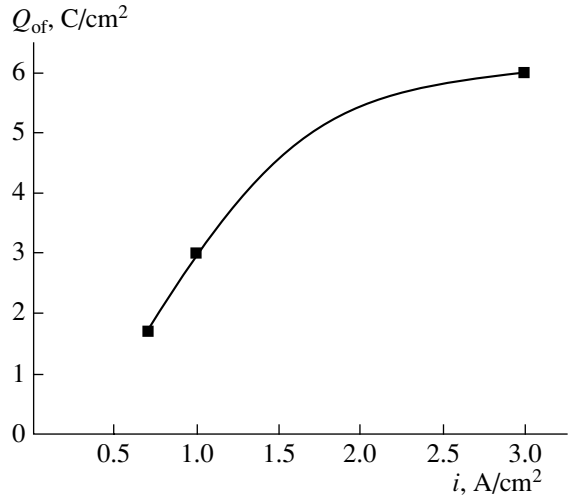

Fig. 4. Dependence of the charge density necessary for the formation of a surface oxide on the anode-dissolution current density for the ZhS-6U alloy at a rotation velocity of 1260 rpm.

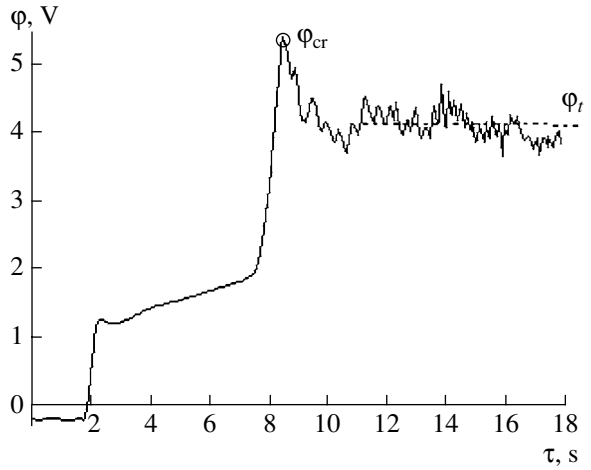

Fig. 5. Variation of the RDE anode-dissolution potential for alloy I at a current density of 5 A/cm^2 and a rotation velocity of 250 rpm.

ferent RDE rotation velocities and for the ZhS-6U alloy (Fig. 3) at the same rotation velocity (1260 rpm), but different current densities. The calculation from Eq. (2) showed that, if the magnitude ΔT_s is equal to ~9°C for curve *1* (Fig. 2), it is ~17°C for curve *2*, and $\Delta T_s = 30$°C for *3* (250 rpm) (the initial moment of processing before the potential-growth point in time). Thus, the potential for this current density is determined by both hydrodynamic conditions and the achievable surface temperature.

If the shape of the φ–τ curve of the dependences of a rhenium-containing alloy similar to those shown in Fig. 2 is conserved at high current densities for the ZhS-6U alloy, then such a shape of the dependence curve takes place only at relatively low densities (curve *1*, Fig. 3). For high current densities, a potential jump of $\Delta\varphi_{of}$ is observed. The value of the transmitted charge $Q = i\tau_{of}$ corresponding to this process, being a current-density function, increased with the current density, (Fig. 4). As is shown below, an additional voltage drop $\Delta\varphi_{of}$ was related, primarily, to surface oxidation. Taking into account the fact that the tungsten content inclined to passivation in neutral chloride solutions [1, 2] was much higher in the ZhS-6U alloy, oxide accumulation and, as a consequence, an additional voltage drop $\Delta\varphi_{of}$ upon dissolution of this alloy, occurs at much lower current densities. This agrees with the data presented above (see Fig. 1 from which it follows that, at $i \sim 1$–10 A/cm^2, εC is much higher than that for the rhenium-containing alloy and much less inclined to passivation than the tungsten alloy [1, 2]) and the results described below, thus indicating an elevated oxide concentration in the surface layer at low current densities for the ZhS-6U-alloy surfaces in comparison with alloy I. Upon reaching a certain relatively high potential φ_{cr} (Figs. 3 and 5), activation is observed (potential decrease over time) at high current densities along with simultaneous transition to an oscillatory mode.

Table 2. Critical temperature drops in the transition to the TKI and the oscillator dissolution process

Alloys	i, A/cm^2	Rotation velocity, rpm	ΔT_s^{cr}, °C	ΔT_s^t, °C
ZhS-6U	10	1200	79	68
Alloy I	5	250	83	65
	10	1260	–	68

As can be seen from the results of calculation presented in Table 2, the values ΔT_s^{cr} corresponding to φ_{cr} as well as the ΔT_s^t corresponding to φ_t calculated from Eq. (2) (see Figs. 2 and 3) are independent of both the alloy composition and the stirring rate. This means that φ_{cr} is actually the potential of the transition to thermokinetic instabilities (TKIs) (the "thermal explosion" potential; for more details, see [12, 15]), and φ_t is the transpassive-dissolution potential caused by the transition to the TKI (during the calculation of ΔT_s^{cr} and ΔT_s^t from Eq. (2), we used the quantity $\eta_a^{cr} = \varphi_{cr} - \varphi_{st}$ and $\eta_a' = \varphi_t - \varphi_{st}$, where φ_{st} is the stationary potential of a de-energized electrode (see Figs. 2, 3, and 5) as η_a). It is necessary to emphasize that during calculation we introduced a correction to an ohmic voltage drop between the capillary end and the electrode surface according to data published in [12, p. 54] taking the electrical conduction of the solution under investigation into account. The introduced correction was equal to ~1 V for i = 10 A/cm^2 and 0.5 V at i = 5 A/cm^2 (in

Figs. 2–6, the values of potentials are given without the correction of the ohmic component).

From the generalized polarization curves presented in Fig. 6, it can be seen that: (i) the dissolution potentials of both alloys virtually coincide in the region of low current densities when the accumulation of oxides in the surface layer and the corresponding voltage drop $\Delta\varphi_{of}$ for the alloy with a high tungsten content are negligible (see Fig. 2 curves *1* and *2*, Fig. 3 curve *1*, and Fig. 6 for $i = 0.1$ A/cm^2), and (ii) at higher current densities, the dissolution potentials of alloys with a higher tungsten content are higher owing to an additional voltage drop in the oxide film caused by the high content of tungsten inclined to the oxidation.

At current densities exceeding i_{cr}, the dissolution potentials of both alloys virtually coincide (in Fig. 6, the values of φ at $i = 10$ A/cm^2 are shown only for the ZhS-6U alloy, while they are not shown for the alloy I to avoid overloading the figure; however, both these values and potential-variation intervals are close).

The arrows in Fig. 6 show the conditions under which the potential growth in time (see, for example, curve *3* in Fig. 2) takes place. As can be seen, such a growth takes place upon achieving i_{cr}, which is related to the formation of a salt (oxide–salt) film passivating the alloy surface. It is obvious that, in this case, the dissolution occurs via a salt film.

The dashed lines in Fig. 6 show the Tafel curves for the dissolution of nickel and chromium in chloride solutions [1, 2, 9] upon which soluble products of ionization are formed (at current densities up to i_{ult} for nickel in the corresponding solution and for a preset stirring rate). The corresponding Tafel slopes are ~80 mV/order for nickel and 100 mV/order for chromium. It can be seen that the measured potentials prior to salt passivation are between these potentials (corrected for an additional voltage drop $\Delta\varphi_{of}$ for an alloy with a high tungsten content)

Thus, the dissolution of alloys can be carried out under conditions of active anode dissolution (or anode–anion activation [2]) with the formation of soluble products (in part or completely; to a great extent such a dissolution is characteristic of the alloy I for $i < i_{cr}$), but transpassive dissolution is possible, which is caused by the transition to TKI and occurs at $i > i_{cr}$. The value of i_{cr} depends on hydrodynamic conditions. For $i > i_{cr}$, we observed a decreasing dependence of the current efficiency εC on the current density (Fig. 1), the dissolution occurs via a passivating film, while change in the alloy-composition insignificantly affects the processing rate.

The transition from active (activited) to transpassive dissolution can be observed in time (Fig. 5). The characteristic times of transition processes and values of potentials are determined by the hydrodynamic conditions and surface temperature, which approaches the boiling temperature of the solution for $i > i_{cr}$.

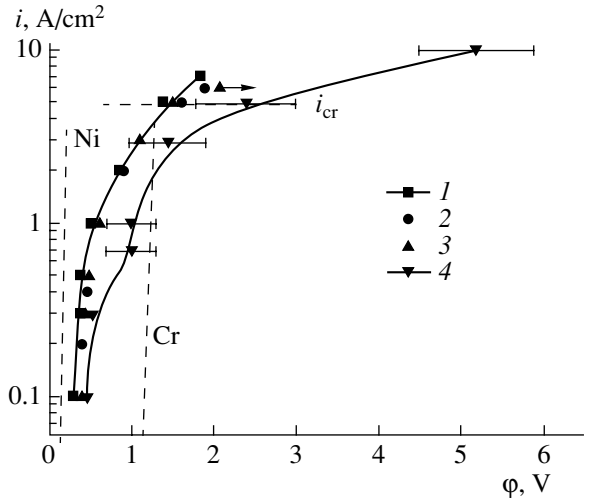

Fig. 6. Polarization curves for RDE anode dissolution in 2 M NaCl for (*1–3*) alloy I and (*4*) the ZhS-6U alloy at rotation velocities of (*1*) 1940, (*2*, *4*) 1260, and (*3*) 250 rpm.

3.3. Change in Composition of Surface Layers during Processing

In Fig. 7, we show SEM photomicrographies after the processing of the investigated alloys at fixed current densities (2, 5, 38, and 40 A/cm^2), $Q = 0.023$ A h, and the RDE rotation velocity of 1260 rpm. In Tables 3 and 4, we list the alloy-element content (wt %) after processing. As can be seen from the photomicrographies, the alloy surface after processing, as a rule, is nonuniform. This leads to the necessity of determining the chemical composition separately for the "basic" and "oxide" (i.e., enriched with oxygen) phases. In Tables 3 and 4, we list average values of these measurements at several points on the surface.

It can be seen that the surface layer of the alloys contains both oxygen and chlorine whose concentrations are dependent on a number of factors: (*a*) differs at varying areas of the surface (some areas are enriched with these components, and others do not contain these elements in the surface layer); (*b*) the content varies depending on the current density (Figs. 8 and 9); and (*c*) the content of these elements depends on the alloy composition (in particular, the alloy surface containing a high initial tungsten concentration is essentially more oxidized (Fig. 9b)).

In both alloys, there was virtually no chlorine in the surface layer after processing both at low and high current densities; however, chlorine was present in a significant amount after processing at $i \approx i_{cr}$. On the one hand, this proves that the peak surface concentration of chloride-containing dissolution products (nickel and cobalt) is achieved for $i \approx i_{cr}$, as was noted above, and on the other hand, it indicates that the oxide–salt surface film is transformed into an oxide film at high current densities ($i > i_{cr}$).

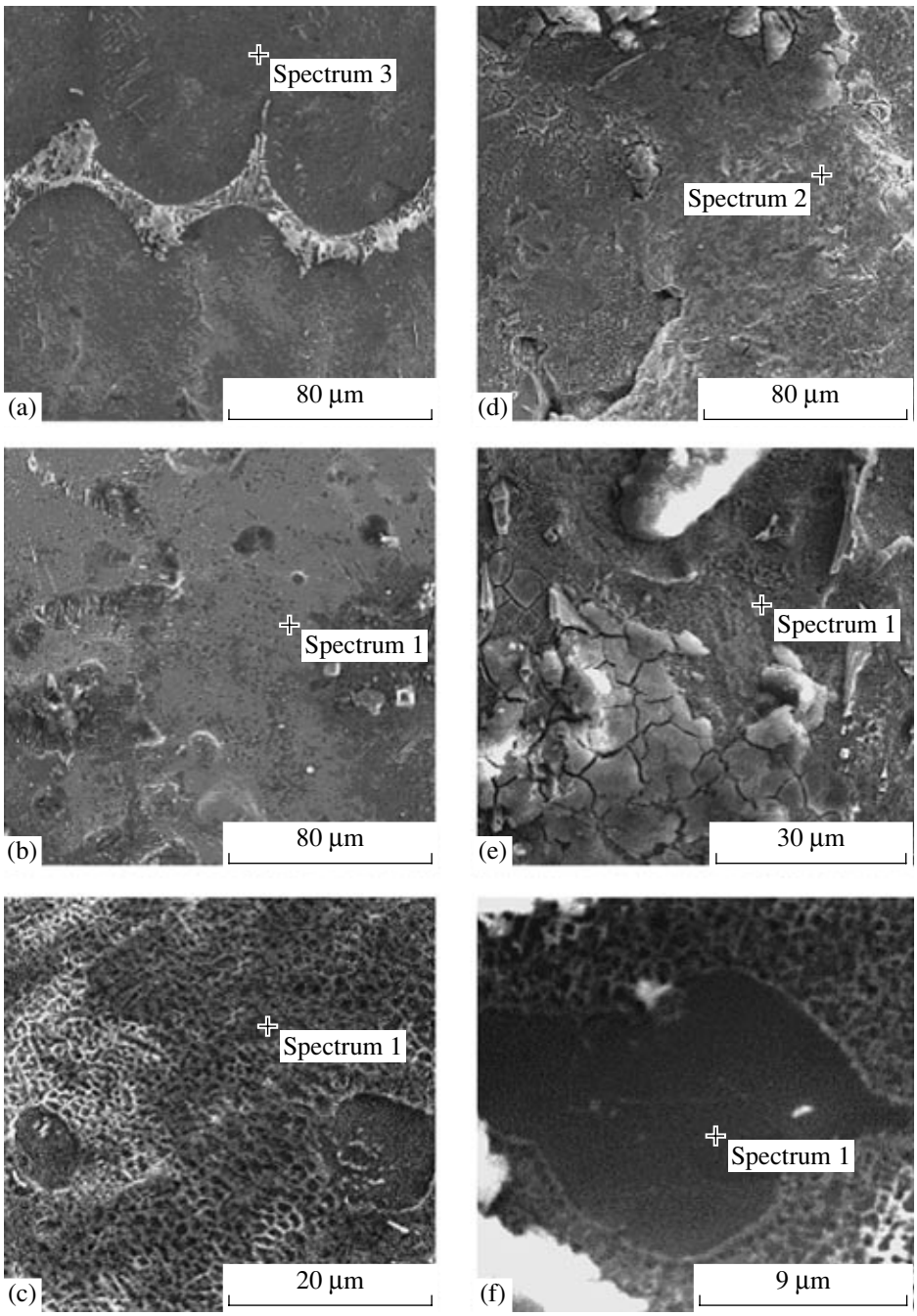

Fig. 7. Photomicrographies of surfaces for (a–c) alloy I and (d–f) the ZhS-6U alloy obtained after anode dissolution (0.023 A h) in 2 M NaCl for the RDE rotation velocity of 1260 rpm and the current densities: (a, d) 2, (b, e) 5, (f) 38, and (c) 40 A/cm^2.

The data in Fig. 8 confirm the assumption that there was an enrichment of the surface layer in tungsten (and in carbides, Tables 3 and 4) and a depletion of Ni, Cr, Co, Re, and Al—the alloy components, which form soluble products in the electrode reactions. Alteration of the surface-layer composition increased as current density increased (Fig. 8). (In Fig. 8, we show the values log$K$, where $K = \frac{C_s}{C_m}$, C_s is the average surface-layer concentration after processing, and C_m is the mean alloy concentration before processing.) In contrast to the results presented in Tables 3 and 4, the data shown in Figs. 8 and 9 show the component values averaged over the entire investigated surface. If only the basic phase was analyzed (without taking into account oxide surface formations discretely located on the dissolving surface), virtually no changes in the concentration of components in the surface layer were observed. For

Table 3. Content of components in a surface layer of alloy I after processing

		Concentration (wt %)								
		Ni	Cr	W	Re	Co	Al	C	O	Cl
Initial composition		62.1	4.8	7.8	5.6	10.1	5.0	3.7	–	–
2 A/cm^2	basic phase	56.1	4.4	8.7	6.8	9.4	6.3	4.5	1.6	0.8
	oxide phase	55.4	4.1	11.2	–	8.0	6.0	9.3	4.6	1.3
5 A/cm^2	basic phase	61.1	5.2	11.4	2.4	9.2	5.3	3.0	1.2	–
	oxide phase	36.8	2.5	6.2	–	6.7	2.5	8.0	20.1	15.9
40 A/cm^2	basic phase	50.3	3.6	10.9	1.9	8.0	5.2	13.0	6.7	–
	oxide phase	22.9	2.7	22.1	5.0	4.2	2.2	17.5	20.3	–

Table 4. The Content of components in a surface layer of the ZhS-6U alloy after processing

		Concentration (wt %)								
		Ni	Cr	W	Re	Co	Al	C	O	Cl
Initial composition		56.5	9.1	12.1	9.5	5.4	2.6	4.5	–	–
2 A/cm^2	basic phase	52.7	7.0	12.9	8.1	4.4	2.7	6.8	5.8	–
	oxide phase	33.5	4.4	26.5	5.5	1.6	3.6	9.3	15.6	–
5 A/cm^2	basic phase	53.4	9.4	14.0	10.0	6.4	2.7	–	3.6	11.4
	oxide phase	29.6	3.5	16.0	6.3	1.8	0.9	–	26.9	19.5
38 A/cm^2	basic phase	56.8	8.7	10.2	8.7	4.8	3.7	4.9	–	–
	oxide phase	5.2	2.9	39.2	–	–	9.2	16.7	26.5	0.7

example, the surface-layer concentration of nickel varies depending on the current density within a range of 53–57 wt % (with an average concentration of 56.5 wt % before processing), that of chromium—7.0–9.4 wt % (before processing 9.1 wt %), that of tungsten—10.2–14 wt % (before processing 12.1 wt %). A similar picture was observed for the component distribution after processing of the rhenium-containing alloy; however, it is noted in this case that the rhenium content decreased with increasing current density and was present in the oxide phase at high current densities.

3.4. Effect of Surface-Layer State on Dissolution Rate: "Abnormal" Dissolution and Its Mechanism

Due to their different electrochemical characteristics, the alloy components can: (*a*) be ionized in various degrees of oxidation; (*b*) give different soluble and insoluble products in cationic (Ni^{+2}, Co^{+2}, and their hydrochloride complexes) and anionic forms ($Cr_2O_7^{2-}$; ReO_4^-) under particular conditions (i.e., the current density and its corresponding potential, or the composition of the near-electrode medium specified by the temperature and stirring rate); (*c*) be oxidized with the formation of oxidant and passivated insoluble products (e.g., tungsten oxides). The achievable dissolution rate depends on both the oxidation rate of surface layers and their ionization with transition in the solution as soluble products.

From our results, it follows that one of the basic reactions is the surface oxidation with the formation of insoluble oxides:

$$Me + nH_2O \longrightarrow MeO_n + 2nH^+ + 2n\bar{e}. \qquad (3)$$

In general, reaction (3) corresponds to the ionization of tungsten, which is accumulated on the surface as an oxide. The ionization according to Eq. (3) decreases the dissolution rate, which indicates a decrease in εC with increasing current density (Fig. 1) and the accumulation of oxides in the surface layer with increasing current density (Tables 3 and 4, Fig. 9b).

However, despite the obvious fractional ionization of alloy components according to Eq. (3) leading to an increase in alloy weight rather than its dissolution with accompanying weight loss; as a whole, the dissolution rate can exceed the Faraday rate calculated on the assumption of the ionization of components in the degrees of oxidation stable for this solution.

The possible reasons for the abnormal dissolution of chrome–nickel alloys in chloride solutions were noted previously in [7, 16].

If one accepts the stage mechanism of dissolution of the basic nickel-alloy (and also cobalt-alloy) compo-

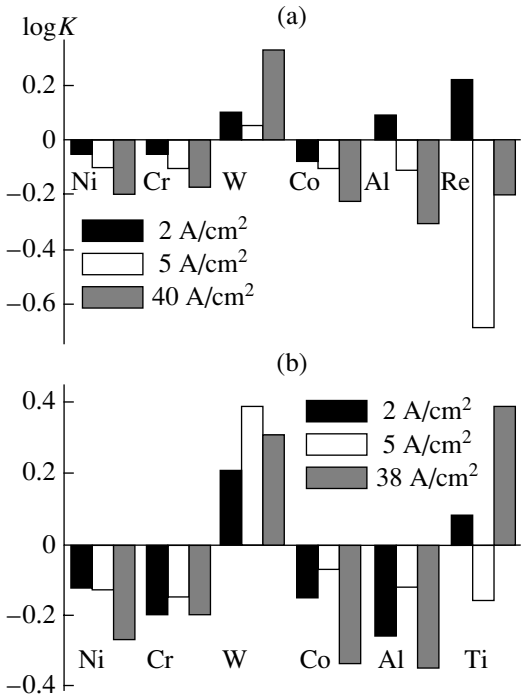

Fig. 8. Diagram of the variation of the component concentration for (a) alloy I and (b) the ZhS-6U alloy in the surface layer after anode dissolution with different current densities.

nent with a slow second oxidation stage of the intermediate low-valence particle (ILVP):

$$Ni + OH^- \rightleftharpoons (NiOH)_{ads} + \bar{e}; \quad (4)$$

$$(NiOH)_{ads} \longrightarrow NiOH^+ + \bar{e}; \quad (5)$$

$$NiOH^+ \rightleftharpoons Ni^{+2} + OH^-, \quad (6)$$

then, owing to the slowness of reaction (5), an intermediate product (ILVP) accumulates, and the possibility of the chemical oxidation of the ILVP by an oxidant (for example, a bichromate ion) appears:

$$6(NiOH)_{ads} + Cr_2O_2^{2-} + 20H^+ \rightleftharpoons 6Ni^{2+} + 2Cr^{3+} + 13H_2O. \quad (7)$$

The consequence of reaction (7) is the transfer of nickel (and also cobalt, i.e., the alloy components which amount to ~70% of the alloy mass) in the solution by nonelectrochemical means, without energy loss from the current source.

A high degree of filling of the surface with an intermediate product is necessary for continuing the reaction according to the above mechanism, which should be the consequence of both the slowness of second-stage dissolution (5) and the greatest possible filling of all of the dissolution surface by the final product—nickel (and cobalt) hydrochloride complex:

$$Ni^{2+} + xH_2O + yCl^- \rightleftharpoons [Ni(OH)_xCl_y]^{2-x-y} + H^+. \quad (8)$$

The last condition is fulfilled after achieving the final current, that is, when a salt film of a particular thickness forms on the dissolution surface according to reactions (4)–(6) and (8) and is dissolved. However, owing to ILVP accumulation, chemical oxidation according to reaction (7) takes place exactly under these conditions, as well as abnormal anode dissolution (the role of the oxidant can be played not only bichromate ions, but also by other ions, for example, perrhenate ions, as well as the solution components).

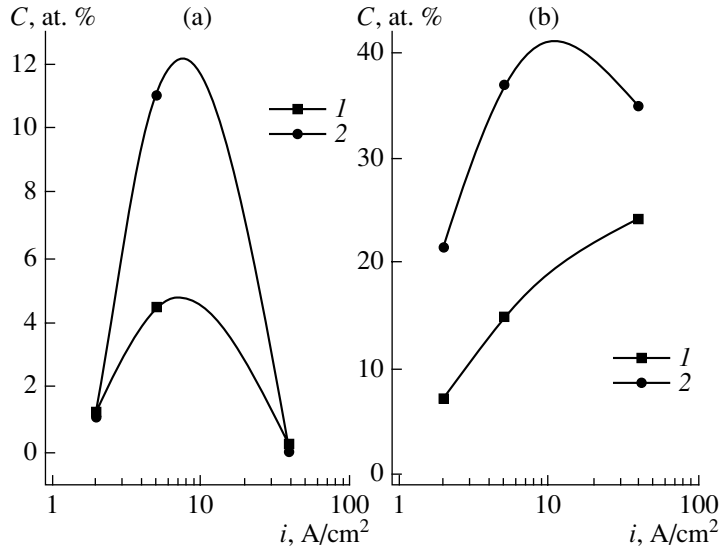

Fig. 9. Effect of the current density on the surface-layer concentration for (a) chlorine and (b) oxygen after anode dissolution of (*1*) alloy I and (*2*) the ZhS-6U alloy.

It is obvious that a similar mechanism cannot occur in the region of low current densities or by increasing the stirring rate (Fig. 7) because the ILVP surface concentration is insufficient for the reaction (7) (or a similar one).

It is also clear that, owing precisely to reactions occurring according to the above mechanism, the peak dissolution rate is achieved for $i \approx i_{cr}$. For current densities where $i > i_{cr}$, the current efficiency εC decreases with the current density, which is a consequence of dissolution according to the "transpassive" mechanism along with an increase in the fraction of energy loss in reaction (3) leading to passivation instead of dissolution.

4. CONCLUSION

The results of these investigations demonstrate the important role that the presence of tungsten plays for heat-resistant chrome–nickel alloys during their electrochemical dimensional processing in chloride solutions. Its presence in an alloy at a concentration of ~12 wt % leads to passivation of the surface and a decrease in the dissolution rate in comparison with a material containing a smaller amount of tungsten. A partial substitution of tungsten by rhenium in an alloy results in depassivation, an increase in the dissolution rate, and a decrease in the dissolution potential for a preset current density.

High-speed dissolution of the investigated alloys can be carried out according to various mechanisms. When dissolving in an active (anode-activated) potential range (at current densities lower than the maximum current density i_{ult} of the salt passivation because the dissolution-product concentration of the basic component (nickel) achieves the saturation concentration, and a salt film is formed), we observed: (*a*) a distinction in dissolution rates for alloys with different tungsten contents; (*b*) an increasing dependence of the current efficiency on the current density.

Dissolution in the transpassive region occurs at a surface temperature which exceeds the bulk temperature, and under a condition of thermokinetic instability resulting in periodic failure and the formation of surface coating layers (preferentially oxide layers). During dissolution under these conditions, a decreasing dependence of the current efficiency on the current density occurs; this dependence is caused predominantly by the preferential accumulation of insoluble oxides on the surface, while the dissolution rate is virtually independent of the alloy composition and hydrodynamic conditions.

The transition from activated to transpassive dissolution is determined by the hydrodynamic conditions and by achieving the final anode current for the basic component. The kinetics of the formation and dissolution of the salt film coating the electrode surface under these conditions is such that the chemical oxidation of intermediate products of nickel (and cobalt) by oxidants (both products of anode dissolution and solution components) is possible, which results in an anomalously high rate of anode dissolution.

ACKNOWLEDGMENTS

The authors thank E. Momaiko (at the Center of Investigations and Testing of Materials, Technical University of Moldova) for performing the surface analysis.

REFERENCES

1. Dikusar, A.I., Engel'gardt, G.R., Petrenko, V.I., and Petrov Yu., *Elektrodnye protsessy i protsessy perenosa pri elektrokhimicheskoi obrabotke metallov* (Electrode Processes and Transport Processes during Electrochemical Dimensional Processing of Metals), Chisinau: Stiinta, 1983.
2. Davydov, A.D. and Kozak, E., *Vysokoskorostnoe elektrokhimicheskoe formoobrazovanie* (High-Speed Electrochemical Formation), Moscow: Nauka, 1990.
3. Eliseev, Yu.S., Krymov, V.V., Mitrofanov, A.A., Saushkin, B.P., Sychkov, G.A., and Troshin, A.N., *Fizikokhimicheskie metody obrabotki v proizvodstve gazoturbinnykh dvigatelei (Physicochemical Methods of Processing in Manufacture of Gas–Turbine Engines)*, Saushkin, B.P., Ed., Moscow: Drofa, 2002.
4. Altynbaev, A.K., Ivanenkov, I.A., and Saushkin, B.P., Surface-Layer Improvement when Machining Small-Diameter Holes in Details from High-Temperature Alloys, *Uprochn. Tekhnol. Pokr.*, 2006, no. 8, pp. 38–42.
5. Dikusar, A.I., Redkozubova, O.O., Yuschenko, S.P., and Yakhova, E.A., Anodic Dissolution of Armco Iron in a Mixed Kinetics Mode: Effect of Macroscopic Heterogenity, *Russ. J. Electrochem.*, 2002, vol. 38, no. 6, pp. 632–637.
6. Atanasyants, A.G., Kuznetsova, T.M., Kornienko, V.A., and Kuzin, V.I., A Study of the Anodic Dissolution of Type ZhS-6U and Ah S-26 Alloys with Respect to Electrochemical Machining to Size, *Soviet Surface Eng. Appl. Electrochem.*, 1985, no. 3, pp. 1–5.
7. Dikusar, A.I. and Arzhintar', O.A., Anomalies during a High-Speed Anode Dissolution of Chrome–Nickel Alloys, *Teoriya i praktika elektrokhimicheskoi obrabotki v rastvorakh nitratov i khloratov*, Chisinau: Stiinta, 1976, pp. 3–19.
8. Petrenko, V.I., Dikusar, A.I., and Arzhintar', O.A., Effect of Concentration of Strengthening γ-Phase in Heat-Resistant Chrome–Nickel Alloys on Rate of their Electrochemical Processing in Solutions of Nitrates and Chlorates, *Elektron. Obrab. Mater.*, 1976, no. 4, pp. 14–19.
9. Petrenko, V.I., Investigation of Electrode-Process Effect on Technological Characteristics of Electrochemical Processing of Nickel, Chromium, and High-Temperature Alloys Based on them, *Cand. Sci. (Techn.) Dissertation Theses*, Novocherkassk, 1979.
10. Nevskii, O.A., Zhokhova, O.K., Dikusar, A.I., and Rumyantsev, M., Anode Dissolution of High-Temperature ZhS-6U Alloy in Water and Water–Organic Electro-

lytes, *Izv. Vyssh. Uchebn. Zaved. Khim. Khim. Tekhnol.*, 1990, vol. 33, no. 6, pp. 74–81.

11. Amirkhanova, N.A., Balmasov, A.V., Lilin, S.A., Pimenova, N.I., and Saypova, V.V., Comparative Characteristics of High-Speed Anodic Dissolution of Prospective Heat-Resistant Nickel-Based Alloys, *Surface Eng. Appl. Electrochem.*, 1997, no. 5, pp. 23–27.
12. Dikusar, A.I., Engel'gardt, G.R., and Molin, A., *Termokineticheskie yavleniya pri vysokoskorostnykh elektrodnykh protsessakh* (Thermokinetic Phenomena in High-Speed Electrode Processes), Chisinau, 1989.
13. Kio, N.S. and Landolt, D., Rotating Disk Electrode Study of Anodic Dissolution of Iron in Concentrated Chloride Media, *Electrochim. Acta*, 1975, vol. 20, no. 5, pp. 393–399.
14. Davydov, A.D., Kabanov, B., Kashcheev, V.D., Mirzoev, R.A., and Nenashev, V.A., Anode Dissolution of Nickel in Intermixed Solutions of Chlorides as Applied to the Dimensional Electrochemical Processing, *Fiz. Khim. Obrab. Mater.*, 1972, no. 4, pp. 139–142.
15. Engelgardt, G.R. and Dikusar, A.I., Thermokinetic Instability of Electrode Processes. I Theoretical Analysis, *J. Electroanal. Chem.*, 1986, vol. 207, no 1, pp. 1–11.
16. Arzhintar', O.A., Dikusar, A.I., and Petrov Yu.N., Oxidation of Intermediate Low-Valence Particles at High-Speed Anode Dissolution of Chrome–Nickel Alloys in Solutions of Chlorides, *Dokl. Akad. Nauk SSSR*, 1975, vol. 225, no. 5, pp. 1088–1092.

ISSN 1068-3755, Surface Engineering and Applied Electrochemistry, 2007, Vol. 43, No. 1, pp. 11–17. © Allerton Press, Inc., 2007.
Original Russian Text © D.Z. Grabco, I.A. Dikusar, V.I. Petrenko, E.E. Harea, O.A. Shikimaka, 2007, published in Elektronnaya Obrabotka Materialov, 2007, Vol. 43, No. 1, pp. 16–23.

ELECTRICAL SURFACE TREATMENT METHODS

Micromechanical Properties of Co–W Alloys Electrodeposited under Pulse Conditions

D. Z. Grabco, I. A. Dikusar, V. I. Petrenko, E. E. Harea, and O. A. Shikimaka

Institute of Applied Physics, Academy of Sciences of Moldova, ul. Academiei 5, Chisinau, MD-2028, Republic of Moldova

Received February 27, 2006

Abstract—Results of the investigation of pulse current frequency influence (rectangular unipolar pulses, i_m = 3 A/dm^2, relative pulse duration 3, frequency 0.67–333 Hz, Q = 3600 C/dm^2) on the properties of Co–W alloys at electrochemical deposition—deposition rate, current efficiency, structure of obtained coatings, and their microhardness (microindentation and sclerometric ones)—are presented. The correlation between the microhardness determined by quasi-static indentation and the "organic" phase content in the alloy is shown (the microhardness decreases as the total content of carbon and oxygen in the deposited layer increases). Sclerometric tests have shown that microhardness increases with an increasing tungsten concentration in the deposited layer.

DOI: 10.3103/S1068375507010024

INTRODUCTION

In recent years, an intensive search for new environmentally safe functional and decorative coatings with a view to substitute chromium ones, widely applied in industry at present, has been carried out. This problem is caused by the necessity to eliminate environmentally harmful production applied to obtaining chromium coatings, despite the fact they satisfy many performance requirements [1–3].

Possible variants for this substitution are the coatings of cobalt–tungsten alloys. These alloys may potentially have high hardness, excellent wear resistance, and a low friction coefficient [1–4]. In a number of studies [3–10], it was noted that electrodeposition yields amorphous and nanocrystal coatings of Co–W alloys, both pure and containing impurities of boron and iron on soft steel. Subsequent annealing makes it possible to significantly increase the coating hardness due to recrystallization processes proceeding thereat.

It is shown in [1] that one of the methods for the improvement of mechanical and performance properties of coatings may be the application of electrolysis pulse conditions. It is known that the application of pulse conditions of electrodeposition allows for the control of the composition and structure of alloys [12]. The present work is dedicated to finding the relationship between the conditions of pulse electrochemical deposition of Co–W alloys, the composition and structure of the obtained layers, and the micromechanical properties of the obtained coatings.

EXPERIMENT METHODS

Electrodeposition Conditions

Electrolytic coatings were deposited from a citrate electrolyte (used, in particular, in [9, 10]) of the following composition, mol/l: Na_2WO_4, 0.05; $CoSO_4$, 0.2; $C_6H_8O_7$ (citric acid), 0.04; $Na_3C_6H_5O_7$ (sodium citrate), 0.25. It was shown that T = 25°C and the current density of 3 A/dm^2 are optimal conditions for obtaining from this electrolyte of amorphous coatings with high tungsten content in the alloy (this is, as a rule, the purpose of obtaining these layers, since increasing tungsten content improves its performance properties, particularly, its microhardness [9]). In the Co–W electrodeposition process, the near-electrode layer buffering is important; for this purpose, boric acid with a concentration of 0.65 mol/l, was introduced into the electrolyte [13]. In the present work, an electrolyte of the above-mentioned composition with the addition of boric acid was used. The electrolyte was prepared by dissolution of cobalt sulfate ($CoSO_4 \cdot 7H_2O$), sodium tungstate ($Na_2WO_4 \cdot 2H_2O$), citric acid, and sodium citrate in distilled water with subsequent addition into the solution of boric acid up to its total concentration of 40 g/l.

Deposition was carried out on glass-textolite disks covered with copper foil of thickness 105 μm, which were placed in a special holder and fixed with a clamping screw. Samples of two variants were used: in a "macrovariant," with a total surface of the free circular section of the sample of 0.785 cm^2 (diameter ~10 mm), and in a "microvariant," with an active section on the disk surface with an area of 0.031 cm^2. In the latter case, the whole surface, with the exception of a hole ~2 mm diameter, was isolated by pressure-sensitive polyvinyl chloride film of thickness ~95 μm. The use of microsamples in the present study was caused by the

Table 1. Electrodeposition conditions, composition and micromechanical properties of the studied samples

No.	f, Hz	C_{W+Co}, mass %	C_W, mass %	H_v, kgf/mm^2	H_s, kgf/mm^2
1	0.67	93.6 ± 0.5	18.5 ± 0.9	590/526	–/105
2	0.67*	–	–	622/–	–/–
3	3.33	95.4 ± 1.2	21.3 ± 2.1	–/404	–/194
4	3.33*	92.4 ± 0.5	19.0 ± 0.2	685/–	–/–
5	6.7	93.5 ± 1.7	20.8 ± 1.5	–/325	–/–
6	33.3	91.6 ± 2.7	15.3 ± 0.4	–/464	–/132
7	66.7	91.6 ± 0.8	23.2	–/536	–/203
8	333	92.8 ± 0.7	22.4 ± 1.5	–/401	–/203
9	333*	90.0 ± 1.0	13.0 ± 0.4	–/511	–/–

* Data for microsamples are given. In the numerator and denominator of the fraction, the sample microhardness values before and after polishing, respectively, are given.

necessity to obtain miniature parts used in microelectronics. Samples were fixed in a special holder which was placed in an electrochemical cell. The deposition methods were analogous to those described in [10, 13]. The deposition was carried out under stationary conditions (in a vessel with an immovable electrolyte) at room temperature (~25°C). The electrolyte of total volume 250 ml was weakly mixed by a magnetic mixer. Graphite pivots were used as an anode. The anodic and cathodic spaces were not separated. Preparation of the samples before deposition of Co–W alloys was carried out by generally adopted methods [14].

As mentioned above, an optimal value of the current density for deposition from the mentioned electrolyte without the addition of boric acid is equal to 3 A/dm^2. In the present study, the deposition was carried out at a rectangular unipolar pulse current with the same current density of 3 A/dm^2. The pulse current parameters were set by virtue of potentiate PI-50-1. The relative pulse duration (ratio of the total period of pulse τ_i and pause τ_p to pulse duration) in all cases was equal to 3, and the frequency varied in the range of about three orders of magnitude, from 0.67 to 333 Hz. The total time of deposition in all cases was 20 min. The deposition conditions and the sample characteristics are given in Table 1.

At deposition under the macrovariant conditions, the metal yield on the current was determined by the weight method, taking into account the total increase of the sample mass while passing Q = 3600 C/dm^2 (no correction was made for the deposit mass increase due to introduction of an "organic" phase co-deposited with the alloy, which has not influenced the principal conclusions due to the small value of atomic weights of light elements constituting the specified phase). The calculation was carried out proceeding from a chemical equivalent of the alloy 0.311 mg/C, being average for all possible compositions. The probable error here does not exceed 1%. In the case of deposition in the microvariant (at the same electric charge), the average thickness of the coating was determined by a metallographic microscope, because at small dimensions of the sample, the error at weighing appears to be too great.

Analysis of Composition and Study of the Coating Morphology

The chemical composition of the obtained samples was studied by the method of energy-dispersive x-ray spectroscopy (EDX-spectroscopy) with an INCA Energy analyzer.

Identification of the surface microstructure and morphology was performed by virtue of the scanning electron microscope Vega Tescan, the optical microscopes Amplival, Neophot, and the interferometer MII-4.

Micromechanical parameters (indentation microhardness H_V and sclerometric microhardness H_s) were determined by the microhardness tester PMT-3. Loads P, applied to a Vickers diamond indentor, were varied within the range of 0.1–0.5 N. Tests were performed at room temperature. The microhardness values were determined using known formulae [15]. For a quasi-static indentation, $H_V = 1854\ P/d^2$; for sclerometric tests (scratching method), $H_s = 1000\ P/a^2$, where d is the indentation diagonal and μm; and a is the scratch width, μm. Final values of microhardness for each load were estimated as an average measurement for 10–15 indentations (depending on the spread in data) or of 5 scratches.

In some cases, in order to obtain sharp, well-defined indentations, before microhardness measurement, the sample surface was polished with chromium oxide (powder of Cr_2O_3 with the grain dimension <2 μm) to eliminate roughness and obtain a smooth, flat surface. For comparison, in some samples, the initial surface microhardness was preliminarily measured directly after Co–W coating deposition and after polishing.

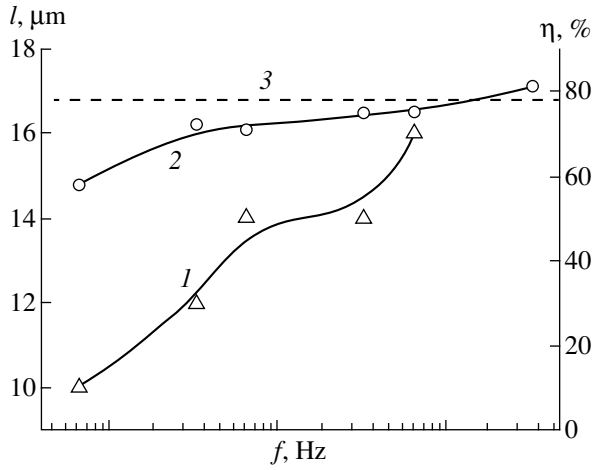

Fig. 1. Variation of the coating average thickness (*1*) and the metal yield-on-current (*2*) in dependence on pulse current frequency. Horizontal line (*3*) shows the value of the yield-on-current at deposition at a constant current density of 3 A/dm^2.

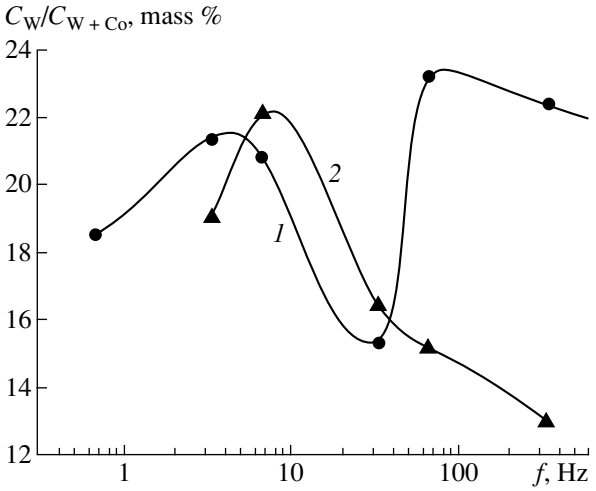

Fig. 2. Dependence of relative tungsten concentration in the coating on pulse current frequency in macro- (*1*) and microsamples (*2*).

RESULTS AND DISCUSSION

Influence of the Pulse Current Parameters on Deposition Rate, Composition, and Morphology of the Coating

As shown in Fig. 1, the average thickness of the coating at Q_{cp} = const increases with an increasing pulse current frequency. This is explained by an increase of the metal yield on the current. However, the highest value of the yield-on-current (YC) determined at the maximal frequency (with the pulse duration τ_i = 1 ms) did not practically exceed the average value (~78%) obtained by deposition in the same electrolyte at a constant current [13]. It is obvious that the deposition rate and YC at deposition on micro- and macrosamples do not qualitatively differ, but they increase with the pulse current frequency. The coating thickness varied across the sample surface: the greatest thickness was at a distance from the center; and on the edge, it decreased again due to the current distribution across the sample surface and due to edge effects near the holder body.

However, the tungsten content in the coatings obtained by different variants differ considerably at the frequencies above 30 Hz (Fig. 2). At a higher frequency, the tungsten content in microsamples is significantly less. It should be noted that Fig. 2 shows the average values, but the spread in particular values may achieve 10% with respect to root–mean–square deviation (Table 1).

At treatment with a frequency of less than 30 Hz, the average values of tungsten content in the samples obtained by the two methods were close (Fig. 2). However, deviations observed at high frequencies show that the electrochemical method to obtain alloys of the given composition is sensitive to fine variations in the process parameters. Small variations in the conditions result in significant changes in the composition and the properties of the coatings of these alloys.

The sample surface morphology is characterized by both common and distinctive characteristics. A common characteristic of all samples was the appearance of a mosaic picture on the film surface resembling the grain structure of polycrystalline materials (Fig. 3).

Dimensions of the mosaic cells varied in different samples from 5–10 to 50–100 μm. An analogous picture is observed at investigation by virtue of an optical microscope. It is obvious that the boundaries between the cells are breaks in the deposited layers, which testify to the high cracking of the obtained coatings.

The surface inside the cells has various structures. In some cases, it was smooth with no roughness (Fig. 3b), and in other cases, globules (hemispheres) of different a dimension and density were observed (Figs. 3a and 3c). The globule diameter varied in the range of 1–25 μm, and their height was about 1–6 μm.* Formations of the semicylindrical form of an arbitrary orientation shown as an oriented accumulation of hemispheres were also observed (Fig. 3c). Formation of such a microstructure is apparently determined to a certain degree by the relief of the copper foil surface, whereupon the film was deposited, because a similar picture is observed on the initial sample surface. Nonisotopy, disorientation of the substrate crystallites, leads to local accumulations of defects and preferential growth of deposit on these sections.

After insignificant removal of the coating surface layer, its surface changed form. The mosaic boundaries still existed, while the inner surface suffered a modifi-

* This is probably the reason for overstating the deposit thickness at measurements using a metallographic microscope.

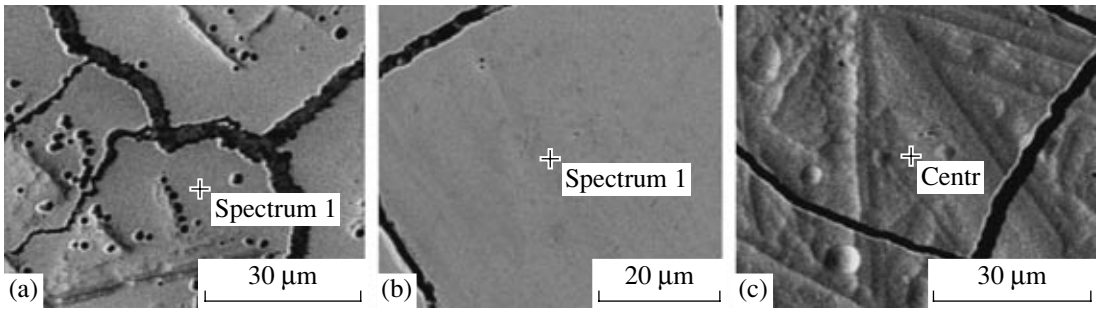

Fig. 3. Morphology of the surface observed in the scanning electron microscope after deposition at frequency 0.67 Hz (a, b) and 333 Hz (c) in macro- (a, c) and microsamples (b).

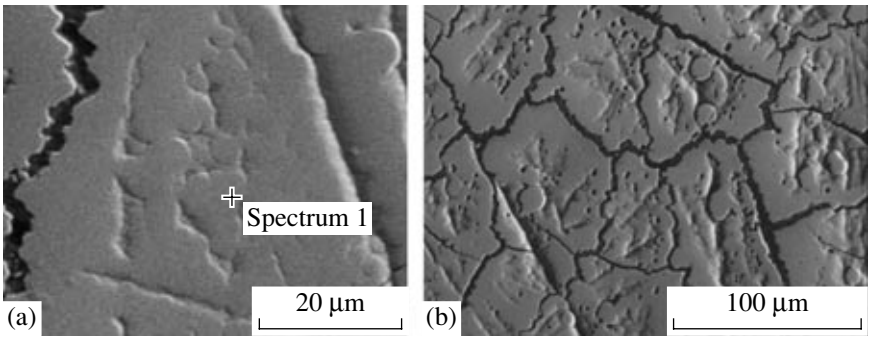

Fig. 4. Structure shown in the scanning electron microscope after partial polishing of surfaces of the samples deposited at frequency 33 Hz (a) and 333 Hz (b) (macrosample).

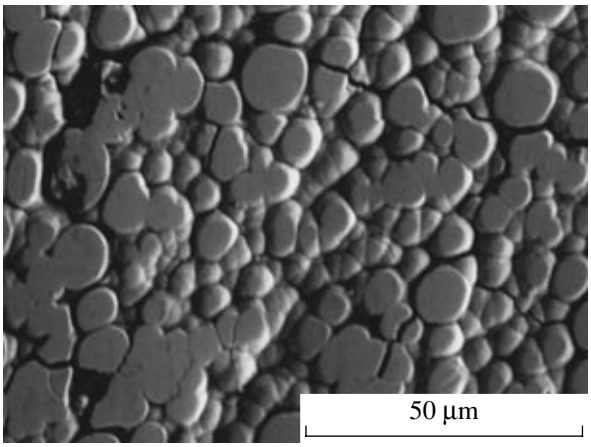

Fig. 5. Picture of the surface after partial polishing of the sample with high-density globules obtained by deposition with the pulse current frequency 6.7 Hz.

cation (Figs. 4 and 5). The tops of the formations of the semicylindrical form and globules have been polished-off, and on the surface, extensive (Fig. 4) or circular (Figs. 4b and 5) areas, instead of the globules, remain. These microphotographs of the surface obtained after mechanical polishing show that the formed globules are not hollow formations (Fig. 5).

The data in Table 1 show that the composition of the obtained deposits contains 90–95% cobalt and tungsten, and the rest is an "organic" phase. The dependence of the total concentration of carbon and oxygen in the obtained layers on the treatment conditions is shown in Fig. 6. It is seen that the total concentration of carbon and oxygen may achieve 36 at. %. Furthermore, it is changed by the frequency, i.e., by the pulse treatment conditions.

On the Correlation of Composition, Structure of the Obtained Layers, and Their Micromechanical Properties

Figure 7 shows the dependences of the average values of microhardness (indentation one) on pulse current parameters for two deposition conditions: by micro- and macrovariants. It is seen that, in all cases, H_V values for the microsample are significantly higher. That is, there is no direct dependence of the microhardness value on the tungsten content in the alloy. At the same time, an obviously pronounced correlation between the concentration of "impurity" (C=O) and microhardness is observed. As follows from the comparison of data for the microsample shown in Figs. 6 and 7, when the concentration of carbon and oxygen in the deposit increases, the microhardness decreases, and vice versa—it increases with a decreasing concentration decreasing. However, for the lowest H_V values (e.g., registered at f = 6.7 Hz), it is significantly higher than the

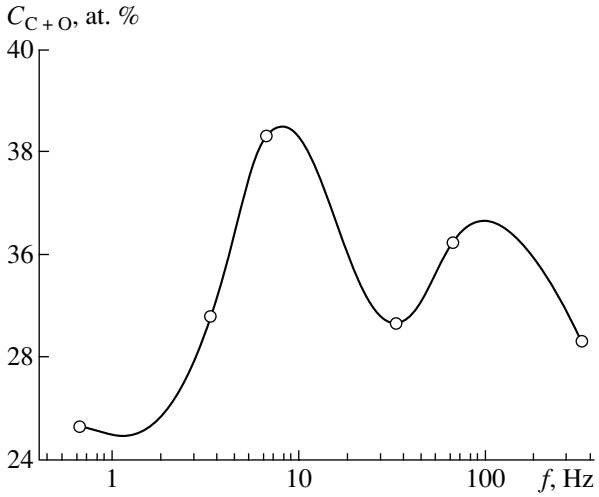

Fig. 6. Dependence of the total concentration of carbon and oxygen ("organic" phase) in the coating on the pulse current frequency.

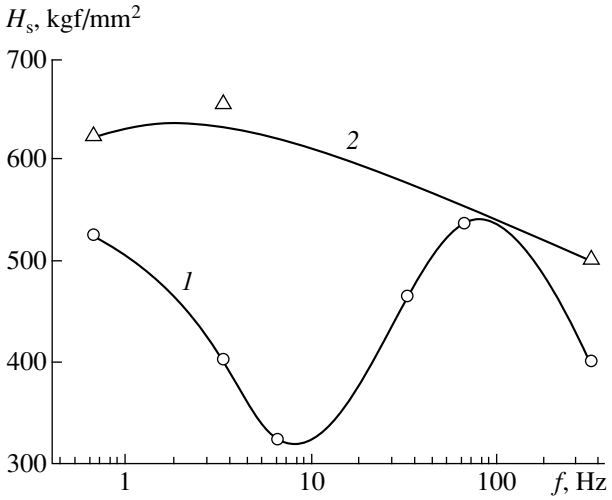

Fig. 7. Influence of the pulse current frequency on microhardness of cobalt–tungsten coating in macro- (*1*) and microsamples (*2*).

microhardness of the substrate ($H_V^{Cu} = 110$ kgf/mm^2) and cobalt, and, in the majority of cases, it is higher than the microhardness of tungsten and cobalt oxide, being inferior only to the values of microhardness of tungsten carbides (Table 2). It should be noted that, here, we consider the values of the microhardness of coatings after electrodeposition without heat treatment.

It is also obvious that the value H_V is influenced by the electrodeposited layer structure. The lowest microhardness is achieved when a globular structure is formed (Figs. 5 and 7), but these are the conditions for observation of a maximal concentration of "organic" phase in the coating.

A comparison of H_V values determined in one sample under different conditions of the surface preparation before measurements (Table 1, Fig. 7) shows that microhardness varies insignificantly (by ~11% for the deposits obtained at current frequency 0.67 Hz), which is considerably less than the differences resulting from a variation in the conditions for obtaining coating.

The data given in Table 1 and in Figs. 2 and 6 correspond to the composition determined directly after electrodeposition of films before polishing. Determination of the surface layer composition after polishing may give other values of concentrations of the components, which in turn influences the obtained values of microhardness. This is an extra confirmation of a known statement that in the case of amorphous electrodeposited films, the films under study belonging to them [9, 10], composition and mechanical properties may differ greatly, because these films are characterized by an obvious inhomogeneity with respect to composition and properties [17].

Table 3 shows the correlation of characteristic H_V values and the chemical composition of the films obtained both directly after electrodeposition and after polishing. It is apparent that a decrease in the metal phase fraction (cobalt and tungsten) and an increase in the content of carbon and oxygen lead to a significant decrease in microhardness. The indentation microhardness value for almost all samples is above 400 kgf/mm^2. For some, $H_V > 500$ kgf/mm^2. If we compare these values with the microhardness values for cobalt and tungsten (Table 2), we will see that pure metals are considerably softer than their compound (CoW). In addition, it follows from the literature data [16] that the compound of cobalt and oxygen (CoO) and the compound of tungsten and carbon (WC and W_2C) are correspondingly ~3 and ~5 times as hard as pure metals.

Analysis of the obtained values of sclerometric microhardness H_s (at scratching under load) shows the following: (a) it is significantly lower than the indentation microhardness (Table 1, Fig. 8); and (b) there exists an obviously pronounced dependence on tungsten concentration in the alloy (Fig. 8). Determination of the sclerometric microhardness is of considerable importance for an estimation of the tribological behavior of the surface, because a scratch is a single act of dynamic contact of roughness on the surface of rubbing parts. High values of sclerometric microhardness are characteristic of good tribological behavior of the mate-

Table 2. Microhardness of Co and W, and of compounds on their basis [16]

Material	Microhardness H_v, kgf/mm^2
Co	130
W	350
Co–W	400–500
WC and W_2C	1700–1800
CoO	380

Table 3. Correlation of the microhardness characteristic value and chemical composition of cobalt–tungsten electrolytic deposits

No.	Microhardness H_v, kgf/mm^2	Chemical composition, at. %			
		Co	W	C	O
1	650–550	65–70	5–8	15–20	8–10
2	550–500	60–67	6–8	20–30	7–20
3	470–450	58–62	3–5	25–30	7–10
4	410–400	40–60	2–5	20–30	9–30
5	325–300	25–30	2–4	~50	~20

rial. Furthermore, the appearance of scratches testifies to the adhesion properties of the film and the strength of its contact with the substrate. The scratches on the studied samples have a plastic form, with no brittle fractures and film splitting from the substrate. This fact testifies to the good adhesive properties of the obtained cobalt–tungsten coatings.

It is obvious that a high tungsten concentration in the layer must give the best tribological characteristics of the surface.

The results obtained in the work allow us to make the following conclusions:

First, since the EDX-spectroscopy has shown the presence of four elements (Co, W, C, and O) in all studied samples, it is reasonable to suppose that the deposited alloys are not just a solid solution of Co–W, but they may contain intermetallic compounds (e.g., CoW or Co_3W) and, probably, other possible compounds of these four elements. Such potential compounds may be tungsten carbides or oxides of cobalt and tungsten. Taking into account that carbides and oxides of Co and W are characterized by high hardness (Table 2), we can assume that their possible presence in the alloy obtained by the electrolytic method will favor a strengthening of the obtained coating.

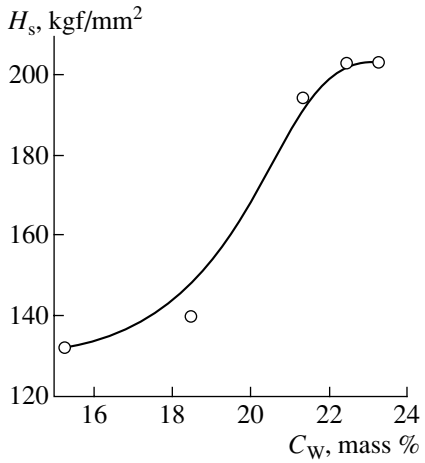

Fig. 8. Dependence of the coating sclerometric microhardness on the tungsten concentration in the alloy.

Second, if, parallel with the solid solution and intermetallic compounds of Co–W, carbides and oxides of these elements are formed in the electrochemical deposition process, directly obtaining these compounds is a challenging way to further strengthen the coatings and improve other mechanical parameters, such as wear resistance, corrosion resistance, etc. The method for the regulation of composition and structure may be the application of pulse conditions of treatment, following the results presented here.

Third, the observed decrease of the microhardness with the increasing "organic" phase content in the deposit will be a solid limitation for obtaining layers with the required mechanical properties.

It is shown in [2] that, due to an increasing *W* concentration in the alloy, the coating hardness increases, but becomes considerably more brittle. Micromechanical tests carried out by us have shown high plasticity of indentations and scratches. This means that improving the strength properties of Co–W coatings in the studied case is not accompanied by increasing film brittleness.

Compositions and structures of the coatings obtained in the present work cannot be considered optimal neither with respect to concentration of components in the alloy nor with respect to their mechanical properties. However, the correlations found between composition, structure, and mechanical properties may appear to be important for mastering the conditions for obtaining coatings of amorphous Co–W alloys with set mechanical properties. Therefore, further mastering of conditions (including the pulse ones) of electrolytic deposition of cobalt–tungsten alloys containing an optimal concentration of carbides and oxides of the given metals to obtain high-quality coatings seems to be relevant.

CONCLUSIONS

In this work, we have shown a correlation of pulse conditions for obtaining by electrolytic deposition of cobalt–tungsten films on copper substrate from the citrate electrolyte, normally used to obtain amorphous alloys, the microstructure of the obtained coatings, and their micromechanical properties determined by the

methods of microindentation and scleroscopy (scratching). It was found that variation in the electrodeposition conditions (e.g., transition from deposition on the macrosample to that on the microsample) leads to significant deviations in both layer composition and mechanical properties. It is shown that, at the same average density of current (3 A/dm^2), the composition, structure, and mechanical properties strongly depend on the frequency of the applied pulse current.

A correlation between the content of the "organic" phase (carbon and oxygen) in coatings and their micromechanical properties was found: a decrease in the microhardness H_V is accompanied by increasing content of these components. The presence of a correlation between the sclerometric microhardness, reflecting tribological behavior of the surface, and tungsten concentration in the deposited layer is shown. The results of the study can serve as a basis for further improvement of the conditions and electrolytes for electrodeposition allowing the required mechanical properties of the surface to be obtained.

The authors are grateful to S.A. Silkin and O.V. Tun'kov for help in carrying out this work.

This research was performed with partial financial support from INTAS-MOLDOVA (grant INTAS 05-104-7540) and with the support of the National Center of Material Science of the Technical University of Moldova (grant RESC-MR-995).

REFERENCES

1. Eskin, S., Berkh, O., Rogalsky, G., and Zahavi, J., Co–W – Alloys for Replacement of Conventional Hard Chromium, *Plating Surface Finising*, 1998, vol. 85, p. 79.
2. Shell, J.D. and Rechtsteiner, M., Replacement of Chromium Electroplating Using Advanced Material Technologies on Gas Turbine Engine Components, *Plating Surface Finishing*, 2000, vol. 87, p. 17.
3. Capel, H., Shipway, P.H., and Harris, S.J., Sliding Wear Behavior of Electrodeposited Cobalt–Tungsten and Cobalt–Tungsten–Iron Alloys, *Wear*, 2003, vol. 255, p. 917.
4. McHenry, M.E., Willard, M.A., and Laughlin, D.E., Amorphous and Nanocrystalline Materials for Applications as Soft Magnets, *Progr. Mater. Sci.*, 1999, vol. 44, p. 291.
5. Maruthi, B., Ramesh, L., Mayanna, S., and Landolt, D., Electrodeposition and Characterization of Co–W Alloys, *Plating Surface Finishing*, 1999, vol. 86, p. 85.
6. Admon, U. and Dariel, M.P., Microstructure of Electrodeposited Co–W Thin Films, *J. Appl. Phys.*, 1986, vol. 56, no. 6, p. 2002.
7. Abdel Hamid, Z., Electrodeposition of Cobalt–Tungsten Alloys from Acidic Bath Containing Cationic Surfactants, *Mater. Lett.*, 2003, vol. 57, p. 2558.
8. Donten, M., Stojek, Z., and Cesiulis, H., Formation of Nanofibers in Thin Layers of Amorphous W Alloys with Ni, Co and Fe Obtained by Electrodeposition, *J. Electrochem. Soc.*, 2003, vol. 150, no. 2, p. C95.
9. Ibrahim, M.A.M., Abel El Rehim, S.S., and Moussa, S.O., Electrodeposition of Nanocrystalline Cobalt–Tungsten Alloys from Citrate Electrolyte, *J. Appl. Electrochem*, 2003, vol. 33, p. 627.
10. Bobanova, Zh.I., Petrenko, V.I., Silkin, S.A., Iushchenko, S.P., and Yakhova, E.A., Electrodeposition of Amorphous Co–W alloys: Role of Hydrodynamic Conditions, *Elektr. Obrab. Mater.*, 2005, no. 6, p. 86.
11. Donten, M. and Stojek, Z., Pulse Electroplating of Rich–in Tungsten Thin Films of Amorphous Co–W Alloys, *J. Appl. Electrochem.*, 1996, vol. 26, p. 665.
12. Landolt, D. and Harlot, A., Microstructure and Composition of Pulse–Plated Metals and Alloys, *Surface and Coating Techn.*, 2003, vol. 169, p. 8.
13. Silkin, S.A., Tin'kov, O.V., Petrenko, V.I., and Tsyntsaru, N.I., Dikusar, A.I., Electrodeposition of Co–W alloys: Role of Temperature, *Elektr. Obrab. Mater.*, 2006, no. 4, p. 11.
14. Grilikhes, S.Ya., *Obezzhirivanie, travlenie i polirovanie metallov* (Defatting, Etching and Polishing of Metals), Leningrad, 1994.
15. Boyarskaya, Yu.S., Grabco, D.Z., and Kats, M.S., *Fizika protsessov mikroindentirovaniya* (Physics of Microindentation Processes), Chisinau: Stiinta, 1986.
16. Kovenskii, I.M. and Povetkin, V.V., *Metallovedenie pokrytii* (Metal Science of Coatings), Moscow: JSC Intermet Engineering, 1999.
17. Ivan'ko, A.A., *Tverdost' (spravochnik)* (Handbook of Hardness), Kiev: Naukova Dumka, 1968.

ISSN 1068-3755, Surface Engineering and Applied Electrochemistry, 2007, Vol. 43, No. 1, pp. 18–23. © Allerton Press, Inc., 2007.
Original Russian Text © S.B. Afanasyev, D.S. Lavrenyuk, P.O. Nikolaev, Yu.K. Stishkov, 2007, published in Elektronnaya Obrabotka Materialov, 2007, Vol. 43, No. 1, pp. 24–30.

ELECTRICAL PROCESSES IN ENGINEERING AND CHEMISTRY

A Semiautomatic Method for Computer Processing of the Velocity Profile in EHD Flows

S. B. Afanasyev, D. S. Lavrenyuk, P. O. Nikolaev, and Yu. K. Stishkov

St. Petersburg State University, Research and Educational Center Elektrofizika, ul. Ul'yanovskaya 1, Petrodvorets, St. Petersburg, 198504 Russia

Received October 30, 2006

DOI: 10.3103/S1068375507010036

INTRODUCTION

One of the main problems arising in studies of EHD effects and, in particular, EHD flows in weakly conducting liquids consists in visualization of these effects. The problem is mainly related to selection of light-reflecting tracers used for visualization of EHD flows, since dielectric fluids are very sensitive to impurities and additives to the fluid [1, 2].

Several methods for visualizing EHD flows are known [1–3]. The method of visualizing inclusions is one of the most popular. This method involves addition of special visible tracers (foreign particles or air bubbles) to the fluid. These tracers move with the fluid, so that in observing their motion one can determine the character of a flow, its velocity, and other parameters. However, this method imposes some constraints and requirements on the tracers. Electric conductivity of a tracer should not significantly differ from that of the studied fluid, otherwise the tracer will acquire, under the effect of an electric field, an electric charge different from the charge of the ambient fluid. As a result of this, its velocity may significantly differ from that of the fluid. A difference in the dielectric characteristics of suspended particles and the ambient fluid will result in particle motion with respect to the fluid under the effect of electrophoretic forces. The motion of suspended particles may also be affected by other phenomena and factors related to the differences between the dielectric properties of particles and the fluid surrounding them.

Dimensions of tracers should be small enough in order to, on the one hand, not distort the motion of the studied flow itself and not move with respect to the fluid under the effect of electrical and gravitational forces; and on the other hand, small enough for the tracer's tracks to be clearly distinguishable on a photo film or on a computer display. The difference between the densities of the tracer and the fluid should not be large. A tracer's boundaries should not change under the effects of electrical and gravitational forces.

This set of requirements significantly narrows the pool of substances that may be used as tracers.

In the laboratory of fluid electrohydrodynamics of the Research Institute of Radiophysics affiliated with St. Petersburg State University, small gas bubbles are used for studying EHD flows. It has been shown that if the bubbles have sufficiently small dimensions, it is the EHD flow that drives the bubbles, since the bubbles are virtually not charged by electrodes. Studies of the behavior of gas bubbles have shown that the relative error in the measurement of the velocity of an EHD flow related to individual motion of the bubbles does not exceed 5–10%. If gas bubbles are added to a fluid through a capillary tube, one can control tracer dimensions, implement the dosage of tracers, reduce pollution of a fluid to a minimum, and easily add tracers to an observation field and remove them from the field.

EXPERIMENTAL FACILITY

EHD flows are studied with a unique facility developed at St. Petersburg State University. Over a number of years, the facility's design has been improved and amended, but its conceptual design remains unchanged

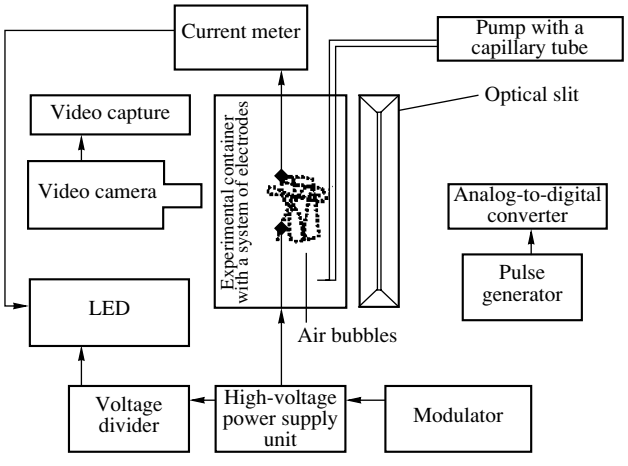

Fig. 1. Block scheme of the experimental device.

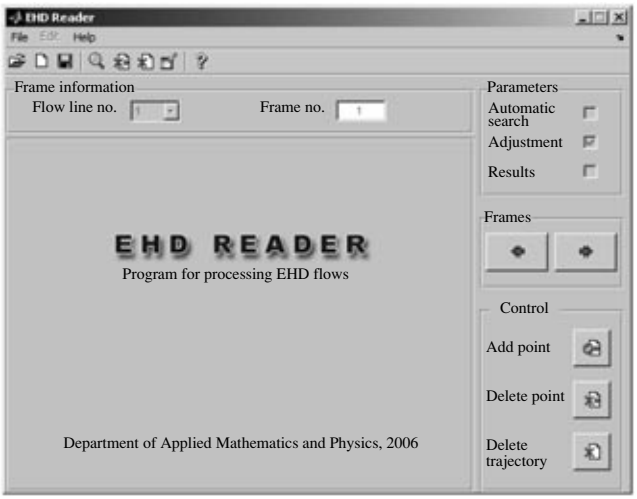

Fig. 2. Main window of the *EHD-Reader* program.

(Fig. 1). The facility consists of the following main components:

—Electric module. This block incorporates a high-voltage power-supply unit developed on the basis of a generator and a voltage multiplier. The block is intended for generation of controlled high voltage between electrodes.

—Video-channel block. This block is for recording EHD flows. The flow is recorded to a computer by a video camera and a video capture card and is concurrently displayed on the screen of a control monitor. It is also possible to make snapshots of flows.

—Pulsed flashing unit consisting of a light diode whose power is supplied from a special generator and a system of lenses with which a light beam may be focused in the studied area.

—Pneumatic channel intended for adding air bubbles of sufficiently small dimensions to a fluid through a special capillary tube.

—Experimental container, which is a rectangular vessel made of plastic and filled with the studied fluid. The container also contains a system of electrodes.

COMPUTER PROCESSING OF RESULTS

During an experiment, EHD flows are recorded on a videotape, or snapshots of the flows are made. There are a number of proprietary programs available [4, 5] that allow photos and video recordings of EHD flows to be processed with high accuracy (to do so, a film is divided into separate fields). The program operations are based on the following algorithm: a separate flow line is selected, which is represented in a photo as a set of strokes or points (depending on the duration of the flashing pulses). If the flashing pulses are short enough, location of bubbles is represented in individual fields as "points"; if, however, the pulse duration equals the half-distance between bubbles, strokes are recorded in the fields. For each trajectory, an approximating line is plotted using Bezier curves. In the points where this line crosses the strokes, marking points are set that contain information about the flow's velocity parameters. Based on the coordinates of the marking points, the program computes the components of the flow velocity in the location of strokes. Afterward, the dependence of the velocity components on the distance along a trajectory is approximated and their values are updated. Similar operations are performed for all trajectories contained in a photograph. Subsequently, information is consolidated and the data on the velocity distribution are approximated for the entire area occupied by the flow.

Below, an original program called EHD-Reader is described. This software package, developed by students and lecturers of the physical department, is based on an alternative approach to processing experimental data. The main difference from the algorithms considered above is that the stage of preliminary preparation of images in a graphics editor is skipped and data-processing operations are partly automated. The developed technique may be used for processing both photo and video images.

Developed in a MATLAB environment, the program consists of two units. One unit uploads and converts graphical data, inputs coordinates (including

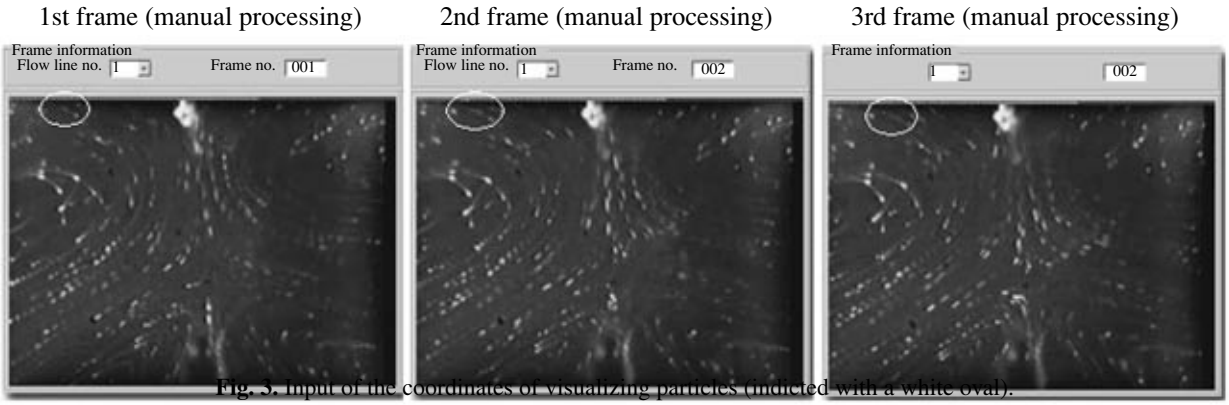

Fig. 3. Input of the coordinates of visualizing particles (indicted with a white oval).

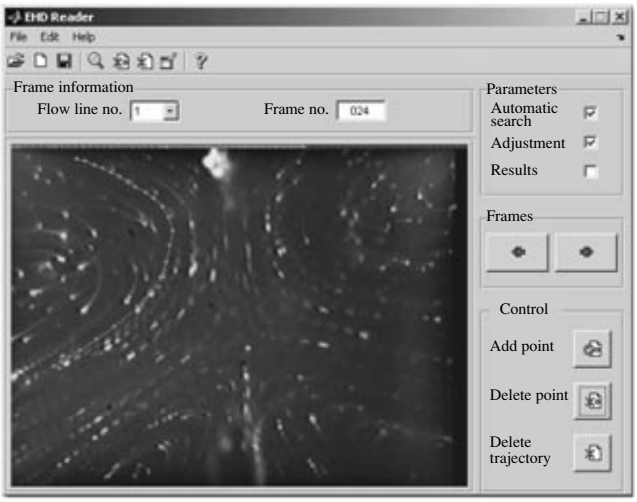

Fig. 4. Separation of a single trajectory in an EHD flow.

automatic-search elements), and removes incorrectly input points (distorted trajectories). The second unit approximates input data, constructs fields on the basis of individual points, and displays information on the screen in a graphical form. Standard tools of MATLAB libraries (Image Processing Toolbox and Spline Toolbox) are used.

After the program has been uploaded (the main window is shown in Fig. 2), it is necessary to enter the path to the directory containing a shooting sheet of the video fragment where the experiment for study of an EHD flow is recorded (File\Upload image). The window displays then the first frame of the studied sequence.

When a video film is prepared for processing of trajectories, the selected film fragment is expanded into a series of frames that are saved as separate numbered graphical files (Fig. 3).

PROCESSING OF A TRAJECTORY

Processing of an individual trajectory consists of the following operations. The position of a stroke on the selected trajectory in the current frame is indicated with the "mouse" and fixed by clicking the "Set point" button. When the button is clicked, the cursor coordinates are read and sent to a function that determines the brightest pixel near the selected point, converts it into a binary form according to the set level, selects the object containing this pixel, and returns the coordinates of this object's center. Graphical objects may be handled with the tools available in the Image Processing Toolbox library. The zoom function (Edit/Zoom) function enables one to increase input accuracy.

After coordinates of three points have been entered manually (Fig. 3), coordinates of the next points may be found automatically. To do so, one should tick the "Parameters/Automatic search" checkbox. An approximation parabola is constructed using the three last points, and the new point is searched for in its vicinity. If the automatic mode operates unsatisfactorily, the user may delete a point input earlier or an entire trajectory (the "Delete point" and "Delete trajectory" buttons) and enter coordinates manually as it described

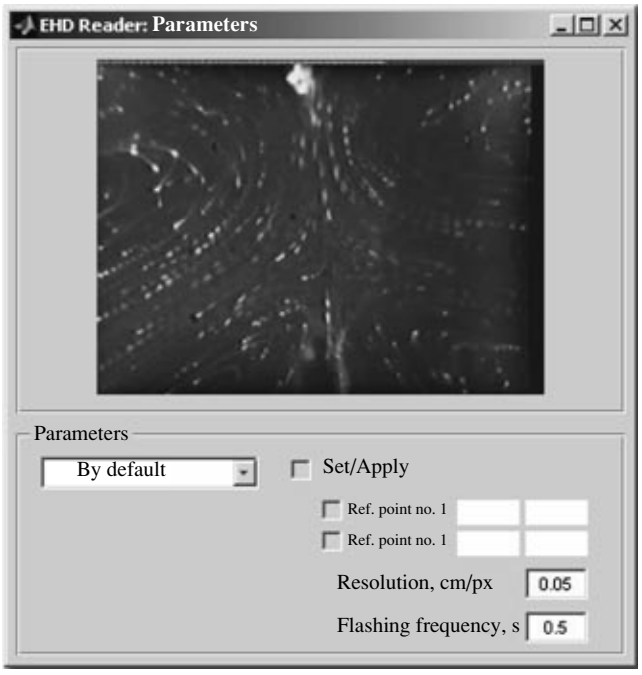

Fig. 5. Window for setting parameters of an EHD flow.

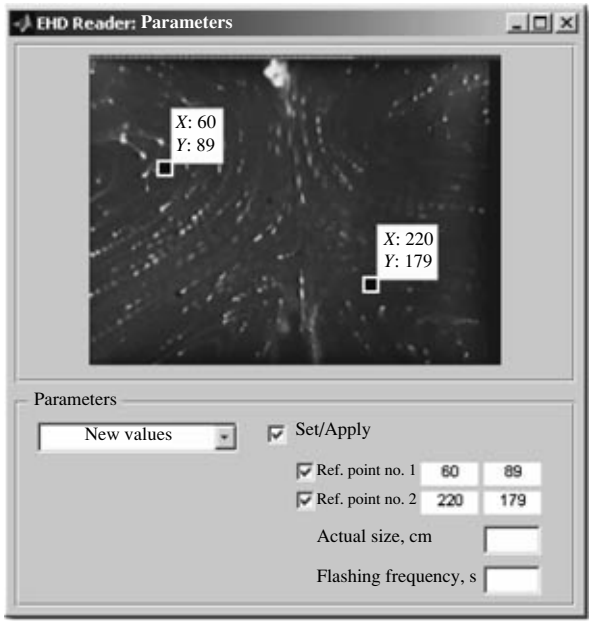

Fig. 6. Manual setting of the parameters of an EHD flow.

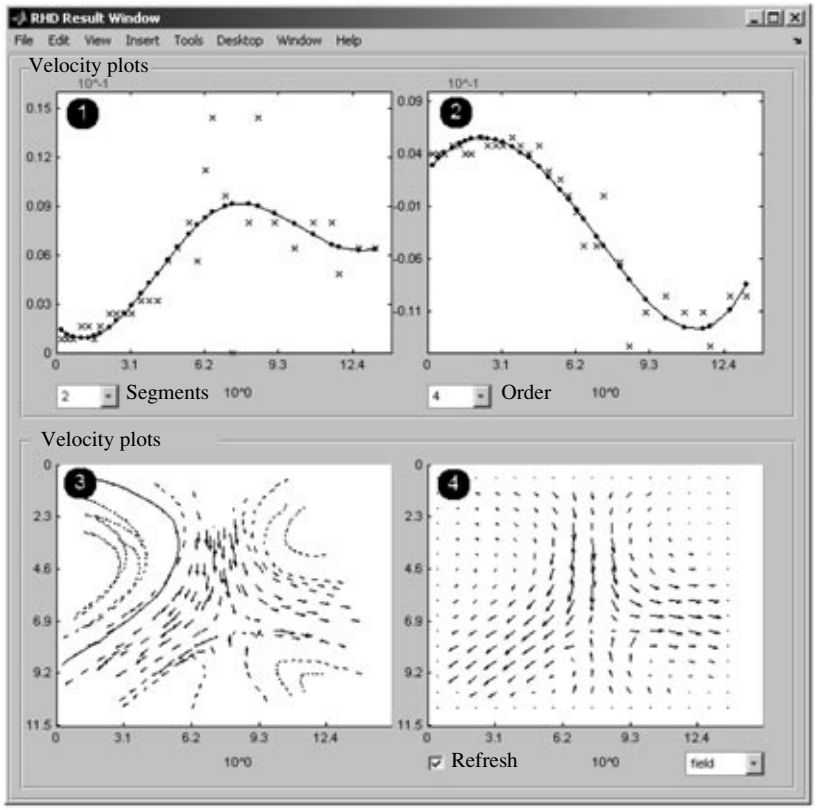

Fig. 7. The window of *EHD-Reader* program results.

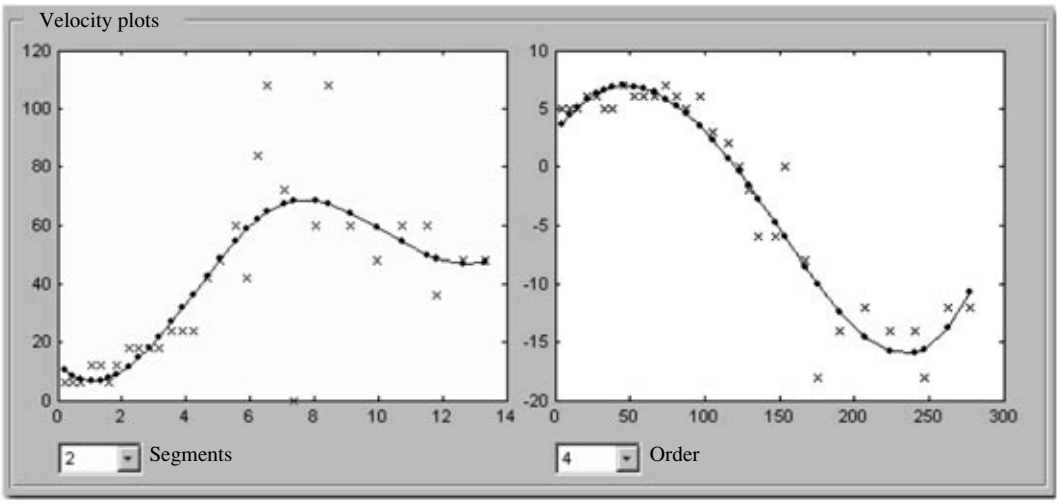

Fig. 8. *X* and *Y* components of a particle's velocity along a selected trajectory.

above. As a result, a processed trajectory is obtained (Fig. 4).

PARAMETERS

Image dimensions are set in the program in pixels so that processed data are not informative. To transfer to actual dimensions during the processing operation, one can use the "Parameters" dialog (Fig. 5) called up by the respective button or from the toolbox or from the "Edit" tab of the main menu.

The popup menu prompts three options for setting parameters:

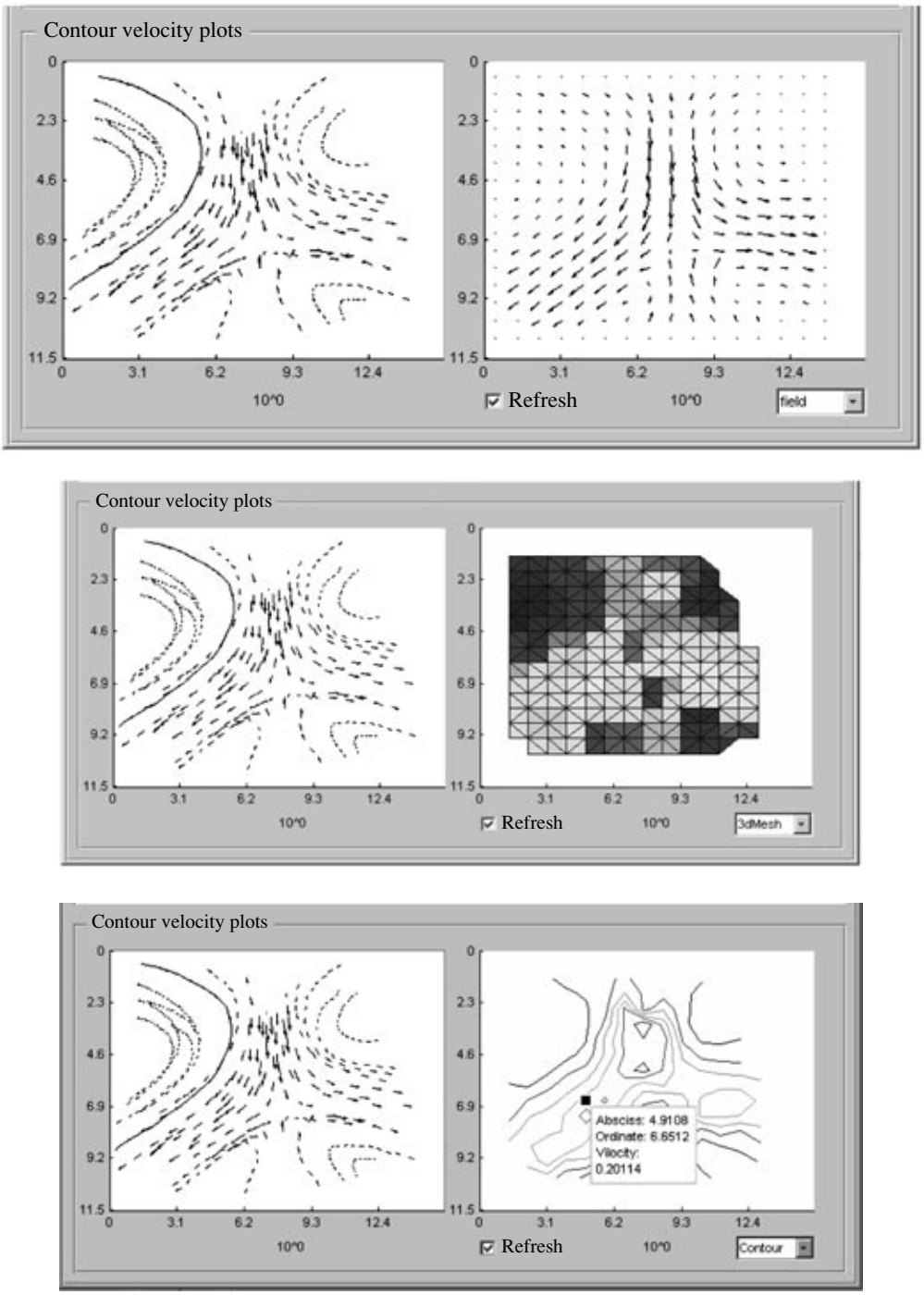

Fig. 9. Contour plots of the velocity field of an *EHD* flow displayed as (*1*) a vector field, (*2*) a 3D mesh, and (*3*) contour plot.

(i) *default values*: the values incorporated in the program that are used most frequently;

(ii) *previous session*: the value of the parameters set by the last user during the program sessions are used;

(iii) *new values*: parameters are set manually. Let us consider this option in more detail.

Manual Setting of Parameters

The main task performed by the user is to set the resolution to be used by the program, i.e., the value measured in cm/pixel that determines the number of centimeters per pixel of image. To do so, the user should tick the "Set/Apply" checkbox (Fig. 6). Using the cursor

(which changes its shape to a cross) location of two reference points on the image is indicated. (Any pair of points may be used for this.)

After the coordinates of the reference points have been determined, the actual distance between these points (expressed in centimeters) is set in the "Actual dimension" line.

Another important parameter is "Flashing frequency," i.e., the time interval between two adjacent frames. This parameter is expressed in seconds.

After all parameters have been set, the "Set/Apply" checkbox should be cleared, otherwise the changes will not be enabled. The parameters will be saved after the window closes; subsequently, they will be available as described in the "Previous session" item.

RESULTS

After all of the flow lines of interest for the user have been processed, the data may be analyzed in the "Results" window (Fig. 7). The window consists of two parts displaying, respectively,

(i) the *X* component of the velocity plotted as a function of the abscissa value;

(ii) the *Y* component of the velocity plotted as a function of the ordinate value;

(iii) the vector plot of the velocity field with the track highlighted;

(iv) the contour plots of the velocity field.

VELOCITY COMPONENTS

After photos have been processed, velocity components of tracers become available (Fig. 8). However, these quantities are only known at certain discrete time moments. To determine the dependence of a particle's velocity on its position within the interval between electrodes, the data are approximated by splines using the least-squares method.

The "Segments" parameter sets the number of segments in the approximating spline, and the "Order" parameter determines the order of that spline.

DISPLAY OF PROCESSED EXPERIMENTAL RESULTS

After each of the current-flow lines has been processed separately, the overall picture of the EHD flow may be constructed. The "Contour plots" section offers different options for display of the studied velocity field (Fig. 9).

(i) vector velocity field (Field);

(ii) 3D mesh (display in the form of a color palette);

(iii) contour plot (Contour) of velocities showing data as velocity levels. Having clicked a point of interest, the user will see its coordinates and the absolute value of the velocity displayed on the screen.

Thus, the described program allows the user to construct the velocity field of an EHD flow observed in an experiment. The processed results may be displayed in one of three forms (Fig. 9) and used for further processing and determination of the velocity at any point in the interval between electrodes.

REFERENCES

1. Stishkov, Yu.K. and Ostapenko, A.A., *Elektrogidrodinamicheskie techeniya v zhidkikh dielektrikakh* (Electrohydrodynamic Flows in Fluid Dielectrics), Leningrad, 1989.
2. Stishkov, Yu.K., Main Stages in Development of Electrodynamics in the Research Institute of Radiophysics of St Petersburg State University, *Sb. dokladov "Problemy difraktsii i rasprostranenie radiovoln"* (Collection of Articles "Diffraction Problems and Propagation of Radio Waves"), St. Petersburg: Izd. SBbGU, 2000, vol. 28, p. 229.
3. Sekino, Y., Ohayama, R.-I., and Kaneko, K., Measurements of Unsteady EHD Flows from Injection Studies on Free Surfaces by Particle Report Image Velocimetry, *Ann. Rep. Conf. Electrical Insulation and Dielectric Phenomena*, Atlanta (USA): OMNIPRESS, 1998.
4. Pavleino, M.A. and Stishkov, Yu.K., Computer Processing of Electrohydrodynamic Experiments, *Sb. dokl. VI mezhd. nauch. konf. po sovr. problemam elektrofiziki i elektrogidrodinamiki zhidkostei* (Proc. VI Int. Scient. Conf. on Modern Problems in Electrophysics and Electrohydrodynamics of Fluids), 2000, pp. 4–9.
5. Buyanov, A.V., Pavleino, M.A., and Stishkov, Yu.K., *Effect of External Factors on the Main Characteristics of EHD Flows* (Proc. VI Int. Scient. Conf. on Modern Problems in Electrophysics and Electrohydrodynamics of Fluids), 2000, pp. 87–92.

ISSN 1068-3755, Surface Engineering and Applied Electrochemistry, 2007, Vol. 43, No. 1, pp. 24–35. © Allerton Press, Inc., 2007.
Original Russian Text © M.S. Apfel'baum, 2007, published in Elektronnaya Obrabotka Materialov, 2007, Vol. 43, No. 1, pp. 31–46.

ELECTRICAL PROCESSES IN ENGINEERING AND CHEMISTRY

Distribution of Electric Fields in Certain Types of Stationary Weakly Ionizing Jets

M. S. Apfel'baum

Institute of Thermal Physics of Extreme States, Russian Academy of Sciences, ul. Izhorskaya 13/19, Moscow, 125412 Russia

Received October 11, 2006

DOI: 10.3103/S1068375507010048

The theoretical models for the creation and transport of a volume charge during thermal ionization (thermal dissociation) of immobile and moving weakly conducting media (as well as in an electric field) described in this study represent the natural development of the models published in [1, 2] for the case of nonisothermal processes. As before, we assume that thermal ionization (thermal dissociation) evolves according to the laws of classical Arrhenius–Boltzmann–Gibbs statistics and the kinetics and the rate of such ionization (dissociation) per time unit and per unit volume $W_{D,I}$ satisfies the known equation of statistical physics (mechanics)

$$\frac{\partial W_d}{W_d \partial T} = \frac{u_a}{k_B T^2}, \quad \frac{\partial W_{Ii}}{W_I \partial T} = \frac{u_i^A - u_e^B}{k_B T^2}. \tag{1}$$

In (1), k_B is the Boltzman constant, T is the absolute temperature, u_i^A is the potential of ionization of an A atom in the molecule of a medium with covalent chemical bonds, and u_a is the activation energy of the molecules in media with ionic bonds. In the case of dissociation, an analog of Eq. (1) for the constant of such a process introduced below is presented together with the ionization constant in [3] (in [3], self-dissociation of impurity-free weakly conducting media and the effect of a strong electric field on such media are studied; heptane, widely used in practice, is considered an example of such a medium). If a medium contains impurities,[1] which usually increase the natural conductivity of a purified medium σ_0, in calculating $u_{a,i}$, it is necessary to take into account the characteristics of the impurities affecting thermal ionization (thermal dissipation). To apply such statistical kinetics with electron which are similar to those widely used in statistical physics (mechanics), we also introduce a well-known hypothesis according to which the volume rate with which ions are produced $W_{D,I} = W_{D,I}(n_a, n_p)$ linearly depends on the concentration of neutral molecules n_a (taking into account the fact that the latter monotonically increases when the absolute value of E grows, being limited by the absolute value of the electric-breakdown field; it increases as well when the (sufficiently small) concentration of admixtures n_p that may be present in the medium prior to its purification grows) with the respective proportionality factor K,

$$W_{D,I}\left(n_a, n_p, T, \left|\vec{E}\right|\right) = K_{D,I}\left(n_p, T, \left|\vec{E}\right|\right) n_a;$$
$$K_{D,I}\left(n_p, T, \left|\vec{E}\right|\right) = K_{D,I}(n_p, T, 0)\psi\left(\left|\vec{E}\right|, T\right)/\psi(0, T). \tag{2}$$

$$\psi\left(\left|\vec{E}\right|, T\right) > 1, \quad T > T_0, \quad \partial\psi/\partial T > 0, \quad n_\pm \ll n_a \tag{3}$$

which mathematically closes the set of differential equations used in the theoretical models of earlier studies, for example [1, 2]. We assume that for the considered media a similar algebraic inequality holds:

$$n_p \ll n_a. \tag{4}$$

We then have $n_a = \frac{\rho_a}{m_a} \approx \frac{\rho}{m_a}$; i.e., the density ρ of the mixture as a whole may be approximately considered equal to that of the neutral component of the molecular carrier medium ρ_a. Here, m_a is the mass of the neutral particle. Integration of (1) yields

[1] In particular, according to the data of [4], the low-voltage conductivity of a purified transformer oil determined on the basis of current–voltage characteristics is an order of magnitude smaller than that of unpurified oil. To increase conductivity, special easily ionized additive agents (mixtures) are often added to such media [5]. In this study, ionization of AB molecules with covalent bindings of type $2AB \longrightarrow A^+B + AB^-$ as well as dissociation of molecules with ionic binding of type $AB \longrightarrow A^+ + B^-$ are considered. In the case of ionization, media with molecules consisting of atoms A (like nitrogen in the air) with a sufficiently low ionization potential and atoms B (like oxygen in the air) with a sufficiently high electron affinity energy are considered.

$$\begin{cases} W_d = C_d \exp\left(-\dfrac{u_a}{k_b T}\right); & (5a) \\ W_I = C_I \exp\left(\dfrac{u_e^B - u_i^A}{k_b T}\right). & (5b) \end{cases}$$

To increase the absolute value of the flow velocity of weakly conducting fluid media in a strong external electric field (Fig. 1), admixtures are added whose compositions differ from those indicated in [5]. Such admixtures enhance the electrophysical or electrochemical near-electrode ionization effects described, for example, in [6] (in both uniform and nonuniform strong electric field) owing to which the flows of the considered media in such fields become more active. In this study, media with specially added admixtures are not considered. Apart from the purified media, only media with admixtures present a priori are considered. The coefficient of proportionality in linear dependence (2) between the rate of production of simple and complex (depending on the molecular composition of the considered medium) ions and the concentration of neutral particles, which is known in physicochemical publications as the constant of ionization (dissociation), is assumed to grow if the temperature and the absolute value of macroscopic electric field $\vec{E}$ increase, this circumstance being taken into account in the mathematical form of (2). Generically, such field should be considered electromagnetic; however, as it was shown in [7], in weakly conducting (weakly ionized) media, the effect of the induced magnetic fields on the studied electromagnetic phenomena is so small that the magnetic fields originating from an external source are not considered in this study. For theoretical description and calculations of electrohydrodynamic characteristics, it is sufficient then to use the electrohydrodynamic approximation [8], where the system of Maxwell equations for the macroscopic magnetic fields decouples from the main system of equations and may be not considered at all. The same refers to the equations describing variations in the concentration of admixtures, which is small relative to the concentration of the molecules of the carrier medium. However, unlike a magnetic field that weakly affects the considered processes in the polarizable but not magnetizable media, the admixtures, as was noted above, affect the medium's conductivity. Therefore, it should be noted that the possible types of equations for the volume concentration of admixtures are very similar to the equations for the same concentration of charged components presented here. The latter equations are presented below and possible types of equations for admixtures are also indicated. The macroscopic Maxwell equations for the strength of the sought electric field for the case of the constant relative dielectric permittivity of considered media ε_r may be presented in the standard form:

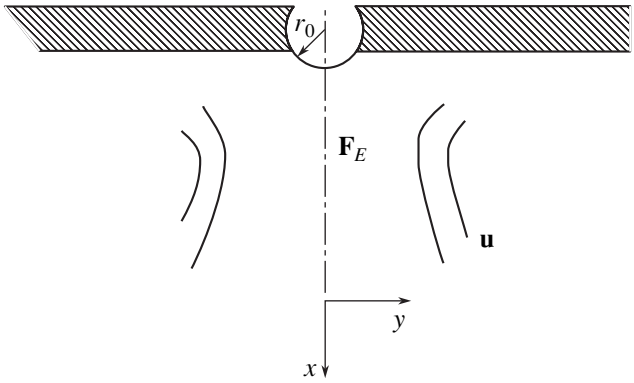

Fig. 1. The simplest layout of electric wind (flow of a weakly conducting fluid in a strong electric field).

$$\begin{cases} \operatorname{div}\vec{E} = \dfrac{q}{\varepsilon_r \varepsilon_0}; \\ \vec{E} = -\nabla\varphi. \end{cases} \quad (6)$$

System of equations (6) may be reduced to a single scalar Poisson equation of the second order for the potential of macroscopic electric field φ. The methods for solving the boundary problems for such an equation whose right-hand side explicitly depends on spatial coordinates are well known. However, in the case of prebreakdown processes, the right-hand side of this equation depends on the electric-field distribution; therefore, the Poisson equation should be solved in combination with other equations presented below. In Eqs. (6), $q = (n_+ - n_-)Ze_0$ is the density of the volume charge and ε_0 is the permittivity of free space expressed in the SI system of units. In the absence of an applied strong electric field or before heating, the considered media (beyond the diffuse layers near their boundaries) are electrically neutral. Their low-voltage conductivity σ_0 at a constant temperature T_0 before heating is related to the presence in the medium's volume of equal concentrations of charges $n_{0+} = n_{0-} = n_0$ that have different signs. The quasi-neutral background of positively and negatively charged particles may appear in a medium that does not alter, as a whole, its content in accordance with (1) owing to volume thermal ionization (thermal dissipation) phenomena enhanced in prebreakdown electric fields or when the considered media are heated or partly burned. According, for example, to [1, 7], this results in the formation of a volume charge characterized by a nonuniform distribution of electric fields and temperatures in the considered viscous and sufficiently dense media where, in contrast to dilute gas, mobility hardly depends on the absolute value of the electric-field strength. In addition, such a charge (according, for example, to [6]) may be created near the boundaries of the considered media with high-voltage electrodes. The possible appearance of such a charge at other boundaries with solid, liquid, or gaseous media should be

studied. If the considered medium moves (also in the presence of a strong electric field), the hydrodynamic (gas-dynamic) transport of the forming volume charge also affects its spatial distribution. We studied earlier such an effect emerging in the volume of a moving medium (see for example [2]), and it will be discussed below in this study. The gas-dynamic transport of such a charge near the boundaries of the considered media in the conditions of possible breakdown has been described, for example, in [5]. The value of σ_0 may be found theoretically from the condition of ionization (dissociation) equilibrium determined by ionization (dissociation) of the fluid (gas) molecules and recombination of the charged particles, which has about the same rate. The rate of volume ionization (dissociation) is then determined according to (2), while the recombination rate may be considered proportional to ionic concentrations $n_\pm$ with proportionality factor K_r. Such conductivity may be determined experimentally from the linear segment of voltage–current characteristics observed, in the case of the considered media, only in weak fields. The conductivity value may be found in handbooks or calculated by physical-kinetics methods.

Dependence of recombination factor (or constant) K_r on ionic mobility of charges $b_\pm$ may be found from the simple Langevin–Onsager relation [9]:

$$K_r = \frac{(b_+ + b_-)Ze_0}{\varepsilon\varepsilon_0}. \tag{7a}$$

For simplicity, the charges of positive and negative free (in the case of dissociation, according to Bierrum [9]) ions are assumed to be multiples of the multiplicity value (valence Z). Herein, the value of e_0 is set equal to the proton charge. For a larger multiplicity (valence) of an ion's charge, e_0 should be multiplied by the corresponding factor. Formula (7a) is derived under the assumption that the velocity of charges $\vec{v}_{\pm\vec{E}_0}$ moving under the effect of an electric field is proportional to its (macroscopic) strength $\vec{E}$, ionic mobility being the corresponding proportionality coefficient. In addition to these velocities of the charges, it is necessary to take into account their velocities that are due to molecular-ionic diffusion according to Fick's law [9] $\vec{v}_{\pm\vec{E}} = \frac{D_\pm \nabla n_\pm}{n_\pm}$ as well as the velocity of hydrodynamic transport $\vec{u}$. Under conditions (3) and (4), this velocity may be considered close to that of the medium. Coefficients of ionic diffusion $D_\pm$ are related, under the assumption of ideal plasma, to their mobility values $b_\pm$ by the known Nernst–Townsend–Einstein equation

$$D_\pm = \frac{k_B T}{Ze_0} b_\pm. \tag{7b}$$

The velocities of the elementary volumes of charged components are then

$$\vec{u}_\pm = \vec{u} \pm b_\pm \vec{E} - \frac{k_B T b_\pm}{Ze_0}\frac{\nabla n_\pm}{n_\pm}. \tag{8}$$

Apart from Fick's approximation (8), other models may be used to determine the macroscopic components of the medium's components. For example, to determine $\vec{u}$ (velocity of the neutral component) taking into account viscosity under conditions (3) and (4), the Navier–Stokes equations [10] are used:

$$\begin{cases} \rho\left(\dfrac{\partial \vec{u}}{\partial t} + \vec{u}\nabla\vec{u}\right) = -\nabla p + \rho\nu\Delta\vec{u} + \rho\vec{g} \\ + q\vec{E} + \dfrac{(\varepsilon_r - 1)\varepsilon_0 \nabla(\vec{E}^2)}{2}; \\ \dfrac{\partial \rho}{\partial t} + \mathrm{div}(\rho\vec{u}) = 0. \end{cases} \tag{9}$$

In formula (9), p and ν are the pressure and kinematic viscosity, respectively, of the medium's neutral component, which are close, under conditions (3) and (4), to the corresponding characteristics of the medium itself; t is time, and $\vec{g}$ is the gravity acceleration.

The formula for the volume density of the electric-field force contained in (9) may be derived in accordance with [11]. For incompressible media, the second equation in (9), which is a consequence of the mass-conservation law, is simplified, since, in the case of isothermal regimes, the condition of constant density $\rho = \rho_0$ is satisfied for such media. In addition, since the concentration of possibly present uncleared impurities n_p is small (relative to the concentration of the neutral molecules of the carrier medium), the respective partial differential equations used, for example, in [12], to determine the spatial and time distributions of this concentration are not considered in this study. Such differential equations with corresponding initial and boundary conditions may be qualitatively studied or quantitatively solved after having decoupled and solved the electrohydrodynamic equations for the density, velocity, pressure, and temperature of the carrier medium; the densities of charged components; and the electric-field potential. It should be noted that for a broad class of dispersive media, the distribution of the impurity concentrations satisfies the known equation of convective diffusion. In some studies, for example [12], the value of n_p is determined by applying the equation of such diffusion in Fick's approximation, which is used here for ionic components. Outside the diffusion layers near the boundaries of the considered media, we will use a partial solution of such an equation that is invariable in space and time, assuming that the concentration of impurities before application of a strong electric field or heating of the medium is leveled with time increasing by diffusion of impurities and affects con-

ductivity in accordance with (1). In the dissociation case, one should distinguish media with self-dissociation [3] and with dissociation of impurities (a kind of weak electrolytes) considered, for example, in [9]. The weakly electrolytic isothermal case where only impurity molecules dissociate may be studied theoretically similarly to the case of dissociation (ionization) of the neutral molecules of the carrier medium (namely, in functional dependences (2), as well as the formulas presented below, the concentration variables of the neutral components of the carrier medium and the admixtures should be swapped). The case of nonisothermal creation of charges is considered in this study only provided the rate of ionization (dissipation) of the neutral molecules in the carrier medium is proportional to the concentration of those molecules.

The continuity equation for charged components may be represented, taking into account relation (8) and Fick's diffusion law, as follows [13]:

$$\frac{\partial n_\pm}{\partial t} + \operatorname{div}\left[n_\pm(\vec{u} \pm b_\pm \vec{E}) - \frac{k_B T b_\pm}{Z e_0} \right] = K_{\mathrm{D,I}}(n_\mathrm{p}, T, |\vec{E}|) n_\mathrm{a} - K_r n_+ n_-. \quad (10)$$

These equations are derived in vector form, for example, in [13], by differentiating the field of a time-dependent vector in the moving volume of the continuous medium (the issue of correctness of the continuous-medium approximation with a weak degree of ionization (dissociation) of its charged components is not discussed here.) In the isothermal conditions and if the concentration of admixtures is small (4) and density is constant $\rho = \rho_0$, the system of equations (10) combined with Eqs. (6) and (9) becomes mathematically closed.

If $\vec{E} = 0$ and $T = T_0$, the value of $K_{\mathrm{D,I}}$ may be found from σ_0, i.e., the value of conductivity under such conditions. Namely, this may be done using equality $W_{\mathrm{D,I}} = W_r$ in absence of heating and a strong applied electric field (beyond the boundary layers close to the boundaries of the considered area where diffusion may be effective):

$$C_I = \frac{\sigma_0^2 \exp\left[\frac{u_e - u_i(0)}{k_B T_0}\right]}{Z\varepsilon_r \varepsilon_0 e_0 (b_+ + b_-)\rho_0}, \quad C_D = \frac{\sigma_0^2 \exp\left[\frac{u_i(0)}{k_B T_0}\right]}{Z\varepsilon_r \varepsilon_0 e_0 (b_+ + b_-)\rho_0},$$

$$u_{a,i} = u_{a,i}(|\vec{E}|) \quad (11)$$

$$K_{\mathrm{D,I}}(n_\mathrm{p}, T_0, 0) = \frac{\sigma_0^2 n_\mathrm{a}}{Z\varepsilon_r \varepsilon_0 e_0 (b_+ + b_-)\rho_0}.$$

Equations (11) were derived on the basis of Eqs. (5), which are known in physics and chemistry literature as Arrhenius-type equations, and the Langevin–Onsager relation (7a). In addition, Onsager has considered in [9] the effect of a strong electric field on dissociation constant K_D for "loose" ionic pairs and has shown that such a field does not affect recombination of the pairs. The effect of the electric field on K_D may be described[2] only via the effect of $\vec{E}$ on u_i (Frenkel–Plumley model [3, 14] for the case of ionic conductivity). Both the Onsager model [9] and the Frenkel model for ionization [14] or Plumley model for dissociation [3] that are applied here are based on classical Arrhenius–Boltzmann–Gibbs statistics and kinetics [15]. In the Onsager theory [15], transition to macroscopic values is made after having found solutions of an equation of the Boltzmann-equation type [8, 15] for the distribution function of the ensemble of the free charges created as a result of dissociation in an applied electric field, rather than after having solved sufficiently simple Eq. (1).

To close, in a mathematical sense, differential Eqs. (9)–(11) in the case of heating or partial burning of the considered media, a differential equation for heat inflow is required as well as the algebraic equation of state:

$$\rho = \rho(p, T). \quad (12)$$

For an ideal and perfect gas, function (12) may be represented in the form [13]

$$p = \rho k_B T / m_\mathrm{a}, \quad (13a)$$

and for an incompressible fluid under isothermal conditions (in the Boussinesq approximation) in the form [12]

$$\rho = \rho_0[1 - \gamma(T - T_0)]. \quad (13b)$$

The equation for heat inflow taking into account Joule heating for temperature T may be represented, with the energy contribution relative to polarization, viscosity, and chemical relations being neglected, as

$$\rho c_v \left(\frac{\partial T}{\partial t} + \vec{u} \nabla T \right) = \operatorname{div}(\lambda(T) \nabla T) + \sigma \vec{E}^2. \quad (14)$$

In Eq. (13b), the specific coefficient of thermal expansion is considered constant. In Eq. (14), the thermal capacity for a constant specific volume for an ideal gas and incompressible fluid is also a constant. How-

[2] Reduction of ionization potential ΔU_i by an electric field is described, according to [14], by a simpler formula: $\Delta U_i = \int_{r_M}^{\infty} \frac{e_0^2 dr}{4\pi\varepsilon\varepsilon_0 r^2}$. Here r_M is the maximum height of the potential barrier in the Coulomb attraction of nuclei and electrons in the field. Also $\frac{e_0^2}{4\pi\varepsilon\varepsilon_0 r_M^2} = e_0|\vec{E}|$ (change in the work function according to [18] and the binding energy u_a of a molecule with the particle charge $|e| = Ze_0$ according to [3] are calculated in a similar way). If the work of the electric field is taken into account, the value of such a reduction should be doubled according to [3, 14, 18]. In addition, we assume that a strong electric field affects neither electron affinity nor, according to [9], the recombination factor.

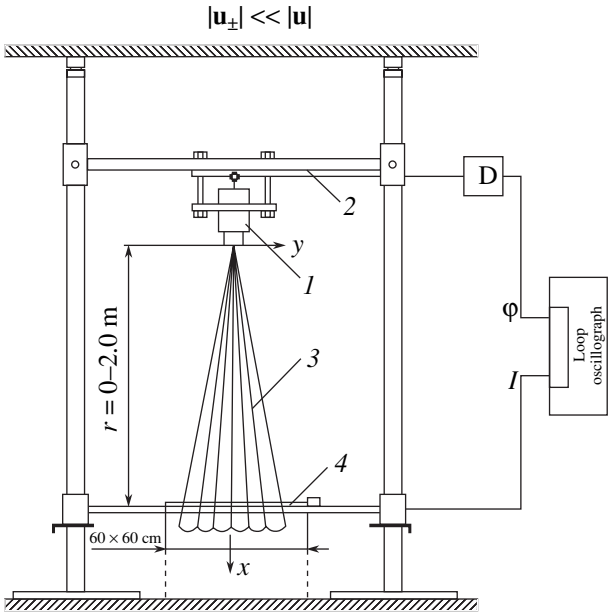

Fig. 2. Layout of experiment [21] for determination of the distribution of the potential in thermally ionized jets: (*1*) thermal diffuser; (*2*) fixing device; (*3*) jet; and (*4*) electrode for determination of the potential.

ever, heat conductivity is assumed, for example, in the case of an ideal gas with equation of state (13a) to be linearly dependent on temperature. For media with equation of state (13b) incompressible under isothermal conditions, heat conductivity may be considered to be weakly dependent on T. The thermal gas-dynamics equation neglecting thermal ionization (thermal dissociation) of the considered media and formation of a volume charge are usually represented by all authors as Maxwell equations for a microscopic electric field. However, different authors represent the thermal electrodynamics equation of type (10) in different forms. For example, for ionic concentration $n_\pm$, instead of equations with diffusion (10), a momentum-conservation equation of type (9) may be used in the form

$$\rho_\pm \vec{a}_\pm = -\nabla p_\pm + \vec{f}_\pm. \qquad (15)$$

Here $\rho_\pm$ are densities and $\vec{a}_\pm$ are kinematic accelerations of infinitesimally small (in a physical sense) volumes of the mixture's charged components, and p and $\vec{f}_\pm$ are the pressure and volume densities of the external forces acting on those volumes. Depending on the properties of ions, in analyzing mathematical relationships for the densities of the resulting external forces, the forces related to viscosity may be taken into account or neglected. In Fick's approximation [15–18], viscosity is not taken into account for charged components (unlike the neutral component) under condition (3); however, according to [2, 19], it should be taken into account when those components are created. Macroscopic Eqs. (15) may be derived not only by the methods of continuum mechanics described, for example, in [10, 13], but also from their microscopic analogs by determining the corresponding momenta of the Boltzmann kinetic equation for the distribution function of microparticles [8, 15]. In deriving the expression for force densities $\vec{f}_\pm$, one may also take into account the effect of these forces on collisions between charged and neutral components, which is often studied in the physics of nonideal and partly ionized plasma [20]. For example, macroscopic equations for the momenta of charged components are represented in [21] as

$$\begin{cases} \rho_\pm \vec{a}_\pm = -\nabla p_\pm + n_\pm Z e_0 \vec{E} + \alpha_\pm n_\pm (\vec{u} - \vec{u}_\pm), \\ p_\pm = n_\pm k_B T. \end{cases} \qquad (16)$$

Here $\alpha_\pm$ are the constants that may be determined from the characteristics of collisions between charged components and neutral molecules. In addition, the equation of state for ionic components (16) is represented in approximation (13a) for an ideal ionic gas. In the case of a nonideal ionic gas, these equations may become more complex if collisions with charged components and between neutral components are taken into account. More often relation (16) is replaced with equations for momenta or flows thereof derived either in Fick's approximation or according to the Euler approach (without taking viscosity into account) in combination with the corresponding mass continuity equations presented above. Equations (16) for ionic components are partly similar to both models. For example, Eqs. (16) contain all the terms that are contained in the momentum equation (except the viscous-friction forces). It is such an approximation that is called the Euler equations for a nonviscous gas. Unlike the Euler equations or (viscosity being taken into account) the Navier–Stokes equations, formula (16) contains a term that takes into account collisions of uncharged and charged components whose quantitative effect is proportional to relative velocities. In finding the characteristics of gas-dynamic jets heated to the temperature of low-temperature plasma, study [21] assumes that they obey the conditions of local thermodynamical equilibrium.

In this approximation, $\vec{a}_\pm = 0$ and Eqs. (16) reduce to Fick's diffusion equations (8). In study [21], these equations, which are generically not closed in the mathematical sense, were solved for the case

$$|\vec{u}_\pm| \ll |\vec{u}|. \qquad (17)$$

Approximation (17) is justified for the distribution of the potential field induced in heated turbulence gas-dynamic jets (Fig. 2). Equations (16) become closed with Maxwell equation (5). If quasi-neutrality is assumed, which is typical of plasma media with $T >$ 1000 K [20, 21], Eq. (16) may presumably be solved without involving Maxwell equation (5). This was the

method that was used in [21] to solve these equations. In the general case, even if distribution of u and T are given, Eqs. (5) and (16) are not sufficient to obtain mathematically closed equations of thermal ionization (thermal dissociation); they have to be completed with continuity-type equations (10). Such an approach was used in [22] to amend theoretical solutions for the electric potential of thermal ionized immersed jets that do not flow around solid walls, which was published in [21].

However, in deriving solution in [21], the contribution from diffusion and charge drift in an electric field was taken into account, while in [22] only the contribution from the hydrodynamic transfer of the volume charge created in a heated jet was considered and no assumption regarding plasma quasi-neutrality has been made. Generalization of and amendments to the results presented in report [22] are described below in this study. The theoretical model of [21] is hardly applicable to calculations of the characteristics of thermal ionization (thermal dissociation), conductivity, and fluxes in the region of strong electric fields, in particular, to [23]. However, the theoretical model for calculating the thermal physical and electrical-engineering characteristics of weakly ionized (weakly dissociating) heat carriers used in energy-generating facilities considered here may also be used for strong applied electric fields (Fig. 1). In contrast to our earlier publication [24], in this study, another formulation of the problem is considered for constant $p = p_0$ in the spatial area. Namely, we consider the effect of a weakly conducting (weakly ionized) medium's pressure on the current–voltage characteristics in a strong applied nonuniform electric field (in [24], the problem has been solved only in application to experimental results [23] where a special vacuum pump was used to change pressure p_0; the experiment also involved the study of the effect of this pressure on the measured Townsend (observed) corona-ignition voltage U_k). A more complex (as compared to [24]) problem is solved here, since the results of [24] cannot be used for calculating the energy consumed by electric filters as a function of the ambient pressure and the pressure p_0 of the medium undergoing cleaning in these devices (which have been commercially used for a long time). To do so, as in our earlier studies, we use a reduced (simplified) system of Eqs. (5)–(10) not taking diffusion into account. In addition, we neglect the effect of electric-wind jets as hydrodynamic (gas-dynamic) transport of the generated volume charge on potential φ. When the difference between mobility values $b_\pm$ are taken into account, this system differs,[3] from a similar system presented, for example, in [1] by additional terms:

$$\begin{cases} q = -\varepsilon_r\varepsilon\vec{E}\nabla\sigma/\sigma \ (-\vec{E}\nabla\sigma/\sigma = \operatorname{div}(\vec{E})); \\ \varepsilon_r\varepsilon b_+ b_- \vec{E}\nabla q = \sigma_0^2\dfrac{\Psi(|\vec{E}|, T)}{\Psi(0, T_0)} - \sigma^2 + (b_+ - b_-)q\sigma; \\ \vec{E} = -\nabla\varphi. \end{cases} \tag{18}$$

In deriving (18), in addition to Langevin formula (7a), Eq. (11) was used. If impact ionization by free electrons in a strong electric field, which is more typical of dilute gases, is neglected, the explicit form of additional-ionization function $\Psi(|\vec{E}|, T)$ may be derived according to Frenkel or similarly, in the case of dissociation, according to [3] and Onsager [9].

The conditions under which one may neglect diffusion and convective components of current densities have been derived in [2]; they are part of the conditions for similarity between ionization (dissociation) and recombination. In this case, the system of electrodynamic macroscopic equations (18) together with the Maxwell equations (5) decouples from the Navier–Stokes hydrodynamic equations [10, 13] and may be solved independently. To obtain conditions for chemical or ionization (dissociation) equilibrium (beyond the diffusion boundary layer and in the hydrostatic approximation), Eq. (18) is rewritten for dimensionless variables:

$$E_* = U/L, \quad \sigma_* = \sigma_0, \quad b_* = (b_+ + b_-)/2,$$

$$n_* = \sigma_*/(2b_*Ze_0);$$

$$\tilde{\varphi} = \varphi/L, \quad \tilde{T} = T/T_*, \quad \tilde{\sigma} = \sigma/\sigma_*,$$

$$\tilde{b}_\pm = b_\pm/b_*, \quad \tilde{q} = q/(n_*Ze_0).$$

The new variables are defined using L, the characteristic dimension of the variation of variables U, applied electric voltage σ_*, conductivity of the self-neutralizing background that belongs to the type of conductivity of the quasi-neutral plasma [20] or an electrolyte [17] owing to dissociation (ionization) of fluid (gas), and T_* is the characteristic temperature. System of Eqs. (5) and (18) then has the form

$$\begin{cases} \tilde{q} = -\delta\tilde{\vec{E}}\tilde{\nabla}\tilde{\sigma}/\tilde{\sigma}, \quad \delta = \dfrac{2\varepsilon_r\varepsilon_0 b_* E_*}{\sigma_* L}; \\ \dfrac{\sigma^2}{4}\tilde{b}_+\tilde{b}_-\tilde{\vec{E}}\tilde{\nabla}\tilde{q} = \dfrac{\tilde{\Psi}\left(\tilde{\vec{E}}, \tilde{T}\right)}{\Psi(0, T_0)} - \tilde{\sigma}^2 + (\tilde{b}_+ - \tilde{b}_-)\tilde{q}\tilde{\sigma}; \\ \tilde{\vec{E}} = -\tilde{\nabla}\tilde{\varphi}. \end{cases} \tag{19}$$

[3] In problem [22] for the potential of jets heated to plasma temperatures, the mobility values may be the same or different. In the case of quasi-neutrality, it follows from (19) that the difference between the mobility values weakly affects the sought characteristics. The flow effect on the distribution of φ in electric filters is insignificant, and in heated jets it becomes a dominant effect for the case of low φ in the created plasma.

In (19), differentiation is performed with respect to the dimensionless coordinate (characteristic length L) and $\tilde{\Psi}(\left|\tilde{\vec{E}}\right|, \tilde{T}) = \Psi(E_* \left|\tilde{\vec{E}}\right|, T_* \tilde{T})$.

In the zeroth order in δ ($\delta \ll 1$), conductivity is a known function of the electric-field strength, which, in the same approximation, does not belong to the Laplace type. The volume charge appearing in the first approximation in δ affects the total value of $\vec{E}$. Its density q may be found in this approximation from the equations derived from (19). Expressed in dimensional variables, they have the form

$$\begin{cases} q = -\varepsilon_r \varepsilon \vec{E} \nabla\sigma/\sigma; \\ \sigma = \sigma_0 \dfrac{\Psi^{1/2}(\left|\vec{E}\right|, T)}{\Psi^{1/2}(0, T_0)}; \\ \vec{E} = -\nabla\varphi. \end{cases} \tag{20}$$

Additional conditions for dissociation (ionization) equilibrium in the case of a moving medium may be derived in a similar way. For a needle high-voltage electrode close to a pointlike one, owing to its small dimensions, one can search for solutions of (20) depending on spatial coordinate r alone; their variations with latitude and longitude can be neglected. In this problem, the difference between the values of $b_\pm$ yields (in contrast to problem [21]) the contribution to only the quadratic order of smallness in σ. If, for T = const, conductivity in weak fields σ_0 is only related to admixtures, the dimensionless criterion of similarity for the studied phenomenon δ increases when E increases. and in strong fields it becomes quite large. If $\delta \gg 1$, when the volume charge is created beyond the boundary layers not only owing to $\nabla\sigma$ but also to emission (injection) from a cathode, the solution of (19) can be sought in the form

$$\sigma = b_- q. \tag{21}$$

The latter inequality may be observed also when the medium's mobility increases—in particular, mobility increases as a result of phase transition from liquid to a dilute gas that complicates both the entire model (since creation of electrons should be taken into account) and the form of Ψ, for example, due to the onset of the impact collision of molecules by such free electrons accelerated by strong electric fields.) The same conclusions hold as well when σ does not increase if the absolute value of the field strength increases. Solutions of type (21) may be used, since diffusion is neglected only outside the vicinity of the boundary layer of a high-voltage electrode. In corona-discharge theory, such a unipolar charged zone is usually called the external zone of a discharge [7]. In the case of a positively charged electrode (which sometimes creates an optical corona), instead of (21), the following class of solutions should be sought for such a zone:

$$\sigma = b_+ q. \tag{22}$$

This solution also corresponds to the case $\delta \gg 1$. In this limit, the current on the boundary both in case (21) and (22) is related to carriers with only one sign of charge.

In the case of the emission boundary conditions for the current density

$$(j_- = j(r_0') = b_- qE \tag{23}$$

on the needle high-voltage cathode and $j_+ = j(d) = 0$ on the anode), a 1D solution of such system has been obtained, among others, in [21]. For this solution

$$E^2(r) = \frac{C}{r^4} + \frac{I}{6\pi\varepsilon_r\varepsilon_0 b_- r}. \tag{24}$$

In Eq. (24), I is the amperage of the current passing through the system of electrodes and a weakly conducting medium, which is assumed in this study, as well as the high voltage applied to the electrodes, to be time-independent (flows in a variable electric field are described, for example, in [6]). The integration constant C in the unipolar conductivity equations (24) is determined from work function $e_0\chi$ taking into account the effect of the electric field on the work function [18]:

$$I = 4\pi r^2 j, \quad \tilde{I} = \frac{I}{4\pi r_0'^2 A_T T_w^2}, \quad \chi = \frac{e_0}{8\pi\varepsilon_r\varepsilon_0 r_a};$$
$$C = r_0'^4 \left\{ \frac{16(k_B T)^4 (\pi\varepsilon_r\varepsilon_0)^2}{e_0^6} \right. \tag{25}$$
$$\left. \times \left(\frac{e_0\chi}{k_B T} - \frac{u_e}{k_B T_W} + \ln\tilde{I} \right) - \frac{\tilde{I}}{6\pi\varepsilon_r\varepsilon_0 b_-} \right\}.$$

It is reasonable to use a boundary condition that corresponds to the dominance of thermal emission (with respect to other ionization or injection surface processes) with subsequent adhesion of the electron to molecules in order to determine C near the cathode, heated at least to the temperature of a low-temperature plasma. It may also be used to study processes in the vicinity of a flame located in a strong electric field [18] provided that the composition of the media remains unchanged in this area (only in the area of partial burning). Solution (24) with integration constant C determined from empirical boundary conditions at room temperature was noted in many studies where only the media with unipolar conductivity were considered, as well as in electrodynamic problems not taking into account hydrodynamic effects.

In the considered approach where C is determined through formula (25), A_r is the universal Richardson–Deshman thermal-emission constant determined by quantum-mechanical methods, T_w is the temperature of the cathode prior to a field being applied, and r is a

characteristic radius of the electrode with a near-electrode diffusion boundary layer. In this study, it is assumed that the electric current flowing through a circuit of the type shown in Fig. 1 weakly changes the temperature of the heated cathode, in the vicinity of which thermal gravitational convection may appear in addition to the electric one. Earlier, the voltage of the "corona ignition" type and other sought for quantities were calculated via formulas that contain a constant r_0' variable within reasonable limits. In developing techniques for calculation of the required characteristics in this study, formulas have been developed that do not contain this constant. In the derivation of these formulas, it has been taken into account that the distance between electrodes satisfies the condition $d \gg r_0'$. Using this condition, one can obtain an expression for the applied voltage for media that is an integral of E determined via (24):

$$U \approx \sqrt{\frac{2Id}{3\pi\varepsilon_r\varepsilon_0 b_-}}. \qquad (26)$$

Applicability of this formula for a cold cathode has been justified in our previous study [24]. In the case of a cathode heated to plasma temperatures, the sufficient condition for applicability of formula (26) has been shown to have the form of inequality $\frac{C}{r^3} \ll 1$. We have derived this inequality from formulas (24) and (25) and the second mean-value theorem for Riemann integrals. In the case of ideal gases whose equation of state is described by (13a), formula (26) may be used to analyze the effect of pressure on prebreakdown current–voltage characteristics. The quadratic dependence of the current on voltage that follows from (26) has been qualitatively confirmed (Fig. 3) by the results of the experiments of [23], where the "corona" was observed in air near a high-voltage pin which is not always the case in the considered liquids and dense gases. It is for plotting the theoretical curve in Fig. 3 according to formula (26) that the equation of state (13a) was used and, in addition to (7a), one more Langevin result, according to which the product of density and mobility is constant. A quadratic current–voltage characteristic also follows from processed data on prebreakdown experiments with dielectric weakly conducting liquids [6]. This dependence can also be confirmed theoretically for the conditions of equilibrium volume isothermal dissociation (ionization) in the case of $\Psi(|\vec{E}|, T_0)/\Psi(0, T_0) = \Psi_0(|\vec{E}|)$, determined according to Frenkel [4] or according to [3] with an elementary charge that is a multiple of Z:

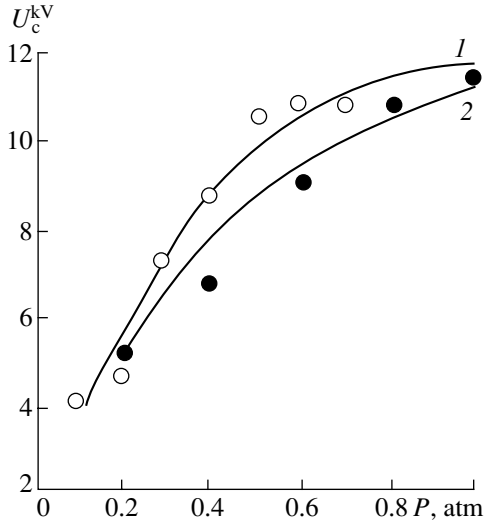

Fig. 3. Comparison of the theoretical dependence of the voltage of a "corona" discharge on the pressure of an ambient medium yielded by (26) with measured results [23]: (*1*) results of experiments [23] and (*2*) a theoretical curve corresponding to Eq. (26) and experimental conditions [23].

$$\beta(T) = \frac{(Ze_0)^{\frac{3}{2}}}{(\pi\varepsilon_r\varepsilon_0)^{\frac{1}{2}}k_BT};$$

$$\beta(T_0) = \beta_0; \qquad (27)$$

$$\Psi_0(|\vec{E}|) = \exp\left(\beta_0|\vec{E}|^{\frac{1}{2}}\right).$$

In this case, for the field in a vicinity of a high-voltage spherical or semispherical electrode whose radius is small (relative to the distance between electrodes) (see Fig. 1), the authors of earlier studies, for example, [16], have obtained an analytic solution (20):

$$|\vec{E}|\exp\left(\beta_0|\vec{E}|^{\frac{1}{2}}\right) = \frac{I}{4\pi\sigma_0 r^2};$$

$$\varphi_w = \varphi(r_0');$$

$$|\varphi_w| = U = \left|\int_{r_0}^{\infty} E dr\right| = \frac{1}{2}\left(\frac{I}{\pi\sigma_0}\right)^{\frac{1}{2}} \qquad (28)$$

$$\times\left(\frac{8}{\beta_0}\left[1 - \exp\left(\frac{\beta_0 E_0^{\frac{1}{2}}}{4}\right)\right] - E_0^{\frac{1}{2}}\exp\left(-\frac{\beta_0 E_0^{\frac{1}{2}}}{4}\right)\right).$$

As follows from (28), the difference between the absolute value of the strength of a self-consistent field

electric field and that of the applied field is small provided only that

$$\beta_0 E_0^{\frac{1}{2}} \ll 1, \tag{29}$$

i.e., in the case when the flows from high-voltage electrodes are not developed according to [6]. If I or U increases, current–voltage characteristic (29) becomes nonlinear, and if

$$\beta_0 E_0^{\frac{1}{2}} \gg 1 \tag{30}$$

the corresponding passage to the limit in (29) yields

$$U = \frac{4}{\beta_0}\left(\frac{I}{\pi\sigma_0}\right)^{\frac{1}{2}}. \tag{31}$$

The effect of r_0 on the current–voltage characteristic is small similar to the regimes of unipolar strongly nonequilibrium ionization (dissociation) for which this conclusion follows from (29).

The quadratic current–voltage characteristic remaining valid in the conditions when the hydrodynamic transport of charge under the electric wind in liquid weakly conducting media affects the spatial distribution of this charge has been experimentally found in [6] not only for unipolarly charged fluids. According to [6], the same empirical dependence is the most characteristic also for the velocities of developed flows. In the case of undeveloped flows, the empirical value of the exponent in the voltage dependence of the axial velocities of jets (see Fig. 1) is, according to [6], larger. This conclusion is obtained below in a theoretical way.

According to [6], for such flows $u(x, 0) \propto u^{\aleph}$, $\aleph = 3$. Theoretically, such a decrease in the exponent when U increases and the undeveloped flows of the electric wind become developed can be obtained for the conditions of equilibrium ionization (dissociation) for which the current–voltage characteristic is described by formulas similar to (29) and (31). In [16], for these conditions, an analogy was used (for the case of an active high-voltage needle and spherical electrodes (see Fig. 1) close to pointlike) between the electric wind and an axial-symmetric jet being discharged from a nozzle into a space filled with the same medium and not flowing around walls or other solid items like cylinders, ellipsoids, or cones when propagating in the medium. Ostroumov [7] was the first to propose such analogy; however, in the cases when the jet is an additional source of mass, this analogy, as has been shown in [6], is not applicable. It may be applied to the structure of a flow (for example, for Landau infinitely narrow jets [10]) characterized by the weak effect of the additional mass brought by the jet as compared to the mass of the medium; however, on the other hand, an electric-wind jet, which is not a source of mass, may be compared with infinitely narrow jets from a pointlike momentum source [10] only provided that the density of Coulomb forces rapidly falls when the distance from the high-voltage electrode (close to a point source) increases. In this case, calculation, according to [10], of vector constant P of the momentum of jets whose velocities are calculated under the assumption that the mass-source characteristics are close to zero, is reduced to calculation of the integral

$$\vec{p} = \int_V q\vec{E}dV = \vec{F}_e, \tag{32a}$$

where V is the volume of the semispace in the direction away from a needle or semispherical electrode (see Fig. 1). A mathematical proof of equality (32a) has been presented in earlier publications of the author of this study, although the statement itself has been made in works of other authors, for example, [12]. Since in spherical coordinates

$$dV \propto r^2 \sin(\theta) dr d\theta d\zeta,$$

this integral converges provided that

$$\left|q\vec{E}\right| < \frac{F}{r^{3+\aleph}}, \tag{32b}$$

where $\aleph > 0$, F is a constant majorant and r is the distance from the center of an electrode whose topology is close, owing to its small dimensions, to a pointlike (small spherical) electrode or the radial coordinate. Equilibrium solution (29) satisfies condition (32), whereas nonequilibrium solutions do not. Therefore, in [25], where unipolarly charged jets were considered in a strongly nonuniform electric field (see Fig. 1), the structure of the solution proved to be more complex than in [2], where the Landau–Shlichting solutions [11, 12] were used and momentum P was calculated using solutions (29). Note that in magnetic hydrodynamics (for example, in [12]) the analogy described above is also widely used; however, no criterion for the pointlike character of the Ampere force creating magnetic hydrodynamic jets similar to (32) has been derived. In limiting case (30a) for undeveloped flows, study [16] predicts $u \sim U^{\frac{5}{2}}$ in accordance with the results of Gibbins' experiments [19]. In limiting case (30b) for $r = \sqrt{x^2 + y^2} \gg r_0$ (see Fig. 1), the formulas for Shlichting jets [12] have the form

$$P = 2\pi\rho_0 \int_0^\infty u_x^2 y dy = \frac{\varepsilon_r \varepsilon_0 U^2}{8}; \tag{33a}$$

$$u_x = \frac{3p}{8\pi\rho_0 x(1+\xi^2/4)}, \quad u_y = \frac{\sqrt{3p}(\xi - \xi^3/4)}{2\sqrt{\pi\nu\rho_0}x(1+\xi^2/4)},$$
$$\xi = \frac{\sqrt{3p}}{2\sqrt{2\pi\rho_0\nu}x}. \tag{33b}$$

Quadratic dependence on U or linear on I follows then from (32a) for the axial velocity of developed jets. In addition, formulas (33) confirm the experimentally observed weak dependence of the velocities of prebreakdown flow on the curvature radius of a thin high-voltage electrode. Independence of the velocities of such flows from Z, which follows from (33), indicates that these formulas may be used to calculate the velocities without preliminary determination of this initial constant by calculations or experiments based on the composition of the medium's molecules (the medium's dielectric permittivity is assumed to be a reference constant similar to mobility and low-voltage conductivity). For prebreakdown jets with planar symmetry (planar jets from high-voltage blade-shaped electrodes), corresponding Shlichting formulas were also used earlier [2].

It should be noted that for Shlichting jets, structure (33b) is maintained also for turbulence regimes where the kinematic viscosity should be replaced by apparent turbulence viscosity. Momentum P of gas-dynamic (plasma) jets from jet engines (see Fig. 2) is then equal, according to (32a), to their thrust. Equation of state (13b) may often be used as well for heated media, in particular, for infinitely thin (weakly diverging) jets of such media. The estimates made in performing this study for the conditions of experiments [21] show that the density of gravitational force in momentum equation (9) may be neglected as compared to the inertia term in those equation. Formulas for the equilibrium distribution of absolute temperature T for constant thermal conductivity in such jets taking into account (33b) (as described, for example, in the monographs by Loitsyanskii, where submerged jets flowing around walls are also considered) may be derived from (14). If the axial distribution of the electric potential is given by (6) with the conditions along the axes of such jets close to (17) and if the relations

$$\left|\sigma\vec{E}\right| \ll \left|q\vec{u}\right|, \quad q = q(x), \quad \vec{j} = q\vec{u},$$
$$I = \int_s q\vec{u}d\vec{S} = 2\pi q\int_0^\infty u_x y dy \tag{33c}$$

are satisfied, we obtain a 1D Poisson equation using also the charge-conservation law presented in the integral form:

$$\int_S \vec{u}d\vec{S} = J = 0.04\sqrt{\frac{P}{\rho_0}}x;$$
$$qJ = I = S_c A_T \exp\left(\frac{U_e - e_0\chi}{k_B T_c}\right); \tag{34}$$
$$S_c = \pi(R_c + r_c)l_c, \quad \Delta\varphi = -\frac{I}{0.404\varepsilon_r\varepsilon_0\sqrt{\frac{P}{\rho_0}}x}.$$

The boundary conditions for this equation may be represented in standard form:

$$\varphi(S_c) = \varphi(0) = 0, \quad \varphi(d_m) = \varphi_0;$$
$$-h_c \le x \le d_m, \quad h_c = \sqrt{l_c^2 - (R_c - r_c)^2}. \tag{35}$$

In (35), r_c, R_c, and l_c are characteristic dimensions of the jet nozzle, and d is the maximum distance between a diffuser and a net-shaped electrode (see Fig. 2) on which the electric potential in the jet may be measured. We have not yet solved the problem whether the empirical boundary solution at a distance of d from a nozzle may be replaced by a stricter one (derived from theoretical consideration). However, in this study, unlike a number of earlier publications, the full electric current has been determined not empirically but from the known Richardson–Deshman formula for the current density (from a metallic nozzle). Unlike [26, 27], a modification of this formula (34) was used here. Because of this, it was possible to derive final formulas for calculating the spatial distribution of the sought for potential taking into account how the electron affinity energy of the molecules in the moving heated medium affects the spatial distribution of the electric field generated in this medium. We have not considered this effect previously. For current I that follows from (33), solution (34) with boundary conditions (35) for the spatial distribution of the potential may be represented in the 1D approximation in the following form (flow rate J in (34) is found via the Shlichting formula for the case of a strong (turbulent) jet whose derivation may be found, for example, in [28]):

$$\varphi(x) = \frac{\varphi_0 x}{d_m} - \frac{I_x \ln(x/d_m)}{0.404\sqrt{\frac{P}{\rho_0}}\varepsilon_r\varepsilon_0}. \tag{36}$$

In contrast to the solutions of macroscopic equations (16) derived in [21], which have been obtained earlier, distribution (36) enables calculation of the maximum in the spatial distribution of the potential observed in experiments [21]. The maximum that follows from (36) is located (close to the experimental value) at a distance of $\frac{d_m}{\exp\left(1 - \frac{1}{\tilde{I}}\right)}$ from the source, which is also close to the empirical value [21], where

$$\tilde{I} = \frac{Id_m}{0.404\varphi_0\varepsilon_r\varepsilon_0\sqrt{\frac{P}{\rho_0}}}. \tag{37}$$

It should be noted that in experiments [21] the mass brought by a jet weakly affected the mass that was entrained in motion by that jet owing to small dimensions of a nozzle as compared to the volume of considered medium (see Fig. 2). Therefore, the theoretical solutions for the equations of motion of viscous media

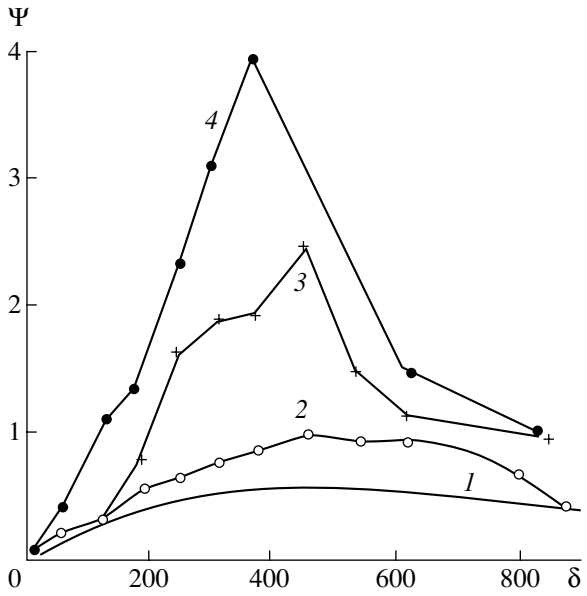

Fig. 4. Distribution of the electric-field potential in a jet (along the jet axis) $\delta = x/d_m$, $\tilde{\varphi} = \varphi/\varphi_m$: (*1*) theoretical solution [36]; (*2*) an experiment with a net-shaped electrode; (*3*) an experiment wit a metallic electrode; and (*4*) an experiment with a liquid electrode (water).

[10, 12] obtained analytically, as was indicated in [28] in an approximation of an infinitely narrow jet are applied in this study for description of both electric convective and thermally ionized jets. A plot of spatial distribution (36) where I was calculated via our modification of the Richardson–Deshman formula (34) is presented in Fig. 4 as theoretical curve *1* calculated for the conditions of experiments [21] with a net-shaped electrode. The jet temperature near a nozzle was 2370 K (to ensure such a value of T, a nitroglycerin ballistic fuel was used), and the exhaust velocity was 1380 m/s indicating that the formulas for turbulence jet may be used to calculate the sought potential. The critical radius of the nozzle's truncated cone was 2.2 mm, the generatrix of that cone was 75 mm, and the nozzle height was 50 mm. The jet thrust was 230 N and the maximum distance from the nozzle at which the electric potential was measured along the jet axis was 2 m. Since the dielectric permittivity of air at room temperature is 1.1, i.e., close to r_1, the same value was assumed for the heated air jet. According to reference data, the work function for extraction of electrons from a steel nozzle was taken to be equal to 4.36 eV and the energy of affinity of the oxygen molecules in air to electrons to −1.8 eV. It is noteworthy that a simple comparative analysis of the work functions, ionization potentials, and electron affinity energies is presented, for example, in [20] (according to [17], in the dissociation case, the exchange current and the electrochemical potential near an electrode surface are analogs of the emission current and the work function for the electrode surface). However, the exchange currents and electrochemical potentials have been studied for weakly dissociating media in [17] and other monographs devoted to electrochemistry in a significantly less comprehensive way than strong electrolytes. When calculating the distributions of electric potential in heated jets according to formulas (36) and comparing them to experimental data, we have improved the agreement between these calculated data and results of experiments [21] relative to a comparison of the results presented in earlier publications with the results of those experiment presented, for example, in [26, 27] (in the calculations of [26, 27], the effect was neglected of the affinity energy of the oxygen molecules in an air jet to the electrons emitted from a metallic nozzle on the sought for distribution of the electric potential in the jet.) In this study, similar to earlier ones, only experiments with a net have been theoretically analyzed (see Figs. 2 and 4). To analyze experiments with continuous metallic or liquid electrodes, 2D and 3D electrodynamic problems have to be solved. The theoretical results described above seem to be applicable in practice both for facilities that have been commercially used in industry (such as electric filters or oil electric dehydrators) and in aircraft engineering (jet engines), as well as for the development of new electric hydrodynamic devices, such as electric hydrodynamic pumps [29] or generators [30]. In the devices of former type, calculations of volume charges, electric fields, and current–voltage characteristics based on the techniques proposed in this study as a synthesis of methods [31] and [32] may yield more accurate results for the electric power and energy consumed. In addition, these techniques may be used to prevent electric breakdowns in such devices.

For the electric hydrodynamic pumps and generators that are currently being implemented in industry, the pressures, flow rates, and power values needed for their design may be calculated using the analytical formulas for electric fields, pressures, and flow velocities due to fields of narrow high-voltage electrodes proposed in this study. A description of a design for an electric hydrodynamic pump as well as the technique for calculation of the pump's pressure and flow rate is presented, for example, in our study [29] where it was shown that high-voltage blade-shaped electrodes should be used rather than needle electrodes proposed in [30]. Similarly, for the case of thermally ionized flows, it was shown in [27] that the comparison of the maxima of the calculated potential for planar and axially symmetric jets yields the planar jets that are preferable for electric hydrodynamic generators.

REFERENCES

1. Apfelbaum, M.S. and Yantkovskii, E.I., Volume Charge and Ponderomotive Forces in Immobile Weakly Conducting Liquid Dielectric with Spherical and Plane Electrodes, *Elektrokhimiya*, 1984, vol. 20, no. 7, pp. 872–878.

2. Yantkovskii, E.I. and Apfelbaum, M.S., On the Pump Effect of a Narrow High-Voltage Electrode in a Weakly Conducting Dielectric Liquid, *Zh. Tekh. Fiz.*, 1980, vol. 50, no. 7, pp. 1511–1520.

3. Plumley, H.J., Conduction of Electricity by Dielectric Liquids at High Field Strength, *Phys. Rev.*, 1941, vol. 50, no. 2, pp. 200–207.

4. Petrichenko, N.A., Thermal Effects Accompanying Electric Wind in Liquids, *Elektr. Obrab. Mater.*, 1973, no. 6, pp. 44–45.

5. Lyubimov, G.A., On the Conditions for Breakdown of a Near-Electrode Layer in a Flow of Ionized Gas, *Prikl. Matem. Tekh. Fiz.*, 1973, no. 3, pp. 16–23.

6. Stishkov, Yu.K. and Ostapenko, A.A., *Elektrogidrodinamicheskie techeniya v zhidkostyakh* (Electric Hydrodynamic Flows in Liquids), Leningrad, 1989.

7. Bologa, M.K., Grosu, F.P., and Kozhuhar', I.A., *Elektrokonvektsiya i teploobmen* (Electric Convection and Heat Exchange), Chisinau, 1977.

8. Gogosov, V.V., Polyanskii, V.A., Semenova, I.P., and Yakubenko, A.A., Equations of Electric Hydrodynamics and Transfer Factors in a Strong Electric Field, *Mekh. Zhidk. Gaza*, 1959, no. 2, pp. 31–45.

9. Onsager, L., Deviation from Ohm's Law in Weak Electrolytes, *Jour. Chem. Phys.*, vol. 2, no. 9, pp. 599–615.

10. Landau, L.D. and Lifshitz, E.M., Mekhanika sploshnykh sred (Mechanics of Continuous Media), Moscow, 1954.

11. Landau, L.D. and Lifshitz, E.M., Elektrodinamika sploshnykh sred (Electrodynamics of Continuous Media), Moscow, 1957.

12. Boyarevich, V.V., Freiberg, Ya.Zh., Shilova, E.I., and Shcherbinin, E.Ye., *Elektrovikhrevye techeniya* (Electric Vortex Flows), Riga, 1985.

13. Sedov, L.I., *Mekhanika sploshnoi sredy* (Mechanics of Continuous Media), Moscow, 1994, vol. 1

14. Frenkel', Ya.I., On the Theory of Electric Breakdown in Dielectrics and Electronic Semiconductors, *Zh. Eksp. Teor. Fiz.*, 1938, no. 12, pp. 1293–1301.

15. Levich, V.G., Vdovin, Yu.A., and Myamlin, V.A., *Kurs teoreticheskoi fiziki* (Course of Theoretical Physics), Moscow, 1971, vol. 2.

16. Apfelbaum, M.S. and Apfelbaum, E.M., One Model of Conduction and Electric Field Distributions in a Liquid Insulator, *J. Electrostatics*, 2001, vol. 50, pp. 131–142.

17. Damaskin, B.B. and Petrii, O.A., *Vvedenie v elektrokhimicheskuyu kinetiku* (Introduction to Electrochemical Kinetics), Moscow, 1975.

18. Lowton, J. and Weinber, F., *Elektricheskie aspekty goreniya* (Electrical Aspects of Combustion), Moscow, 1976.

19. Gibbings, J.C. and Mackey, A.M., Charge Convection in Electrically Stressed Low-Conductivity Liquids. Part 3: Sharp Electrodes, *J. Electrostatics*, 1981, vol. 11, pp. 119–134.

20. Khrapak, A.G., Fortov, V.E., and Yakubov, I.T., *Fizika neideal'noi plazmy* (Physics of Nonideal Plasma), Moscow, 2004.

21. Usachov, V.K., Stavrov, Yu.P., and Tambovtsev, V.I., An Electric Kinetic Phenomenon in a Jet of Ionized Combustion Products, *Tezisy dokl. nauch.-praktich. seminara po elektrofizike goreniya* (Abstr. Scient. Pract. Seminal on Electrical Physics of Combustion), Karaganda, 1985, pp. 66–67.

22. Apfelbaum, M.S., The Space Electric Field Distribution in Thermoionization Strong Jets, Proc. 3rd Workshop on Magnetoplasma Aerodynamics in Aerospace Applications, Moscow, 2001, pp. 317–318.

23. Usachov, V.K., Studies of the Characteristics of Corona Discharge from a Pin under Underpressure Conditions, in: *Avtomatizatsiya energosistem i energoustanovok promyshlennykh predpriyatii* (Automation of Energy Systems and Energy Facilities of Industrial Enterprises), Chelyabinsk: Chelyabinsk Polytechnic Institute, 1981, pp. 127–129.

24. Apfelbaum, M.S., Equations of Ionization for Corona Discharge of Weakly Conducting Gases, *Elektr. Obrab. Mater.*, 1996, nos. 4–6, pp. 38–44.

25. Zhakin, A.I., On Electric Convective Jets in Liquid Dielectrics, *Mekh. Zhid. Gaza*, 1964, pp. 13–19.

26. Apfelbaum, M.S., Spatial Distribution of the Electric Field in Thermal Ionized Jets, *Elektr. Obrab. Mater.*, 2005, no. 1, pp. 50–53.

27. Apfelbaum, M.S., The Space Electric Field Distribution in the Thermoionization Jets, *Proc. 15th Int. Conf. MHD Energy Conversion and 6th Int. Workshop on Magnetoplasma Aerodynamics*, Moscow, 2005, vol. 1, pp. 196–197.

28. Loitsyanskii, L.G., *Mekhanika zhidkosti i gaza* (Fluid Mechanics), Moscow, 1978.

29. Apfelbaum, M.S., A Technique for Calculation of the Characteristics of Electric Hydrodynamic Flows and Pumps, *Elektr. Obrab. Mater.*, 1990, no. 6, pp. 39–42.

30. Bortnikov, Yu.S. and Rubashov, I.B., Electric Gas Dynamical Effects and Their Application, *Magn. Gidrodin.*, 1975, no. 1, pp. 23–34.

31. Ostroumov, G.A., *Vzaimodeistvie elektricheskikh i gidrodinamicheskikh polei* (Interaction of Electric and Hydrodynamic Forces), Moscow, 1979.

32. Tikhodeev, N.N., Differential equation for Unipolar Corona and Its Integration in the Simple Cases, *Zh. Tekh. Fiz.*, 1955, vol. 24, no. 8, pp. 1449–1457.

ISSN 1068-3755, Surface Engineering and Applied Electrochemistry, 2007, Vol. 43, No. 1, pp. 36–39. © Allerton Press, Inc., 2007.
Original Russian Text © F.P. Grosu, M.K. Bologa, 2007, published in Elektronnaya Obrabotka Materialov, 2007, Vol. 43, No. 1, pp. 47–51.

ELECTRICAL PROCESSES IN ENGINEERING AND CHEMISTRY

On Bipolar Space-Charge Structures in Low Conductive Liquids in an External Electrostatic Field

F. P. Grosu[a] and M. K. Bologa[b]

[a] *State Agrarian University of Moldova, ul. Mircheshť 44, Chisinau, MD-2049, Republic of Moldova*

[b] *Institute of Applied Physics, Academy of Sciences of Moldova, ul. Academiei 5, Chisinau, MD-2028, Republic of Moldova*

Received September 18, 2006

Abstract—The general set of equations for the case of electrostatic field in a low conductive liquid in the interelectrode gap of a plane-parallel capacitor is formulated. The basic equation for the distribution of the electric field strength is obtained, and similarity criteria for the processes of current transport and charge formation are found. The conditions that define the form of the field distribution are established by analysis of signs of the first and second derivatives of the electric field strength. In particular, it is shown that formation of bipolar structures is impossible in the case of "pure" polarization when current equals zero. Alternatively, their formation is linked with the passage of a sufficiently strong current. Ways to solve the basic equation are developed. The approximate solution for the general case of the problem is given.

DOI: 10.3103/S106837550701005X

1. INTRODUCTION

Processes of space-charge generation in low conductive liquid dielectrics in electrostatic fields are still the focus of attention of researchers investigating electrophysics and electrohydrodynamics (EHD) of liquids, judging by the programs of various international forums and conferences on the topic [1].

This is understandable, since the problems of charge formation have not been clearly explained as yet, and this hinders more adequate developments in the fields of research noted above. The following known types of space distributions of electric potential between the plates in a plane-parallel capacitor filled with a liquid under investigation have been considered as standard cases (see figure): a heterocharge (curve *1*), a homocharge (curve *2*), and monopolar distributions (curves *3*, *4*). However, during the past few decades, a fine structure a few tenths of a millimeter in thickness of the near-electrode charged layers in a liquid was found [2, 3] that considerably modified the classical distributions (curves *1*(*4*)). It was found that for small (initial) voltages across the test cell, the $\varphi(x)$ distribution corresponds to the heterocharge type (curve 1). When the electrode potential difference increases over some critical value $U \geq U_{CR}$, the sublayer adjoining the electrode surface gains the charge of the same sign as the electrode holds (a homocharge), whose density passing through the zero point ($\rho = 0$) reverses the sign to its initial (opposite) type. Peaks appear in the $E(x)$ distribution of the field strength in the near-electrode layers (curve *5*). This means that space-charge bipolar structures in the near-electrode boundary layers have been formed. Detection of the bipolar structures is of principal importance, since it provides a new approach to the theory and description of numerous secondary electrohydrodynamic phenomena. Nevertheless, the very fact of the existence of such structures is sometimes considered questionable because the probe method that permits detection of the bipolar field distributions is not applicable so close to the electrode surface region.

However, further investigations, including theoretical studies, have confirmed the reliability of the obtained results [4]. The authors of [2, 3] themselves have quite logically explained the formation of homocharges at the electrode surface, when the critical field strength ($E > E_{CR}$) is reached. Namely, the charge injection processes from the electrode prevail over the charge migration transfer from the interior of the liquid to the electrode [3]. We have also put forward an idea

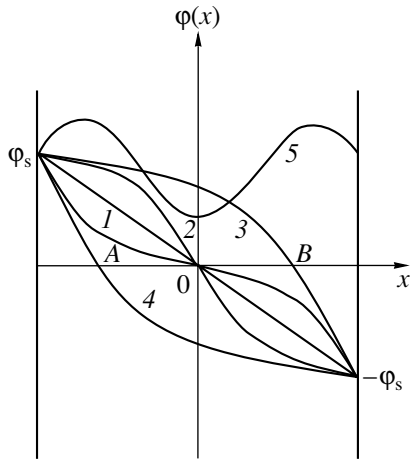

Potential distributions in a plane-parallel capacitor.

[5] that, when the liquid gains a heterocharge, the near-electrode field strength increases to a magnitude high enough to produce an electric "microbeakdown" in the surface liquid layer, which leads to a dramatic drop in the initial "breakdown" field strength. Hence, a layer appears with higher electrical conduction and lower field strength. The physical meaning of the explanations is the same, but the main problem is to develop a mathematical model for the discussed phenomena. In [5] an attempt was undertaken to propose such a model based on a microbreakdown idea, which is still far from complete. The objective of the paper is to clarify the possibility of the existence of bipolar structures in the framework of the classical Nernst–Plank and Maxwell equations. If this possibility is confirmed, the next step of our investigation will be to solve the problem in its final form.

2. GENERAL SET OF EQUATIONS: BASIC EQUATION AND SIMILARITY CRITERIA

Since experimentally bipolar structures may be detected by introducing impurities in the liquid under investigation, the system is multicomponent and partial current densities are expressed as the sums

$$\begin{cases} j_+ = E\sum\limits_{i=1}^{m} k_{+i}\rho_{+i} - \sum\limits_{i=1}^{m} D_{+i}\rho'_{+i}, \\ j_- = E\sum\limits_{i=1}^{n} k_{-i}\rho_{-i} + \sum\limits_{i=1}^{n} D_{-i}\rho_{-i}, \end{cases} \tag{1}$$

where m, n is the number of components, respectively. Introducing the averaged coefficients for mobilities $\bar{k}_\pm \equiv \bar{k}_\pm$ and diffusion $\overline{D}_\pm \equiv \mathrm{D}_\pm$

$$K_+ \equiv \left(\sum_{i=1}^{m} k_{+i}\rho_{+i}\right)/\rho_+; \quad k_- \equiv \left(\sum_{i=1}^{n} k_{-i}\rho_{-i}\right)/\rho_-;$$

$$D_+ \equiv \left(\sum_{i+1}^{m} D_{+i}\rho_{+i}\right)/\rho_+; \quad D_- \equiv \left(\sum_{i=1}^{n} D_{-i}\rho_{-i}\right)/\rho_-; \tag{2}$$

$$\rho_+ \equiv \sum_{i=1}^{m}\rho_{+i}; \quad \rho_- \equiv \sum_{i=1}^{n}\rho_{-i}; \quad k_{\pm i}, D_{\pm i} = \text{const},$$

we obtain the case of a two-component system:

$$j_\pm = k_\pm\rho_\pm E \mp D_\pm\rho'_\pm, \tag{3}$$

where prime means the derivative with respect to x. It is worth noting that averaging of Eq. (2), strictly speaking, do not provide a constant over the volume coefficients $k_\pm$, $D_\pm$ because of $\rho_\pm(x)$ dependences, but due to the linear-fractional character of dependences $k_\pm$, $D_\pm$ on $\rho_{\pm i}(x) > 0$, they are weak functions of the coordinates. So, we assume them to be constant. Furthermore, we also assume $k_+ = k_- \equiv k$ and $D_+ = D_- \equiv D$; the asymmetry is taken into account via the inequality in the rates of chemical reactions at the electrodes, which leads to the inequality $j_+ \neq j_-$ (see below).

The only significant assumption adopted is the fulfillment of the conservation law of densities of partial currents: $\operatorname{div}\vec{j}_\pm = \vec{j}'_\pm = 0 \Rightarrow j_+, j_- = \text{const}$. However, this assumption does not seem very restrictive because it has been approved in electrochemistry [6], where charge carrie concentrations are much greater than for the case of dielectric liquids.

Taking into account all the above and performing addition and subtraction in (3) we obtain a set of differential equations closed with respect to E, ρ, σ, φ with the appropriate initial conditions:

$$\begin{gathered} \rho' = \frac{\sigma}{D}E - \frac{j}{D}; \ \rho(x)|_{x=l} = \rho_0, \\ E' = \frac{\rho}{\varepsilon}; \quad E(x)|_{x=l} = E_0, \\ \sigma' = \frac{k^2}{D}\rho E - \frac{k\delta}{D}; \quad \sigma(x)|_{x=l} = \sigma_0, \\ \varphi' = -E; \quad \varphi(x)|_{x=0} = U; \quad \varphi(x)|_{x=l} = 0, \end{gathered} \tag{4}$$

where the space charge density ρ, specific conductivity σ, the sum j and difference δ of charge densities are given by the formulas

$$\begin{gathered} \rho = \rho_+ - \rho_-; \quad \sigma = k(\rho_+ + \rho_-); \quad j = j_+ + j_-; \\ \delta \equiv j_+ - j_-, \end{gathered} \tag{5}$$

here $\sigma > 0$; $j \geq 0$, $\rho \geq 0$, $\delta \geq 0$ or $\rho < 0$, $\delta < 0$. The coordinate origin coincides with the left capacitor plate, and the right one is grounded. The plate spacing is denoted as l.

Substituting the second equation from set (4) into the third one and integrating we obtain

$$\sigma = \sigma_0 + \frac{\varepsilon k^2}{2D}(E^2 - E_0^2) + \frac{k\delta}{D}(l - x). \tag{6}$$

In the dependence, σ_0 is the function of the field strength E_0, but σ is also meaningful with no field applied (a low-voltage conductivity denoted as σ_*). Then, assuming in (6) $\sigma = \sigma_*$, $E = 0$, $\delta = 0 (j_\pm = 0)$ we obtain

$$\sigma_0 = \sigma_* + \frac{\varepsilon k^2 E_0^2}{2D} \Rightarrow \sigma = \sigma_* + \frac{\varepsilon k^2}{2D}E^2 + \frac{k\delta}{D}(l - x). \tag{7}$$

Substituting (7) into the first equation in (4) gives the basic equation for the charge formation process:

$$\rho' = \varepsilon E'' = \frac{\varepsilon k^2}{2D^2}E^3 + \frac{1}{D}\left(\sigma_* + \frac{k\delta}{D}(l - x)\right)E - \frac{j}{D}. \tag{8}$$

This is the Painleve equation [7]; we reduce it to dimensionless form. Introducing the dimensionless field strength $E = E_0\eta(\xi)$ and coordinate $x = l\xi$ we obtain

$$\eta'' = \pi_0\eta^3 + \pi_1(1 + \pi_2(1 - \xi))\eta - \pi_3, \quad (9)$$

where the following notations for dimensionless similarity complexes are used:

$$\pi_0 \equiv \left(\frac{lkE_0}{\sqrt{2}D}\right)^2;\ \pi_1 \equiv \frac{l^2}{\tau_* D};\ \pi_2 \equiv \frac{lk\delta}{\sigma_* D};\ \pi_3 \equiv \frac{jl^3}{\varepsilon D E_0}, \quad (10)$$

here $\tau_* \equiv \varepsilon/\sigma_*$ is the time of electrical relaxation. It should be noted that introducing the dimensionless potential $\varphi = U\chi$, χ into the last equation in set (4) we obtain

$$\chi'(\xi) = -\pi_4\eta, \quad \pi_4 \equiv \frac{E_0 l}{U}, \quad (11)$$

that is, one more similarity complex π_4 appears containing the voltage U.

The following initial conditions provide the single-valued solution of Eq. (9):

$$\eta(1) = \eta_0 = 1; \quad \eta'(1) = \eta'_0 = 0, \quad (12)$$

where the initial (for $x = l$) charge density ρ_0 is taken equal to zero, which occurs at least in the case of a symmetrical field distribution (figure, curve *1*).

Taking into account (9) and (12), we conclude that solutions for any problem in the process under discussion are also, except for the independent variable ξ, functions of four similarity parameters (10):

$$\eta = \eta(\xi, \pi_0, \pi_1, \pi_2, \pi_3). \quad (13)$$

It follows that the solutions are identical in various processes (problems) for the same values of parameters π_i ($\pi'_i = \pi''_i$); therefore, the π_i complexes are the similarity criteria in the processes being discussed. Furthermore, note that introducing these parameters, we have reduced the dependence of the field strength on eight dimensional parameters j, E_0, ε, K, σ_*, D, δ, l to its dependence on only four parameters, according to the π-theorem requirements. Designing experiments, as well as practical application of the results, becomes more evident on the basis of analogous parameters.

3. ON BIPOLAR STRUCTURES

Consider a basic equation that allows to assess the possibility of the existence of solutions describing the structures under discussion from the point of view of their specific features, namely, the roots of equations $\rho(x) \sim E'(x) = 0$ and $\rho'(x) \sim E''(x) = 0$. Consider several individual particular cases.

3.1. The stage of initial polarization, no current in the circuit ($\pi_2 = 0$, $\pi_3 = 0$)

Equation (9) takes the form

$$\eta'' = \pi_0\eta^3 + \pi_1\eta. \quad (14)$$

Since $\eta > 0$, $\eta'' > 0$, which is the distribution is concave everywhere; this corresponds to the heterocharge field distribution according the general physical concept above. The distribution of curve *5* (see figure) also gives evidence that no bipolar structures may be formed in this case. For this case, the exact solution of Eq. (14) may be obtained using the elliptical integral of the first kind $F(\varphi, k)$; its solutions $\eta(\xi)$ are given in subsequent sections of the paper.

3.2. The stage of current transport in symmetrical conditions ($\pi_2 = 0$, ($j_+ = j_-$), $\pi_3 \neq 0$)

Equation (9) takes the form

$$\eta'' = \pi_0\eta^3 + \pi_1\eta - \pi_3. \quad (15)$$

The right-hand side of (15) has the only positive root that divides the $\eta(\xi)$ plot into a convex part $\eta''(\xi) < 0$ and a concave part $\eta''(\xi) > 0$. The point $\eta''(\xi) \sim \rho'(x) = 0$ is the position of the extremum for the charge density curve. One of the necessary conditions for existence of the sought-for structure is fulfilled, so we may continue the search. For this we find the derivative η' (the dimensionless charge density) from (15):

$$\eta'' = \frac{d\eta'}{d\xi} = \frac{d\eta'}{d\eta}\frac{d\eta}{d\xi} = \frac{1}{2}\frac{d\eta'^2}{d\eta} = \pi_0\eta^3 + \pi_1\eta - \pi_3.$$

Integrating the equation, taking into account initial conditions (12), we obtain

$$\eta'^2 = \frac{\pi_0}{2}\left[(\eta^2 + a^2)(\eta + 1) - \frac{4\pi_3}{\pi_0}\right](\eta - 1), \qquad a^2 = 1 + \frac{2\pi_1}{\pi_0}. \quad (16)$$

The right-hand side, except for the known root $\eta = 1$ from the initial conditions obviously has one more positive root that also divides the domain of definition of the function into a positive part ($\rho > 0$) and a negative part ($\rho < 0$).

Hence, the existence of the root (although for the field strength only) $\eta' \sim \rho = 0$ suggests that bipolar structures are admissible even in the symmetrical case.

3.3. The general case ($\pi_2 \neq 0$; $\pi_3 \neq 0$)

This is the most interesting case because a much larger set of possible variants exists for the sign of the second derivative η'' than in the previous cases, or this sign also explicitly depends on the ξ coordinate; here the sign of the η coefficient in (9) for $\pi_2 < 0$ is determined by the ξ coordinate value. Furthermore, not only near-electrode strength maxima may exist, but minima as well. The exact solution of the problem leads to the transcendental Painleve functions [7], but here we provide only the approximate solution obtained by the simple Taylor series expansion:

$$\eta(\xi) = 1 + \frac{1}{2}A(1-\xi)^2 + \frac{1}{6}B(1-\xi)^3 + \frac{1}{24}C(1-\xi)^4, \quad (17)$$

where

$$A \equiv \pi_0 + \pi_1 - \pi_3; \quad B \equiv \pi_1\pi_2; \quad C \equiv (3\pi_0 + \pi_1)(\pi_0 + \pi_1 - \pi_3). \quad (18)$$

Any sign combination is admissible for all coefficients in dependence (17); therefore, we are able to state with certainty that at least qualitatively it may describe space-charge structures observed in practice.

A quantitative analysis of the discussed regularities is envisaged as the next stage of our investigations. Note, by the way, that the exact solution of the problem under study in the final form is also possible. It is expressed via elliptical integrals and will be also included.

REFERENCES

1. *Sovremennye problemy elektrofiziki i elektrodinamiki zhidkostei*, *Sbornik dokladov VIII Mezhdunarodnoi Nauchnoi Konferentsii* (Actual Problems of Electrophysics and Electrodynamics of Liquids, Proc. VIII Int. Conf.), 2006, St. Peterburg: St. Peterb. Gos. Univ.
2. Rychkov, Yu.M. and Stishkov, Yu.K., Electric Field Strength and Space Charge in Industrial Liquid Dielectrics, *Kolloidn. Zh.*, 1978, no. 6.
3. Stishkov, Yu.K. and Ostapenko, A.A., *Elektrogidrodinamicheskie techeniya v zhidkikh dielektrikakh* (Electrohydrodynamic Flows in Liquid Dielectrics), Leningrad: Izd. Leningr. Gos. Univ., 1989.
4. Apfel'baum, M.S. and Polyanskii, V.A., On the Space Charge Formation in Low Conductive Media, *Magn. Gidrod.*, 1982, no. 1.
5. Grosu, F.P. and Bologa, M.K., Peculiarities of Electrization of Low Conductive Dielectric Liquid in an External Electrostatic Field, *Elektr. Obrab. Mater.*, 2006, no. 4, pp. 37–45.
6. Ostroumov, G.A., *Vzaimodeistvie elektricheskikh i gidrodinamicheskikh polei* (Interaction of Electric and Hydrodynamic Fields), Moscow: Nauka, 1979.
7. Kamke, E., *Spravochnik po obyknovennym differentsial'nym uravneniyam* (Handbook on Ordinary Differential Equations), Moscow: Nauka, 1971.

ISSN 1068-3755, Surface Engineering and Applied Electrochemistry, 2007, Vol. 43, No. 1, pp. 40–43. © Allerton Press, Inc., 2007.
Original Russian Text © P.S. Orlov, 2007, published in Elektronnaya Obrabotka Materialov, 2007, Vol. 43, No. 1, pp. 52–56.

ELECTRICAL PROCESSES IN ENGINEERING AND CHEMISTRY

The Effect of Electromagnetic Fields on Hydrogen-Atom Transport in Steel

P. S. Orlov

FGOU VPO Yaroslavl State Agricultural Academy, Tutaevskoe sh. 58, Yaroslavl, 150042 Russia

Received October 30, 2006

Abstract—This article describes a model of hydrogen diffusion processes, shows the influence of protective cathode stations on the hydrogen saturation of underground-pipeline metal, and suggests a new method to find hydrogen-saturated sections in underground steel gas-supply systems.

DOI: 10.3103/S1068375507010061

The modern theory of the diffusion-transport mechanism of an interstitial metalloid in steel cannot explain how interstitial atoms pass from the environment into the iron crystal lattice, the strength of which exceeds that of steel by 2–3 orders of magnitude. The cause of this problem consists in the fact that the existing models of this process do not fully take into account the structure of real metals consisting of separate crystallites differing from each other in sizes and differently oriented in space. In turn, each crystallite involves fragments consisting of blocks. As a result, there are intercrystalline, interfragment, and interblock spaces in metal with volumes, which are 4–8 orders of magnitude less than those of the crystallites surrounding them. The boundaries between individual grains (crystallites) in metal are large-angle, reaching tens of degrees, and those between subgrains (fragments and blocks) are small-angle, equaling less than one angular degree. Because the input cross sections into microvolumes are commensurable with crystal-lattice parameters, the intercrystalline, interblock, and interfragment cavities are under deep vacuum conditions.

We proposed that the physical model of hydrogen penetration in steel [1], according to which hydrogen atoms are literally driven by atmospheric pressure into the interelement spaces of the metal structure because of the presence of concentration and pressure gradients in the gas phase on the metal surface and in the intercrystalline volumes. Under the action of external pressure, hydrogen atoms rush into interelement cavities with a deep vacuum until an identical gas-phase concentration in all accessible volumes is achieved and collide with the walls of interelement spaces. The relation between the force F acting on an arbitrary colliding body and its momentum is described by the Newton's second law:

$$F = m(dV/dt), \quad (1)$$

where dV is the velocity variation for an atom of mass m in time dt.

The forces F_W acting on cavity walls depend only on load conditions and equal

$$F_W = F/[2\sin(\alpha/2)]. \quad (2)$$

Because all the subgrain boundaries are small-angle, $\sin\alpha \approx \alpha$ for all angles $\alpha \longrightarrow 0$, and the forces F_W acting on cavity walls for an arbitrary normal external pressure P achieve considerable magnitudes, and the pressures P_W acting on walls can exceed the ultimate strength σ_U in arbitrary metals (Fig. 1):

$$P_W = (P_N/\alpha) \geq \sigma_U. \quad (3)$$

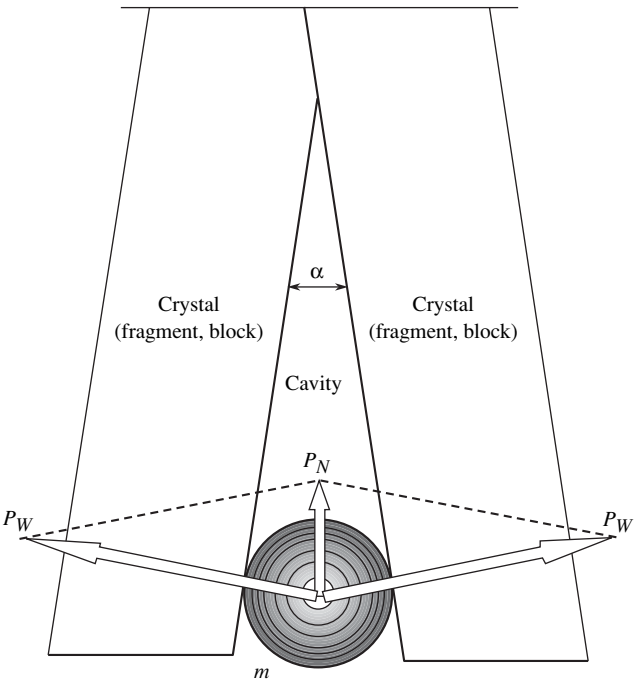

Fig. 1. Mechanism of the penetration of an interstitial atom with a mass m in intercrystalline, interfragment, and interblock volumes (cavities) in steel.

When cavity volumes increase as a result of the action of external stretching loads, hydrogen atoms near microvolume vertices move somewhat forward, and new portions of these hydrogen atoms penetrate in microvolumes. When a technological load is removed from the construction, interblock spaces decrease in size according to Hooke's law, and pressures on the cavity walls increase. Multiple cyclically alternating loads lead to the hydrogen saturation of the metal and to failure of the construction. The sum of weak interactions and the loading conditions imposed on alternating external loads, facilitates the penetration of hydrogen into steel. The proposed mechanism of hydrogen transport in steel is valid for other gases and carbon.

According to the modern model of diffusion process for the one-dimensional transport of a particle flux [2], interstitial atoms are displaced in metal under the action of concentration gradients $\partial c/\partial x$ describing the diffusion process itself or the mass transfer proceeding according to Fick's first law and also due to the potential gradient $\partial\varphi/\partial x$ (electrical transport) and the temperature gradient $\partial T/\partial x$ (heat transfer or energy transfer). But the existing model does not describe the transport of an interstitial metalloid from the environment into a metal under the action of the pressure gradient $\partial P/\partial x$, which describes the baric transport (momentum transport). The potential to remove hydrogen from steel under the action of electromagnetic fields is also ignored.

The author proposes an improved mathematical model [3] of the interstitial-atom transport in the metal and, further, in the crystal lattice, taking the pressure gradient into account, as well as the possibility for the evacuation of hydrogen from steel under the action of an external variable magnetic field:

$$\frac{\partial m}{\partial t} = -D\left(\frac{\partial c}{\partial x} + A\frac{\partial P}{\partial x} + B\frac{\partial T}{\partial x} + C\frac{\partial \varphi}{\partial x} + C\frac{\partial^2 \Phi}{\partial x \partial t}\right)SM, \quad (4)$$

where $\partial m/\partial t$ is the amount of substance ∂m passing through an area S in time ∂t (the mass transfer); $\partial^2\Phi/(\partial x\partial t)$ is the rate of the magnetic-flux-gradient variation of an external electromagnetic irradiation (the term of the equation describing the transport of interstitial-metalloid atoms under the action of an external electromagnetic field at high-frequency heating of the metal, e.g., the electromagnetic transport, which takes into account the possibility of evacuating hydrogen from steel); $A = c\upsilon/(RT)$; $B = cQ^*/(RT^2)$; $C = cFZ^*/(RT)$ are the integral coefficients; D, M, R, F, Z^*, Q^*, υ, and c are the diffusivity; the gram-atom weight of diffusing substance; the universal gas constant; the Faraday constant; the effective charge—a dimensionless quantity indicating a degree of ionization of an metalloid in metal; the specific heat-transfer energy; the specific volume of intercrystalline, interfragment, and interblock spaces per 1 mole of interstitial atoms; and the concentration of interstitial atoms in metal, respectively.

The last term in Eq. (4) shows that hydrogen transport in metal is carried out under the action of a time-dependent magnetic-flux gradient and describes the mechanism of hydrogen evacuation from steel by strong external electromagnetic fields.

The modern theory for transition metals relates the interstitial-atom effective charge Z^* to the hole conductivity of a metal, and the transported heat Q^*—with the thermal electromotive force. Meanwhile, charge transport by holes is not accompanied by atomic migration in the crystal lattice—there is no mass transfer. The holes migrate by violating the neutrality of the neighboring atom during the filling of a valence bond by the transition of a valence electron from a completely bonded atom to an atom for which one of bonds remains vacant [4]. The charge (hole) transport is not related to the transport of a positively charged carrier, i.e., an ionized impurity atom. The experiments on the electrolysis of carbon in armco-iron and hydrogen in steel disproving the hole-conductivity hypothesis and confirming the interstitial-atom mass transfer under the action of an external electric field were carried out in 1948 [5] and 1928 [6], respectively.

It should be noted that the hypothesis relating the transferred heat Q^* with thermopower gives no theoretical explanation of this interpretation, and does not consider or describe the mechanism of migration of an interstitial atom under the action of the disturbing factor.

The author proposes a physical model explaining the mechanism of heat transfer [7] according to which forces assisting the displacement of hydrogen in steel towards the source of thermal radiation (energy) are related to the wave nature of electromagnetic oscillations.

On heating iron with an external heat source, the electromagnetic oscillations fall on the metal surface and penetrate into the intercrystalline, interfragment, and interblock spaces representing generally a thin wedge with a point immersed in the metal. In addition to its frequency ν, an electromagnetic field (ELMF) is characterized by two strength vectors—those of the electrical E and magnetic H fields oriented perpendicular to one another, varying by the sine law, and displacing in space along radii from a point energy radiator (PER). The order of following the vectors is defined by the right hand rule. Microvolume walls are manufactured from a ferromagnetic material—iron, which has paramagnetic properties at temperatures above the Curie point and, being soft-magnetic, has a residual magnetism because there is a constant magnetic field between the microcavity walls characterized by a magnetic-induction vector B_{FM}. The intensity lines of an external magnetic field in microvolumes (and magnetic-induction lines) are normal to the walls of the microcavities. The magnetic component of the electromagnetic flux modulates the constant magnetic field in the gap with a variable component; therefore, a stable

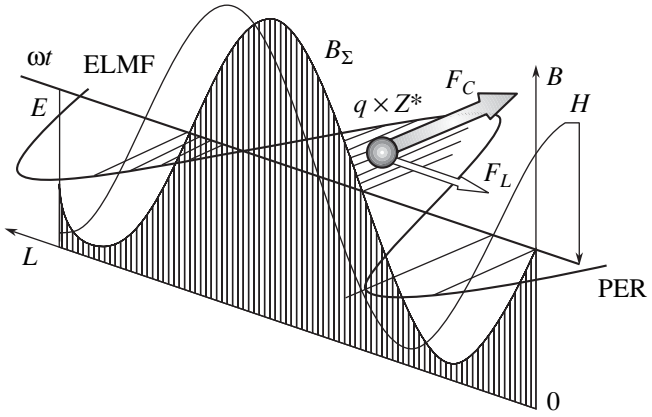

Fig. 2. Electromagnetic transport.

pulsating magnetic field oriented along the normal to the walls appears in the gap between the walls of the microvolume. This leads to polarization of the magnetic component of the electromagnetic field, the magnetic induction of which in the direction of a normal to the walls greatly exceeds the induction of the magnetic field with a different orientation in space. As a result, the symmetric sine magnetic component of the electromagnetic-field with an intensity H in the ferromagnetic-material bulk transforms into a pulsed unipolar magnetic flux characterized by the magnetic induction B_Σ.

The interstitial metalloid hydrogen occupies intercrystalline, interblock, or interfragment cavities in a pseudo-liquid atomic state, and is bound to iron by weak absorption (Van-der-Waals) forces, the binding energy ΔG_{ABS} of which is approximately from 3 to 7 kJ/mol, while the binding energy between the atoms in a molecule is 1–1.5 orders of magnitude higher.

Because the electromagnetic-field energy U_{ELMF} is equal to the product of its frequency ν and the Planck constant h

$$U_{ELMF} = h\nu, \quad (5)$$

the electrical component E of the external electromagnetic field increases with its frequency (with the radiator temperature) and breaks the weak absorption bonds of hydrogen with the iron atoms of the cavity walls, and the Coulomb force F_C displaces ionized positively charged hydrogen atoms with an effective acting charge qZ^* along the strength lines of the electrical component E of the external electromagnetic field:

$$F_C = EqZ^*. \quad (6)$$

When a particle of mass m carrying a charge qZ^* moves across the induction lines B of the magnetic field, the Lorentz force F_L displaces a particle moving with velocity V under the action of the Coulomb force given by Eq. (6) towards the source—the thermal-energy radiator (Fig. 2):

$$F_L = VBqZ^*. \quad (7)$$

If the polarity of the electrical component changes, the Lorentz force becomes much lower because the magnetic-induction magnitude B_Σ decreases. Therefore, hydrogen penetrates into a warm metal from a cold surrounding medium, but to leave steel, it is necessary that it break the absorption bonds. To do this, it is necessary to transfer certain heat energy after which hydrogen leaves the steel in the direction of the thermal-radiation source. At the same time, the ripple ratio of the total magnetic flux becomes very small in strong magnetic fields, and the Lorentz forces become approximately identical in both directions when the polarity of the electric-intensity vector E changes, and hydrogen does not leave strongly magnetized steel.

The proposed model of the heat-transfer mechanism explains the effect of migration of masses towards a radiation-energy source discovered by E.I. Demin in 1989. Under the action of photons, electrons are ejected from a substance as a result of the photoemissive effect, and microscopic particles acquire the positive charge, as a result of which, being in a weak constant magnetic field, they displace towards the radiation-energy source. The mechanism of electromagnetic transport is similar to that described for the heat transport.

A considerable effect on the hydrogen saturation of the metal forming underground pipelines is rendered by thyristor cathode stations. Because the protective-pulse amplitude U_{PP} of the pulsed thyristor protective cathode stations is more than an order of magnitude in excess of the protective potential U_P of an underground steel construct, when feeding protective pulses, the cathode protection operates always in the overprotective mode, which leads to the decomposition of the electrolyte—ground water with the release of atomic hydrogen [1, 8] which then penetrates the metal.

The hydrogen caught in intercrystalline, interfragment, or interblock spaces generates a huge pressure on the cavity walls, and itself suffers precisely the same effect on the part of microcavity walls, i.e., is under pressure, which is much higher than atmospheric; although, at the vertices of these volumes, the deep vacuum is preserved. Therefore, on the surface of a steel pipe, a concentration galvanic cell operates. Its basic current-forming reaction is oxidation on the anode sections and restoration of hydrogen on the cathode sections. The expendable material of the anode is the iron of the hydrogen-saturated walls of the pipe because the electromotive force (EMF) of the concentration galvanic cell formed by differential hydrogen saturation [9] shifts the reaction equilibrium to the right:

$$Fe \longrightarrow Fe^{2+} + 2e. \quad (8)$$

During the operation of the concentration hydrogen secondary cell, the hydrogen expenditure is constantly filled up at the expense of the permanently operating pulsed cathode protection. The electromotive force of an arbitrary galvanic pair, irrespective of the concentra-

tion c of reacting univalent components, is determined from the Nernst equation:

$$E_{EMF} = \varphi_E + 0.0592\{\Delta pH + [lg(c_2/c_1)]\}. \quad (9)$$

The concentration ratio in Eq. (9) can be replaced by the pressure ratio or the partial-pressure ratio.

Knowing the value of electrode potential φ_E for the metal of the pipe surface occurring in the electrolyte (subsoil waters), and the pH value of the medium (the near-cathode electrolyte layer), it is possible to find the hydrogen concentration in steel [10] by measuring indirect parameters—the deviations of the electrode potential of the pipeline metal from values determined by the Pourbe diagram from which the hydrogen pressure in metal can be calculated using the Nernst equation.

Hydrogen in steel is in the atomic rather than the proton state because the hydrogen-saturated surfaces serve as an electron origin (rupturable anodes) during the operation of the concentration galvanic cell of the differential hydrogen saturation [9]. Otherwise, a metal surface hydrogen-saturated by protons would serve as a cathode (the positive electrode). However, as a rule only pipes with very low (more negative) polarization potential fail from hydrogen cracking.

CONCLUSIONS

(i) A physical model of hydrogen penetration in steel taking the actual metal structure into account is proposed.

(ii) A physical model of the heat transfer and the electromagnetic transport of an interstitial metalloid atom in steel is developed.

(iii) A mathematical model of diffusion processes in steel is specified.

(iv) A method for the identification of hydrogen-saturated areas of underground gas pipelines is proposed.

(v) The effect of thyristor cathode stations on the intensification of atomic-hydrogen formation and hydrogen saturation of the pipe metal is shown.

REFERENCES

1. Orlov, P.S., Mechanism of Penetration of Hydrogen into a Steel-Pipe Wall, *Nadezhn. i Diagnost. Gazoprovod. Konstrukt.*, Moscow: VNIIGAZ, 1996, pp. 164–173.
2. Fromm, E. and Gebhart, E., *Gazy i uglerod v metallakh* (Gases and Carbon in Metals), Moscow.: Metallurgiya, 1980, pp. 126–141.
3. Orlov, P.S., Mathematical Model of Dynamic Processes of Energy-Saving Technologies of Restoring Details of Agricultural Machinery by the Method of Steel Cementation, *Energoobesp. i Energosnab. v Sel'skom Khoz.*, Moscow: GNU VIESKh, 2003, pp. 304–309.
4. Granitov, G.I., *Fizika poluprovodnikov i poluprovodnikovye pribory* (Physics of Semiconductors and Semiconductor Devices), Moscow: Sovetskoe Radio, 1977, pp. 10–12.
5. Lebedev, T.A. and Guterman, V.M., "Electrolysis" of Austenite, *Corroziya*, *Zashchita ot Korrozii i Electroliz*, Moscow: Mashgiz, 1948, pp. 156–167.
6. Bardenher, P. and Tanheiser, G., *Mitt. K. Wilh. Inst. Eisenvorschung*, 1928, vol. 10, p. 323.6, 7.
7. Orlov, P.S., Physical Model of Heat-Transfer Mechanism of an Interstitial Metalloid, *Proc. 1st Int. Sci.-Pract. Conference "Science World Potential 2004" 1–15 September 2004*, *Tekhnichni Nauki*, vol. 61, Dnepropetrovsk: Nauka i Osvita, 2004, pp. 58–61.
8. Orlov, P.S., Contactless Diagnostics of Places of Possible Stress–Corrosion Failure of Underground Backbone Gas Pipelines with a Film Water Insulation, *Trudy Mezhdunarodnogo foruma po problemam nauki, tekhniki i obrazovaniya* (Proc. of Int. Forum on Problems of Science, Technology, and Education), Moscow: AN o Zemle, 2003, pp. 43–45.
9. Petrov, L.N., Kalinkov A.Yu., Magdenko, A.N., and Osadchuk, I.P., Element of Differential Hydrogen Saturation, *Zashch. Met.*, 1990, no. 2, pp. 296–299.
10. Orlov, P.S., Goldobina, L.A., Gusev, V.P., Mokshantsev, G.F., Shkrabak, V.V., Shkrabak, V.S., and Shkrabak, R.V., RF Patent no. 2222000, *Bull. Izobret.*, 2004, no. 2.

ISSN 1068-3755, Surface Engineering and Applied Electrochemistry, 2007, Vol. 43, No. 1, pp. 44–48. © Allerton Press, Inc., 2007.
Original Russian Text © N.V. Polishchuk, M.S. Panchenko, I.M. Panchenko, 2007, published in Elektronnaya Obrabotka Materialov, 2007, Vol. 43, No. 1, pp. 57–62.

ELECTRICAL PROCESSES IN ENGINEERING AND CHEMISTRY

On the Possibility that Atmospheric and Terrestrial Electricity Affect Water Filtration

N. V. Polishchuk[a], M. S. Panchenko[a], and I. M. Panchenko[b]

[a] *Rovno State Humanitarian University, ul. Ostafova 31, Rovno, UA-33000 Ukraine*

[b] *European University of Finances, Information Systems, Management, and Business, ul. Kievskaya 64B, Rovno, UA-33028 Ukraine*

Received September 5, 2006

Abstract—The possibility of affecting water filtration via atmospheric and terrestrial electricity is discussed.

DOI: 10.3103/S1068375507010073

In [1–6], we showed that the application of inhomogeneous electric fields (IEFs) upon individual capillary tubes (CTs) and macroporous bodies, the capillary pressure in which is much lower than the hydrostatic one ($2\sigma_{12}\cos\theta/r_0 \ll \rho_1 gl\sin\alpha$), essentially affects both the height of columns and the water-absorption (filtration) rate. This phenomenon is less distinct in microcapillaries and microporous bodies in which the relation between the pressures is opposite: $2\sigma_{12}\cos\theta/r_0 \gg \rho_1 gl\sin\alpha$.

We constantly encounter the filtration phenomenon, i.e., an infiltration of water into the ground and crumbling rocks in scientific investigations, and industrial or agricultural production e.g., in the irrigation and drainage of the soil, hydrogeology, hydromechanics, simulated restoration of terrestrial water resources, discharge of sewage, flow over hydraulic engineering and electrotechnical constructions, flow of moisture through earth dams, various electrophysical and electrochemical phenomena in soils, and so on. The laws of motion of subsoil waters can be extended to motion in other porous media. Therefore, the drying and humidifying of wood and fabrics, waterproofing, the migration of juices in plants, oil extraction from wells, juice extraction from fruits and vegetables, sedimentation of weighed particles from solutions, sewage purification, etc. [7] all relate to the process of filtration.

Among the variety of natural elements, ground water and soil take the major place regarding their significance for the vital functions of mankind and are primary factors for the existence of life on the Earth.

Of all the types of binding of water (e.g., adsorbed on exterior and interior surfaces of particles or the moisture in microcapillaries, i.e., hygroscopic moisture) and states such as cable, film, and contact moisture occurring in macrocapillaries between ground particles, we are interested only in the indicated states because, without IEFs, this water moves mainly under the action of gravity through CTs (molecular forces play a negligible role) during such motion [8]. The intensity of filtration depends on the presence of the largest macropores. Steam spreads by diffusion. In the presence of a temperature gradient, additional so-called thermogradient fluxes arise; however, they are of secondary importance for small daily oscillations of ground temperature.

The enormous role groundwater plays in human affairs is in the basis of our desire to know the direction of fluid flow and reasonably control these processes in the ground. For this purpose, it is necessary to have deep knowledge of the patterns and laws of water filtration, especially, in the presence of numerous and manifold electric fields.

As was noted in [9], the principal barrier to the use of the considerable permanent atmospheric charge is that it is scattered at a small density over the entire near-earth space. Only in pre-storm conditions of the atmosphere or during a thunderstorm, do the charges concentrate in a relatively small volume (thunderclouds). Then, powerful IEFs arise and can significantly affect the filtration properties of the soil.

In fact [10], the negative charge flowing down from a cloud through a leader channel, which creates the path of lightning, fills it nonuniformly, the same as for as the channel of an arbitrary streamer. The greatest charge focuses in the head of the leader. As the leader advances, positive hydrated ions also migrate in the ground under the action of the IEF generated by it. These ions concentrate as much as possible in the area of the head of the leader channel. If the ground is homogeneous, these charges concentrate immediately under the leader channel. If the ground is inhomogeneous and has a generally high resistivity, the space charges are concentrated at places with elevated humidity and, consequently, conductance as well (i.e., subsoil water). In the ground around these areas, powerful IEFs arise and are capable of significantly affecting moisture transport in the ground. When the leader reaches the ground, reverse discharge starts. At the head of this discharge,

which is fed by the flow of positive hydrated charges from the ground in the channel, there is an area of elevated electric intensity under the action of which the plasma-charge density increases by orders of magnitude. In this case, there is a considerable reorganization of the IEF in the ground in the direction of increasing its intensity at each point. After a lightning strike, a long-term relaxation of this field, which is accompanied by a new reconstruction of the moisture-content fields in the ground, is observed. In the wider ground pores, the convective motion of moisture in the form of a vapor or fluid is initiated under the action of all the described factors associated with a lightning strike.

Nevertheless, the principal characteristic of lightning is its current, which predominantly flows along paths of elevated humidity [9]. This current arises in the interior parts of an object due to its moisture content. Because of the heating and evaporating of this moisture by the lightning current inside a porous body, the pressure sharply increases, which leads to its failure. Even after several days, it is possible to observe that rays of burnt grass radially disperse to considerable distances from the origin of a lightning strike, testifying that the lightning current was spread out in macrocapillaries of sandy loam along which positive hydrated ions and the water associated with them were pulled in. These locations appear to be much wetter; although, exactly in these directions, there was a more rapid evaporation of moisture in comparison with the neighboring areas, whereas, in the lightning epicenter (a channel of about 1 cm in diameter), the burning off of the ground and sand-particle aggregation are observed as a result of melting. This is not surprising, because the potential difference between cloud and ground can reach 10^9 V for linear lightning. Average discharge-current strength may equal approximately 10^3 A, and the average charge transported by a lightning strike is 20 C. The energy released in the lightning channel is equal to 10^9–10^{10} J. During an impulse ($\approx 10^{-3}$ s), the lightning channel is heated to 2×10^4 K. During the interval between impulses ($\approx 10^{-2}$ s) it cools down to 10^3 K. The entire lightning discharge lasts about 0.1 s.

However, it is important to emphasize that the absence of lightning does not indicate the absence of charges [10]. Both in thunderclouds, and in different types of clouds, in particular, in stratus and stratus nimbus clouds, electrical charges accumulate. Simply, a thundercloud is much more charged than, for example, a stratus cloud. It should be noted that even in atmosphere without clouds there are free electrical charges. All air space above the earth is filled with electric currents flowing from the top down—from the "heavens," to be exact, from the ionosphere, which is charged positively, to the earth's surface, which is negative. In this case, the potential difference reaches 4×10^5 V. The total negative terrestrial charge (as well as the positive charge of the ionosphere) is approximately 10^5 C. The field strength E in the atmosphere decreases with altitude. The highest value of field strength is found near the earth's surface; this equals 100 V/m in a "clean" atmosphere. Hence, the atmospheric electric field is inhomogeneous and directed vertically downward. Therefore, it should affect mass transfer in plants because they are colloid capillary–porous bodies, in the capillaries and osmotic cells of which a water-based nutrient solution moves from the roots. This process should affect the growth intensity and fruit bearing of plants.

The Earth does not lose its charge due to the ionospheric current because oppositely charged currents occur at bad-weather locations where the positive charges are transferred with lightning and precipitation from the earth surface to the negatively charged lower part of a cloud after which they pass to its upper part and, then, to the ionosphere. Thus, both the positive charge of the ionosphere and the Earth's negative charge are conserved. It should be noted that the field gradient near the surface exceeds 10^4 V/m during a thunderstorm. In addition, it is directed upward rather than downward as it is in clear weather. This means that a large positive charge focuses at this area of the Earth's surface. Around charged places in the ground as well as between them, there are powerful IEFs and currents, which affect moisture transport during filtration. Further, in the absence of thunderstorm, clouds exist, which induce relatively powerful positive charges in the ground. For a surface strength of approximately 500 V/m, the corona discharges flow in the atmosphere from pointed subjects—the tops of trees, pipes, masts, and even grass. In this case, the strength gradient ∇E is directed from the soil to the tops of plants, thus promoting the absorption of additional moisture.

In [9], it was indicated that capillary moisture can have convex menisci for certain types of alkali waters and cause a negative height h_c i.e., capillary descent. An addition, elevation of capillary moisture takes place due to the energy of hydration of ions and adsorption centers on the solid–liquid interface.

The filtration properties of the ground can be appreciably affected by powerful IEFs, which are generated due to the production of free charges during the mechanoelectrical transformations before and after an earthquake [9, 11]. This failure is manifested by the rupture of electrical bonds, and the occurrence of free electrical charges, signals, and a current. At the earliest stages of the mechanical action on solid rocks, the mechanoelectrical transformations are developed in the tectonic epicenter, and a powerful free-charge concentration appears; i.e, a strong IEF source arises. Before tectonic phenomena, for example, strong earthquakes, and during them, electrical phenomena are frequently observed on the surface of the ground. For tens of minutes or less before the first shock, the electric-field strength E in the atmosphere increases by hundreds or thousands of volts per meter. In this case, the atmospheric electric field increases such that ionization and luminescence appear in the air. Several days before the first shock of a strong

earthquake, high IEFs are generated in the earth's crust, electric currents flow, the resistance of an area of the earth's crust decreases (this includes effects due to moisture transport under the action of IEFs and current), and the geomagnetic field in the epicenter region varies.

According to [9], the primary energy supply is located in space in the form of gravitational energy, which the Earth experiences as gravity waves. Because of this, the Earth's mass increases. An increase in the mass and volume of our planet is accompanied by the occurrence of tectonic shifts and, naturally, mechano-electrical transformations, which essentially affect the redistribution of the moisture in the lithosphere and, consequently, in the ground. In the depths of the Earth, the electrical-energy density is much higher than in the atmosphere. In rocks, this electric strength can achieve 3×10^7 V/m [9, 11].

Earthquakes on our planet occur virtually continuously: there are about ten each hour. Earthquakes with catastrophic consequences occur, on average, once a year.

Due to earthquakes, seismic waves of two types (longitudinal P and transversal S) arise. In addition, L-type waves propagate from an epicenter in the Earth's crust. In this case, seismic energy including electric-field energy [12] is released.

Thus, due to earthquakes, the Earth's crust contains high-strength constant as well as alternating electric fields, which, undoubtedly, should affect the phenomenon of subsoil-water filtration.

Arbitrary industrial production is the source of a different kind of technogenic pollution. The majority of physical pollution is in the form of constant and alternate electromagnetic fields of various frequencies up to X-rays. Huge fluxes of electrical energy, when the enormous scale of its production is taken into account, flow in the ground through the ground connections of electrical power equipment in the millions, wireless and electrical equipment, and the neutral groundings of high-voltage transmission lines. In the ground, and preferentially in the soil, manifold types of stray IEFs and currents are scattered. All of them affect mass and heat transfer in the ground, thus reconstructing temperature and moisture-content fields and, consequently, changing the velocity and direction of water-migration processes, heat transport via hot water, water evaporation, and vapor condensation [13–17]. For this reason, the necessity of investigating the electrophysical mechanisms of these phenomena is increasing, before they develop into an ecological catastrophe [18]. During electrophysical action, all physical properties of water [19, 20] change, as well as those of bound water [17, 21], which is in the strong electric field of a surface of ground pores.

For the majority of actually existing ground (sand, clay, peat, rocky cracked ground, etc.), Darcy's law is fulfilled:

$$v = -k\frac{dh}{dl}, \tag{1}$$

where v is the filtration rate; k is the filtration coefficient; h is the piesometric pressure or simply pressure; and l is the distance measured along a line. In addition, at an arbitrary moment and at an arbitrary point (x, y, z)

$$h = \frac{p}{\rho_1 g} + z, \tag{2}$$

where p is the hydrostatic pressure, ρ_1 is the water density, g is the gravity acceleration, and z is the geometrical height.

Taking into account that a fluid filling a porous medium is under the action of gravity ρg directed vertically downward, in the presence of an electrical force f_e, which is directed vertically upwards, Eq. (2) can be rewritten as

$$h_e = \frac{p}{\rho_1 g - f_e} + z. \tag{3}$$

In this case,

$$\vec{f}_e = \sigma_b^e \nabla E - 0.5\varepsilon_0 E^2 \nabla\varepsilon_1 + 0.5\varepsilon_0 \nabla\left[E^2\left(\frac{\partial\varepsilon_1}{\partial\rho_1^e}\right)_T \rho_1^e\right]$$
$$+ \frac{0.5\varepsilon_0(\varepsilon_2 E_2^2 - \varepsilon_1 E_1^2)}{h_s} + \rho_e E + \frac{\varepsilon_0\varepsilon_1 z_i}{\varphi_0 h_e}$$
$$\times \int\left(\frac{\imath}{\sigma_e}\right)^2\left(\frac{\imath dr}{\sigma_e}\right) \pm \frac{\Delta p}{\delta_e'} + \frac{\sigma_{12}^{e2}}{2\varepsilon_0\varepsilon_1 h_s} + \frac{q^2\cos^4\theta_e}{16\pi^2\varepsilon_0\varepsilon_1 r_0^4 h_s} \tag{4}$$
$$+ \frac{0.5\varepsilon_0\varepsilon_1}{\delta_e'^3}\frac{l_e U^2}{\left(r_0 - \chi - \frac{\chi}{a'}\right)\ln\left(r_0/\left(r_0 - \chi - \frac{\chi}{a'}\right)^2\right)}$$
$$- 0.5\varepsilon_0 E^2\left(\frac{\partial\varepsilon_1}{\partial T}\right)_{\rho_1}\nabla T,$$

where σ_b^e is the bound-charge density in the meniscus; ε_0 is the permittivity of free space; ε_1 is the permittivity of fluid; ε_2 is the permittivity of steam–air medium; h_s is the width of a near-surface fluid layer, which is saturated by ions of corona or spark discharges; ρ_e is the bulk fluid-charge density; z is the valence of ions; $\varphi_0 = kT/e$ is the specific potential, e is the elementary charge; i is the electric-current density; r_0 is the CT radius; dr is the of radius increment during the motion from the CT axis; σ_e is the fluid conductivity; Δp is the additional pressure to the atmospheric on the part of the corona wind or the spark-discharge plasma in the CT; δ_e' is the distance between the IEF source and the meniscus; q is

the charge of the water-column top; χ is the double electrical-layer thickness, and a' is the stationary value depending on fluid and CT-wall-surface properties; $l_e = h_e/\sin\alpha$ is the water-column length in the CT tilted at an angle α to the horizon under the IEF action; and h_e is the water-column height of the CT in the vertical position.

The expression for f_e consists of a number of summands, which describe the force effect of the IEF on both the volume of a fluid and its surface layers in the CT [13, 22–25, 26–32], exactly: (i) the suction force of a water column as a macrodipole in the peak-strength area E of the field [13]; (ii) the force acting on a unit volume of an uncharged fluid under isothermal conditions during the interaction between the IEF and polarization charges, which causes the motion of a dielectric fluid in the direction opposite to $\nabla\varepsilon$ (into the area of smaller ε values (gas)) [23]; (iii) the striction force affecting the resultant force if this body (fluid) is enclosed by other dielectric medium [23]; (iv) the surface force acting on the part of the field on the phase interface and directed into the area with a smaller value of ε ($\varepsilon_1 > \varepsilon_2$) and a higher magnitude of E ($E_2 > E_1$), that is, on the interface between fluid and steam–air medium, the IEF forces act on bound electrical charges in the direction opposite to the surface-tension forces σ_{12} of water or a water solution which, under certain conditions, leads to a meniscus deformation, capillary-wave generation, destruction of the water–air boundary, and dispersion of fluid and reconstruction of the two-phase (with bubbles) flow [24]; (v) the bulk ponderomotive force, which acts on the charged fluid [22, 26]; (vi) the force related to inhomogeneous specific distribution of σ_e and E during the flow of direct electric current [27]; (vii) the forces, which change the fluid acceleration because of the pressure on the meniscus exerted by the corona discharge or spark-discharge plasma [25, 28]; (viii) the electrical force originated as a result of saturating a meniscus by one-sign ions [29] and coincident with the direction of the Laplace force (an action similar to that described in (iv)); (ix) the IEF-action force due to which the conditions of its top destruction change [30]; (x) the force compressing a fluid in the direction of the CT axis when its walls and the fluid are charged by identical charges [22, 31], which leads to squeezing water from the CT; and (xi), the electro-thermo-hydrodynamical force which originates due to the existence of a temperature gradient ∇T and is directed oppositely [32, p. 95], which accelerates the fluid motion to the CT cold end.

From Eq. (3), it follows that IEF ponderomotive forces, undoubtedly, should affect the filtration rate and, consequently, water-flux magnitude under IEF action

$$j_1^e = \rho_1^e v_e,$$

where v_e is the filtration rate of the flux in the IEF, and ρ_1^e is the density of water in the IEF.

Taking into account the complexity of Eq. (4) and its possible inadequacy, probably, the determination of the filtration-flux magnitude in the IEF represents the upper limit; nevertheless, this study should be carried out.

REFERENCES

1. Karpovich, I.N., Panchenko, M.S., Panasyuk, A.L., and Churaev, N.V., Effect of Inhomogeneous Electric and Magnetic Fields on the Absorption of a Fluid by Capillary–Porous Bodies, *Elektron. Obrab. Mater.*, 1982, no. 4, pp. 62–66.
2. Polishchuk, N.V., Panchenko, I.M., Panchenko, M.S., and Karpovich, I.N., Effects of Electric Fields on Raising Water in Macrocapillaries and their Consequences, *Elektron. Obrab. Mater.*, 2002, no. 4, pp. 54–67.
3. Polishchuk, N.V., Panchenko, I.M., Panchenko, M.S., and Karpovich, I.N., Effect of Electric Fields on Migration of Water in Capillary Tubes, *Elektron. Obrab. Mater.*, 2003, no. 4, pp. 27–36.
4. Polischuk, N.V., Panchenko, I.M., Panchenko, M.S., and Karpovich, I.M., Effect of an Electric Field on Water-Migration Rate in a Wide Capillary Located under a Small Angle to Horizon, *Elektron. Obrab. Mater.*, 2003, no. 6, pp. 25–33.
5. Polishchuk, N.V., Panchenko, I.M., and Panchenko, M.S., Moisture-Transfer Effect on the Heat Transfer under the Effect of an Inhomogeneous Electric Field in Conical Capillaries, *Inzh. Fiz. Zh.*, 2004, vol. 77, no. 4, pp. 121–127.
6. Polischuk, P.V., Panchenko, I.M., Panchenko, M.S., and Mosievich, A.S., Intensification of Moisture and Heat Transfer during the Capillary Absorption of Water by Macroporous Medium at a Combined Effect of Inhomogeneous Temperature, Electric and Gravity Fields, Abstracts of papers, *V Minskii internatsional'nyi forum po teplo- i massobmenu* (V Minsk Int. Conf. on Heat and Mass Transfer), Minsk, GNU "Lykov Institute of Heat and Mass Transfer, Belarussian Academy of Sciences, Belarus," May 24–28, 2004, vol. 2, pp. 240–241.
7. Lyashko, I.P., Sergienko, I.V., Mistetskii, G.E., and Skopetskii, V.V., *Voprosy avtomatizatsii resheniya zadach filtratsii na EVM* (On Automation of Solving the Filtration Problem on Computer), Kiev: Naukova Dumka, 1977.
8. Lykov, A.V., *Yavleniya perenosa v kapilyarno-poristykh telakh* (Transfer Phenomena in Capillary–Porous Bodies), Moscow: Gos. Izd Techn.-Teor. Lit., 1954.
9. Vorob'ev, A.A., Earth-Crust Electricity as a New Power Source, *Elektron. Obrab. Mater.*, 1980, no. 3, pp. 40–46.
10. *Tekhnika vysokikh napryazhenii* (High-Voltage Equipment), Razevig, D.V., Ed., Moscow: *Energiya*, 1976.
11. Kobranova, V.N., *Fizicheskie svoistva gornykh porod* (Physical Properties of Rocks), Dr. Sci. (Geol.-Mineral.) Dakhnov, V.N., Ed., Moscow: Gos. Nauchn.-Techn. Izd. Neft. i Gorno-Topl. Lit., 1962.
12. Brown, G.C. and Mussett, A.E., *Inaccessible Earth*, London, UK: George Allen and Unwin, 1981.

13. *Sil'nye elektricheskie polya v tekhnologicheskikh protsessakh: elektronno-ionnaya tekhnologiya* (Strong Electric Fields in Technological Processes: Electron–Ion Technology), Collect. of Papers, Academician Popkov, V.I., Ed., no. 3, Moscow: Energiya, 1979.
14. But, A.P., *Osnovy elektronnoi technologii stroitel'nykh materialov* (Fundamentals of Electron Technology of Building Materials), Moscow: Lit. po stroit., 1968.
15. Bernatskii, A.F., Tselebrovskii, Yu.V., and Chunchin, V.A., *Elektricheskie svoistva betona* (Electrical Properties of Concrete), Doct. Sci. (Techn.) Vereshchagin, Yu.N., Ed., Moscow: *Energiya*, 1980.
16. Novikov, M.P. and Fedorov, A.M., *Vlagostoikost' radioelektronnoi apparatury* (Moisture-Resistance of Radioelectronic Equipment), Moscow: Radio i svyaz', 1981.
17. Nerpin S.V. and Chudnovskii, A.F., *Fizika pochvy* (Soil Physics), Moscow: Nauka, 1967.
18. Bilyavskii, G.O., Padun, M.M., and Furdui, R.S., *Osnovi zagalinoi ekologii* (Fundamentals of General Ecology), Kiev: Libid', 1995.
19. Eizenberg, D. and Kauzman, W., *The Structure and Properties of Water*, Washington, D.C.: Science, 1951.
20. Usatenko, S.T., About Electrophysical Effect on Hydrogen-Containing Fluids, *Elektron. Obrab. Mater.*, 1980, no. 3, pp. 46–50.
21. Greg S.G. and Sing K.S.W., *Adsoption Area and Porosity*, New York: Academic Press, 1967.
22. Denisov, A.A. and Nagornyi, V.S., *Elektrogidro- i elektrogazodinamicheskie ustroistva avtomatiki* (Electrohydro- and Electrogasdynamic Devices of Automation), Leningrad: Mashinostroenie, 1979.
23. Tamm, I.E., *Osnovy teorii elektrichestva* (Fundamentals of Theory of Electricity), Moscow: Nauka, 1976.
24. Bologa, M.K., Smirnov, G.F., Didkovskii, A.B., and Klimov, S.M., *Teploobmen pri kipenii i kondensatsii v elektricheskom pole* (Heat Exchange at Boiling and Condensations in an Electric Field), Doct. Sci. (Techn.) Vasil'ev, Ed., Chisinau: Stiinta, 1987.
25. Kaptsov, N.A., *Koronnyi razryad* (Corona Discharge), Moscow–Leningrad: Gostekhizdat, 1947.
26. Bologa, M.K., Grosu, F.P., and Kozhukhar', I.A., *Elektrokonvektsiya i teploobmen* (Electrical Convection and Heat Exchange), Chisinau: Stiinta, 1977.
27. Ostroumov, G.A., Distribution of Mechanical Forces in Fixed Electrolyte for Arbitrary Configuration of Electrodes, *Elektron. Obrab. Mater.*, 1975, no. 2, pp 37–40.
28. Ostroumov, G.A., *Vzaimodeistvie elektricheskikh i gidrodinamicheskikh polei* (Interaction of Electric and Hydrodynamic Fields), Moscow: Nauka, 1979.
29. Grosu, F.P., Bologa, M.K., and Kozhukhar', I.A., Theoretical Aspects of Effect of Electric Field on Miscibility, *Elektron. Obrab. Mater.*, 2004, no. 1, pp. 42–45.
30. Koekin, V.K., Effect of an Electric Field on a Fluid Jet, *Elektron. Obrab. Mater.*, 1990, no. 4, pp. 43–45.
31. Grigorov, A.I., Shiryaeva, S.O., and Egorova, E.V., About Certain Features of Nonlinear Resonance Interaction of Modes of Charged Jet, *Elektron. Obrab. Mater.*, 2005, no. 1, pp. 42–49.
32. Landau, L.D. and Lifshits, E.M., *Elektrodinamika sploshnykh sred* (Electrodynamics of Continuum), Moscow: Nauka, 1982.

ISSN 1068-3755, Surface Engineering and Applied Electrochemistry, 2007, Vol. 43, No. 1, pp. 49–52. © Allerton Press, Inc., 2007.
Original Russian Text © A.I. Vasil'ev, L.M. Vasilyak, S.V. Kostyuchenko, N.N. Kudryavtsev, M.E. Kuzmenko, V.Ya. Pecherkin, 2007, published in Elektronnaya Obrabotka Materialov, 2007, Vol. 43, No. 1, pp. 63–67.

ELECTRICAL PROCESSES IN ENGINEERING AND CHEMISTRY

Investigation of the Effect of a Protective Layer on Parameters of Quartz Low-Pressure Gas-Discharge Lamps with Oxide Electrodes

A. I. Vasil'ev[a], L. M. Vasilyak[a], S. V. Kostyuchenko[a], N. N. Kudryavtsev[b], M. E. Kuzmenko[a], and V. Ya. Pecherkin[a]

[a] *ZAO NPO LIT, ul. Krasnobogatyrskaya 44, korp. 1, Moscow, 107076 Russia*

[b] *Moscow Institute of Physics and Technology, Institutskiĭ per. 9, Dolgoprudnyĭ, Moscow oblast, 141700 Russia*

Received October 9, 2006

Abstract—Low pressure amalgam lamps are widely used for disinfection of air and water surfaces. The application of amalgam instead of pure mercury makes it possible to design a high-efficiency powerful ultraviolet lamp and to improve the ecological impact of disinfection equipment. This paper describes the effect of oxide electrodes and a quartz inner surface on the lifetime of a lamp and on the ultraviolet-intensity reduction in low pressure lamps. We show that the burning time of the noble-gas arc discharge at a low pressure depends on the interaction between the discharge plasma and the inner quartz surface. Use of a rare-earth-metal-oxide protective layer on the inner quartz surface increases the lifetime of the lamp and prevents ultraviolet-intensity reduction in low-pressure amalgam lamps.

DOI: 10.3103/S1068375507010085

The presence of a protective layer of rare-earth-metal oxides on the inner surface of quartz flasks increases the operation time of low-pressure arc-discharge lamps with inert gases and retards the decrease in the ultraviolet-radiation intensity for low-pressure amalgam lamps.

Lamps with a low-pressure arc discharge are widely used for generating ultraviolet (UV) and visual radiations. The effective operation time of such lamps ranges from several hundreds of hours for spectral lamps to several thousand hours for xenon and mercury lamps [1, 2]. During operation, the intensity of the radiation of such lamps decreases. For example, for UV glass low-pressure bactericidal lamps, the UV-radiation intensity can decrease to approximately 50% of its initial value after 3500 hours of operation [2]. It is known that in bactericidal low-pressure lamps manufactured from uviol glass, mercury ions, which are present in the low-pressure discharge plasma, interact with the inner surface and penetrate deep into the glass [3]. This is possible because the uviol glass contains up to 15 mass % of Na_2O. The sodium-ion mobility in glass is sufficient to allow penetration of mercury ions from the surface into the volume [3]. This leads to decreasing the number of mercury atoms in the discharge and to glass darkening. This last situation results in a decrease in the UV-radiation intensity that reduces the useful operation time of the lamp. The presence of a protective coating on the inner surface of UV bactericidal lamps of uviol glass prevents the deep penetration of mercury ions into the glass, decreases their velocity, and considerably increases the effective operation time to 10000–12000 hours [4]. For example, when disinfecting water by exposure to UV radiation, powerful high-performance bactericidal lamps with a long operation time, and which experience only a small intensity decrease over time, are required. For manufacturing such lamps, quartz is used because it has a higher fusion temperature and is a steadier material than glass due to its lack of the alkali-earth-metal ions which favor the penetration of mercury ions into the quartz volume. The UV-radiation intensity of quartz lamps decreases by 50% over approximately 6500 hours of operation [5].

The purpose of this work is to investigate the effect of a protective layer on the inner quartz surface on the parameters of the low-pressure arc discharge in an inert-gas mixture and on the UV-radiation intensity of powerful amalgam low-pressure lamps.

We used lamps with a 16.6 mm inner diameter of the quartz-tube and three-spiral oxide electrodes. During their manufacture, all lamps received the complete conventional technological treatment, including high-temperature processing in a vacuum, and were filled with a mixture of spectroscopically pure inert gases (neon and argon). The lamps were supplied with a stabilized ac current of 1.85 ± 0.1 A at a frequency of 45 ± 3 kHz from electronic start controlling devices (ESCDs).

If the inert-gas pressure decreases, the discharge-burning duration decreases from several thousands of hours at pressures of 5–10 Torr to several hundreds of hours at 1 Torr and to 1 hour at a pressure of 0.3 Torr. It was experimentally established that this life time

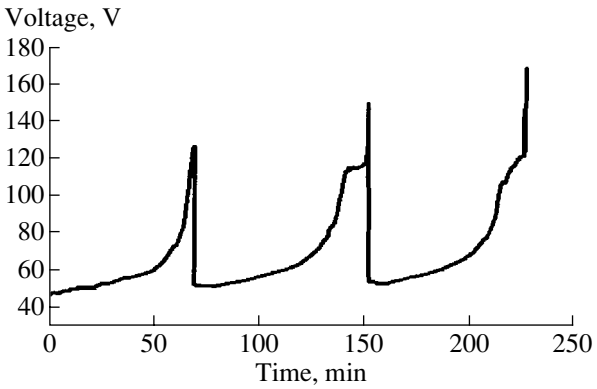

Fig. 1. Time dependence after changing the gas mixture.

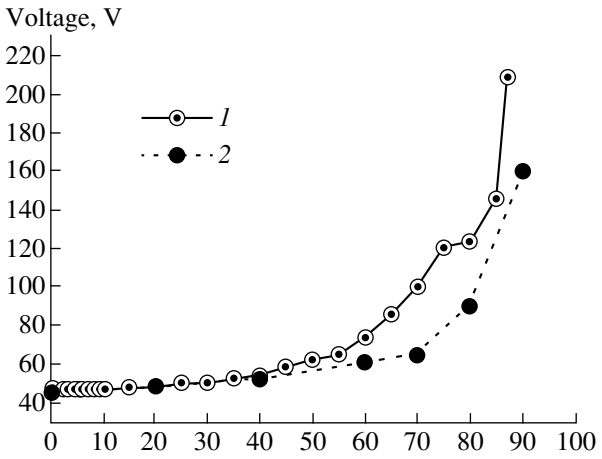

Fig. 2. Time dependence of the burning voltage across the lamp (*1*) with permanently burning discharge fed by the ESCD and (*2*) with the HF discharge.

changed only slightly as the discharge-tube length was varied several-fold. We assumed that the burning duration depends on the interaction of the plasma with the quartz wall rather than with the oxide electrodes of the lamps. To confirm this assumption, we manufactured the quartz lamp with a discharge-gap length of 450 mm. After technological treatment, the lamp was left on the evacuation post and filled with an argon–neon mixture to a pressure of 0.3 Torr, and its volume was separated from the vacuum-system volume of the post by a special valve. In this lamp, the discharge was ignited, and the voltage drop was monitored for a steady discharge current. After spontaneous quenching of the discharge, the gas mixture was replaced with a new one with the same composition and pressure. After switching on the ESCD, the discharge ignited and steadily burned. The discharge burning time was virtually equal to that in the first case. This procedure was repeated, the data from these two repetitions on the dependence of the voltage across the lamp on the burning time is given in Fig. 1. Thus, we found that the discharge-quenching process at low inert-gas pressures depends on the filling-gas composition in the quartz lamp during burning rather than the properties of oxide electrodes.

To be completely convinced that the change in the filling-gas composition is caused by the quartz-wall effect instead of gassing products from oxide electrodes, we carried out the following experiment. We manufactured two identical lamps, which were unsoldered from the evacuation-post vacuum system after filling with inert gases. In one lamp, the discharge was ignited from the ESCD, and a voltage drop was measured. In the second lamp, a high-frequency (HF) electrodeless capacitive discharge was ignited. In this case, the oxide electrodes were outside the area of the HF discharge in order to eliminate their effect on the discharge plasma. After a period, the HF capacitive discharge was quenched and, for approximately 1 min, the discharge was ignited using the ESCD, and the voltage across the lamp was measured. The discharge was switched off, and the HF capacitive discharge was ignited in the lamp again. This procedure was executed until it was possible to ignite the discharge from the ESCD. These results are shown in Fig. 2. As can be seen from the figure, the voltage across both lamps grew virtually identically. Hence, the change in the voltage drop across the lamp at low inert-gas pressures is determined by variation of the filling-gas composition during the discharge burning which is caused by the interaction of the discharge plasma with the quartz wall rather than with the oxide electrodes of the lamps.

In order to investigate the effect of a protective layer on the burning duration, we manufactured four groups of quartz lamps (with three lamps in each group), the discharge-gap length was 450 mm, and the pressure of the argon–neon mixture was 0.3 Torr. Lamps from the first group were the experimental control. On the inner surface of the quartz tubes of the lamps of the second, third, and fourth groups, we deposited a protective layer of a rare-earth-metal oxide, with coats of 50, 75, and 100% of the inner-surface area of the lamps, respectively. Figure 3 gives the averaged dependence of the voltage across the lamp with inert-gas discharge on time for all four groups of lamps. These curves have two strongly pronounced portions with different slopes. After switching off the lamp, the voltage slowly increased to a certain critical value after which rapid voltage growth took place, which ended with the spontaneous quenching of the lamp discharge because the working voltage across the electronic power supply was restricted. The reignition of the arc discharge in the lamp was impossible. The duration of the first portion of the curve was minimal for lamps without a protective layer and maximal for lamps with their inner surface completely covered with a protective layer. The transition from the first portion to the second portion of the curve occurred at a voltage of approximately 70 V for all lamps, which corresponds to an electric-field intensity of 1.2–1.3 V/cm in the positive column of the discharge. To verify the assumption that the voltage

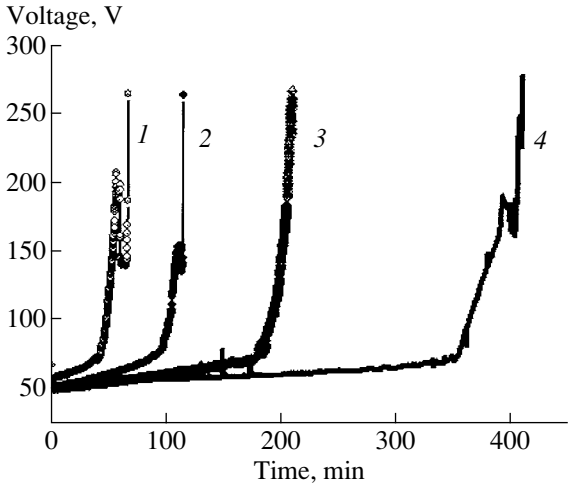

Fig. 3. Operation-time dependences of the voltage across lamps with various areas (in %) of the protective layer on the tube inner surface: (*1*) 0; (*2*) 50; (*3*) 75; and (*4*) 100.

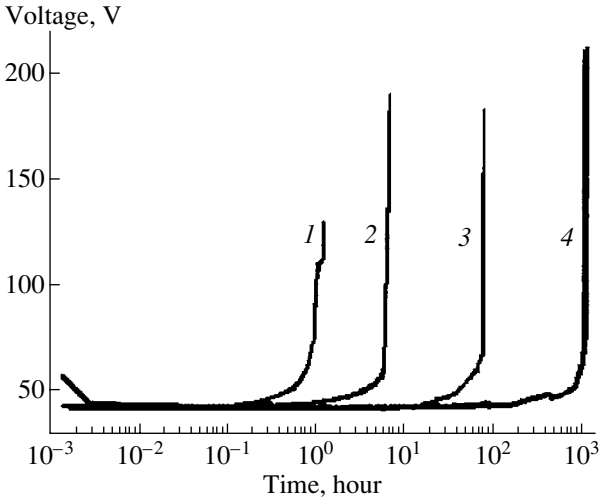

Fig. 4. Burning-time dependence of the voltage across lamps for various thickness of the protective layer: (*1*) without a layer, with (*2*) one layer, (*3*) two layers, and (*4*) three layers.

increased in the positive column, we investigated the lamp with a discharge-gap length of 1440 mm lacking a protective layer. For this lamp, we observed also two characteristic portions in the voltage curve; the transition from the first portion to the second one occurred at a field gradient of approximately 1.25 V/cm as well, whereas the durations of the first portion of the curve were identical for the lamps with a different discharge-gap length. These results enable us to also confirm that the slow lamp-voltage growth during the first portion of the curve was determined by the effect of the inner quartz wall contacting with the discharge plasma on plasma properties. The presence of the rare-earth-metal-oxide protective layer on the inner surface of the quartz lamp flask reduced the interaction between the discharge plasma and quartz and increased the operation time of the lamps with inert-gas discharge at a pressure of 0.3 Torr almost by an order of magnitude in comparison with that of the lamps without the protective coating.

To investigate the effect of a protective-layer quality on the burning duration of lamps, we manufactured four groups of lamps with the following parameters: the discharge-gap length was 450 mm, the argon-neon-mixture pressure was 0.3 Torr. The first group of lamps were the experimental control, while we deposited protective layers of rare-earth-metal oxide on the inner surface of the quartz tubes of lamps of the second, third, and fourth groups. The second-group lamps had one protective layer, those of the third group—two, and those of the fourth group—three. In Fig. 4, we show the dependences of the voltage across lamps on the burning time. As the number of protective-coating layers increased, the burning time of lamps increased. If the lamp without the protective coating burned for approximately one hour, the lamp with three protective-coating layers burned for approximately 1000 hours, that is, three orders of magnitude longer.

To investigate the effect of the protective layer on the UV-radiation intensity of lamps with a mercury-vapor discharge during long-term burning, we manufactured six samples of quartz amalgam lamps with a discharge-gap length of 1440 mm. On the inner surface of the quartz tubes of three lamps, we deposited a rare-earth-metal-oxide protective layer transparent to bactericidal-range UV radiation. The three remaining lamps lacked this layer. Both groups of lamps were filled with the same mixture of inert gases to a pressure of 2.0 Torr. As the mercury-vapor source, we used indium amalgam, which enabled us to obtain the maximum UV-radiation power for a lamp electrical power of 240 W. During the operation of the amalgam lamps, we measured the voltage across the lamp, the UV-radiation intensity at a wavelength of 253.7 nm, and the quartz-wall transmittance of the lamp flask at a wavelength of 253.7 nm. The voltage-measurement accuracy amounted to 0.5%, and the relative error did not exceed 2.5% and 3.5% in measuring the UV-radiation power and transmittance, respectively.

Figure 5 shows the dependence of the intensity and transmittance of the UV radiation on the operation time of the lamps with a protective layer and without it, averaged for all the lamps from each group. The UV-radiation intensity at the point corresponding to 100 operation hours of the lamp was taken as 100% according to the conventional method for estimating a decrease in the UV-radiation intensity of luminescent and bactericidal low-pressure lamps [1]. When measuring the UV-radiation transmittance, the transmittance of air was taken as 100%. In Fig. 5, it can be seen that the UV-radiation intensity of lamps with the protective coating was 80% of the initial value in 10000 hours of burning

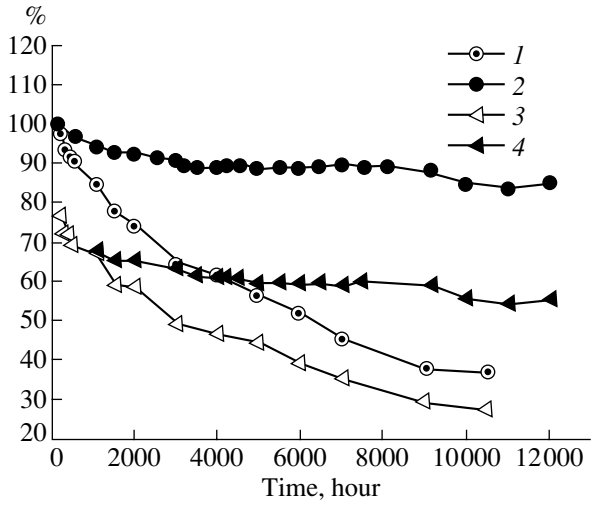

Fig. 5. Operation-time dependences of the UV-radiation intensity (*1*, *2*) and the quartz transmittance (*3*, *4*) for an amalgam lamp. (*1*, *3*) without the protective layer and (*2*, *4*) with the protective layer.

and less than 40% of the initial value for the lamps without a protective coating. It is necessary to note that the time dependence curves correlate well with the UV-radiation curves for the dependence of transmittance for lamps both with the protective coating and without it. The voltage across all lamps was virtually invariable during their operation. Hence, it is possible to assume that the parameters of the discharge and plasma do not change during the operation of amalgam lamps with a protective coating and that the decrease in UV radiation is determined by a decrease in its transmission through the lamp wall.

CONCLUSIONS

(i) In the absence of a protective layer, the quenching of the low-pressure discharge (P = 0.3 Torr) in quartz lamps is caused by a change in the filling-gas composition of the lamp.

(ii) The filling-gas composition varies due to the interaction between the discharge plasma and the quartz surface.

(iii) The presence of a protective layer of rare-earth-metal oxides on the inner surface of quartz lamps with an arc discharge in inert gases increases the operation time of low-pressure lamps and, hence, decreases the degree of interaction of discharge plasma with quartz.

(iv) An increase in the number of protective layers of rare-earth-metal oxides on the inner surface of quartz lamps with the arc discharge in inert gases increases the discharge-burning time by several orders of magnitude.

(v) The protective coating considerably retards the drop in the UV-radiation intensity during the operation of low-pressure amalgam lamps.

(vi) A decrease in UV-radiation intensity is caused by decreasing the quartz-flask transmittance for UV radiation during operation of the amalgam lamps.

REFERENCES

1. Rokhlin, G.N., *Razryadnye istochniki sveta* (Discharge Light Sources), Moscow: Energoatomizdat, 1991.
2. *Spravochnaya kniga po svetotekhnike* (Handbook on Light Engineering), Aizenberg, Yu.B., Ed., Moscow: Energoatomizdat, 1995.
3. Hildenbrand, V.D., Denissen, C.J.M., Geerdings, L.M., et al., Interactions of Thin Oxide Films with a Low-Pressure Mercury Discharge, *Thin Solid Films*, 2000, vol. 371, pp. 295–302.
4. UK Patent Application GB 2124019 A.
5. Vasil'ev, A.I., Kostyuchenko, S.V., Pecherkin, V.J., et al., Effect of a Heat-Treatment Degree of Oxide Electrodes on the Initial Decrease in Bactericidal Radiation of Powerful Amalgam Quartz Low-Pressure Lamps, *Izv. RAN. Ser. Fiz.*, 2003, vol. 67, no. 9, pp. 1310–1313.

ISSN 1068-3755, Surface Engineering and Applied Electrochemistry, 2007, Vol. 43, No. 1, pp. 53–58. © Allerton Press, Inc., 2007.
Original Russian Text © N.I. Botosan, M.K. Bologa, S.E. Berzoi, 2007, published in Elektronnaya Obrabotka Materialov, 2007, Vol. 43, No. 1, pp. 68–75.

ELECTRICAL TREATMENT OF BIOLOGICAL OBJECTS AND FOODSTUFFS

Intensification and Optimization of Heat Treatment of Raw Vegetable Matter by Electroplasmolysis

N. I. Botosan, M. K. Bologa, and S. E. Berzoi

Institute of Applied Physics, Academy of Sciences of Moldova, ul. Academiei 5, Chisinau, MD-2028, Republic of Moldova

Received October 10, 2006

Abstract—Intensification and optimization of heat treatment (drying, boiling, evaporation, and frying) of raw vegetable material by modeling the specific heat conductivity coefficient and dividing the treatment process into stationarity stages are considered. Three main models of a one-dimensional equation of heat conductivity in the presence of heat energy sinks depending on time are investigated. Optimization of the heat loss level is carried out. Correlations between the mode of heating, geometrical parameters, and level of electroplasmolysis of raw biological material are found. To simplify analysis, we consider the simplest geometrical forms of raw material (plane, cylindrical, and spherical). This approach makes it possible to optimize stages of the heating process, geometrical, dimensional parameter, and level of electroplasmolysis of treated medium.

DOI: 10.3103/S1068375507010097

INTRODUCTION

Earlier [1], the modeling of the heat conductivity coefficient of a biological medium for the optimization of heat treatment during moisture evaporation, taking into account preliminary electroplasmolysis of raw material, was carried out. The special importance of the liquid fraction for heat treatment was specified, and formulae for the evaporation rate and intensification effect in the assumption of heat supply from plane-parallel surfaces of heating were derived. Analogous investigations of heat fields of the cylindrical and spherical symmetries are of interest in terms of the analytical description of the heat processes of drying, frying, and boiling of raw biological material, because they are often realized for biological items close to these geometrical forms. The form approximation allows for the determination of the parameters and dependences of the intensification effect and the foodstuff evaporation rate. Revealing the correlation between the geometrical dimensions of foodstuffs and the heat supply mode is also of interest for energy-efficient technologies and regimes.

In biological media, the heat conductivity is made more complex by the endothermal effect of heat absorption in the raw bulk material. The availability of heat sinks through the constant power consumption is characteristic of the stationary stages of raw biological material treatment. Nonstationary heat conductivity is shown at transitions between the heat stationarity stages, and its duration is less than 10% of the heat treatment process. Bulk heating takes place until the temperature field inside the raw material is stabilized at the level of the given treatment stationarity stage. The peculiarity of boiling, frying, and drying the foodstuffs of a certain form lies in the equalization of the temperature field according to the heating of the surface temperature and the form of the analytical dependence on the coordinate being preserved.

Heat treatment may be formally divided into separate processes, where the heat fields differ only in terms of the boundary conditions of heating and the heat characteristics of the medium. Below, the heat treatment analysis for various processes is provided: drying from the foodstuff surface, convection drying with hot air, moisture evaporation in the raw bulk material, boiling, moisture evaporation in bulk by heating the raw material in oil, and frying. An analytical description of each stage of heat treatment allows us to find the principal characteristics, which provide the possibility of controlling the process and optimizing the expenditure and efficiency taking into account electroplasmolysis.

The investigation of solutions to the heat conductivity equation in the stationary mode is carried out considering one-dimensional problems for plane-parallel slices of the cylindrical and spherical forms of raw material. The form parameter is a one-denominator quantity. The mode parameters are the heating temperature and the critical temperature of the liquid–vapor phase transition; the biological medium characteristics are the coefficients of heat conductivity and specific heat in the case of drying, as well as the characteristics of capillaries and level of the medium electroplasmolysis. In the case of convection drying, the process parameters are temperature, density, and rate of air circulation.

ROLE OF ELECTROPLASMOLYSIS IN HEAT TREATMENT OF VEGETABLE MATTER

The specific characteristics of the processes of electric charge, heat, and mass transfer in vegetable matter depend on the ratio of the parts of the liquid fraction content in the intracellular vacuoles and in the intercellular space [2]. The plasmolysis state is determined by the condition of the whole intracellular liquid transition into the free state for the transfer when the medium cellular structure is completely destroyed. Let us note that analytical models for the description of the medium specific kinetic characteristics have a similar dependence on medium parameters: content of dry substances z and part of the free liquid fraction x. Part of the intracellular liquid is determined from the condition for completeness $y(x, z) = 1 - x - z$. Thus, the corresponding relative specific kinetic coefficient of a vegetable medium is presented by the analytical expression

$$\frac{\sigma(x, z)}{\sigma_L} = \frac{\gamma(1-x) + xz(1-\gamma)}{\gamma(1-x) + z(1-\gamma)},$$

where σ_L is the specific kinetic coefficient of the liquid fraction; $\gamma = \sigma_S/\sigma_L$, where σ_S is the specific kinetic coefficient of the dry medium substances; $\sigma(x, z)$ denotes one of the specific kinetic coefficients of the medium transfer; σ is the electric conductivity; λ is the heat conductivity; and D is the specific diffusion. Let us note that electroplasmolysis also leads to a modification of the dielectric permeability coefficient ε and time $\tau_M = \varepsilon/\sigma$ which determines the free-charge relaxation in the medium.

Electroplasmolysis results in vegetable medium transformations reduced to the transition of the intracellular part of the liquid fraction into a state of free intratissue liquid—or, a solution of dry substances. Thus, electroplasmolysis of a vegetable medium, where the extracellular liquid part initially was x_0, transforms all kinetic characteristics of the transfer processes through the value determined by the difference

$$\frac{\sigma(1-z, z) - \sigma(x_0, z)}{\sigma_L} = \frac{z(1-\gamma)^2(1-x_0-z)}{\gamma(1-x_0) + z(1-\gamma)} \geq 0.$$

Modeling of this difference for heat transfer in vegetable matter is based on the composite coefficient of heat conductivity determined by specific characteristics of heat conductivity of the liquid fraction λ_L and dry substances of the medium λ_S. The heat conductivity coefficient of the liquid fraction is practically identical for the intracellular and extracellular components λ_L = 0.58 W/(m K). The heat conductivity coefficients of dry substances in vegetables are approximately five times less than λ_L and are correspondingly equal to 0.02–0.13 W/(m K) for potatoes, 0.12 W/(m K) for carrots, 0.13–0.36 W/(m K) for beet, and 0.15–0.19 W/(m K) for tomatoes [3]. The heat conductivity coefficients of dry substances in fruit and vegetables dried by sublimation to the state of a mash are hundreds of times less than the heat conductivity of water. For example, the heat conductivity coefficients of the media with a moisture content of 5% are equal to 0.029–0.038 W/(m K) in grape mash; 0.030–0.03 W/(m K) in cherry mash; 0.035–0.037 W/(m K) in apple mash; 0.026–0.034 W/(m K) in a fruit mixture; and 0.021–0.023 W/(m K) in potato mash. These data are the basis of the effective application of electroplasmolysis before heat treatment of plant-growing products. The maximum effect of the heat treatment intensification is achieved when the parameter γ tends to zero

$$\lim_{\gamma \to 0} \frac{\sigma(1-z, z) - \sigma(x_0, z)}{\sigma_L} \approx 1 - x_0 - z.$$

PHASE EQUILIBRIUM AT EVAPORATION FROM A FREE SURFACE

The analytical description of the drying process is grounded by the condition of the water molecular equilibrium in various phases at their interface. In the thermodynamic process of evaporation, the substance particle number N is an independent variable; therefore, a member proportional to the particle number must be added to the extensive (additive) thermodynamic functions of enthalpy, inner, free, and Gibbs energies. The equality of the chemical potential $\mu_S(P, T) = G/N$ (where S is the phase index) of both liquid and gaseous phases corresponds to the Gibbs energy minimum $G(P, T, N)$. The two-phase liquid–gas system possesses one degree of freedom only, so the equilibrium state in the (P, T) diagram will be shown by a curve of coexistence of two aggregate states of water.

The chemical potential determined in variables P and T serves for the description of the equilibrium state and the derivation of the equilibrium curve $P_S = P(T)$, the points of the latter showing values of P and T at which water can exist simultaneously in two aggregate states: liquid and vapor.

The Clapeyron–Clausius equation determines, for equilibrium between the phases, the evaporation heat dependence on temperature, the bulk change at the phase transition, and the pressure derivative with respect to temperature $Q = T\Delta V\frac{dP_S}{dT}$. The experimental points [4] of this curve in various ranges with respect to temperature lie down the parabolas shown by the following analytical formulae and Figs. 1–3:

$$P_S = (1.17t^2 - 14.67t + 62.28)10^{-4}\ \text{kg/cm}^2,$$

$$0 \leq t \leq 100^\circ\text{C}$$

$$P_S = (1.44t^2 - 282.69t + 14938.2)10^{-3}\ \text{kg/cm}^2,$$

$$100 \leq t \leq 200^\circ\text{C}$$

$$P_S = (6.2t^2 - 2357.99t + 239286.66)10^{-3}\ \text{kg/cm}^2,$$

$$200 \leq t \leq 374^\circ\text{C}.$$

Here, t is the centigrade temperature. The range interpolation of the equilibrium curve is realized within the accuracy of the deviation not exceeding 1%; additionally, the ranges with respect to temperature may be any of those not exceeding 200 degrees.

Thus, due to liquid evaporation at a given temperature, the partial pressure of vapor may increase only to the limit determined by the saturated vapor pressure according to the equilibrium curve $P_S = P(T)$. The presence of water vapors in air is determined by humidity (ratio of water vapor mass to the bulk). The removal of water vapors out of the bulk creates the conditions for surface evaporation depending on the liquid properties and the surface structure. For vegetable media, the surface capillarity structure and the liquid viscosity, depending obviously on electroplasmolysis level, are of special importance.

In contrast to free liquid evaporation from a free surface, drying is characterized by a peculiar vapor formation from the raw material surface. For the drying of a biological object of a plane form of thickness d, the rate of heat flow spreading inside the raw material a is determined by its heat conductivity $\lambda(x, z)$, the temperature difference of the heating surface T_0, and the central part of the slice T_C, and is expressed by the formula [1]

$$a = \frac{8\lambda(T_0 - T_c)}{q\rho d^2},$$

where q is the specific heat of evaporation and ρ is the raw material density.

At the liquid transition into vapor, water molecules overcome molecule cohesive forces in the liquid. The work of exiting and overcoming the external pressure of already formed vapor are realized due to the kinetic energy of the molecule heat movement. Therefore, for the evaporation process proceeding at a constant temperature, it is necessary to supply a certain quantity of heat, otherwise the liquid will cool.

The cuts and surfaces of biological media are porous structures pierced by a great number of capillaries. The mass transfer in this medium depends on the electroplasmolysis level through the specific diffusion coefficient $D(x, z)$. Hence, a larger drying surface favors more efficient evaporation, taking into account a huge number of capillaries for the liquid transfer to the surface. During drying, the vapor pressure at the entry of a porous substance capillary is equated to the liquid pressure in the capillary

$$P_g - \frac{\rho_b \nu^2}{2} = P_l + \frac{2\sigma_N \cos\alpha_N}{r},$$

where P_g and P_l are the pressures in the gaseous and liquid phases, ρ_b is the air density, ν is the convection flow velocity, σ_N is the liquid surface tension, r is the capillary radius, and α_N is the wetting angle at the water–capillary boundary.

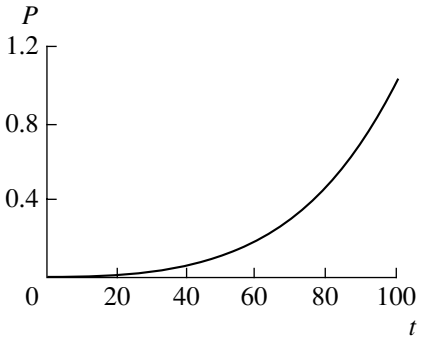

Fig. 1.

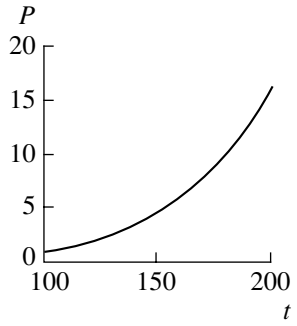

Fig. 2.

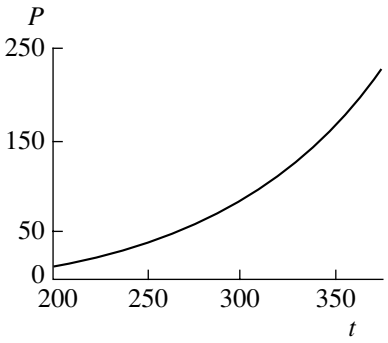

Fig. 3.

According to the Joule–Thomson effect for the Van der Waals gas, near the surface of a raw biological material sample subject to drying, the difference of vapor temperatures in the capillary and on the surface of the sample at the heat equilibrium is the following:

$$T_g - T_l = \left(\frac{2\alpha}{RT_l} - \beta\right)\frac{P_g - P_l}{C_p}$$

$$= \frac{0.424}{C_p}\left(\frac{2\sigma_N \cos\alpha_N}{r} + \frac{\rho_b \nu^2}{2}\right),$$

where C_p is the specific heat at a constant pressure. The Van der Waals constants for water vapor are correspond-

ingly equal to $\alpha = 5.65$ at $m^6/kmol^2$, $\beta = 0.031$ $m^3/kmol$, and $R = 8.314 \times 10^3$ j/(kmol K). The calculation is carried out for room temperature.

In practically every capillary of the raw material surface, the evaporation determined by the liquid supply to the surface-by-surface tension forces and convection suction takes place. In the case of convection drying with hot air, the temperature difference determined by the external temperature of liquid heating from the raw material surface should also be taken into account, substituting $T_0 - T_C = (T_g - T_l) + (T_l - T_C)$, where T_l is the liquid phase temperature near the raw material surface.

HEAT ENERGY SINKS AT RAW BIOLOGICAL MATERIAL TREATMENT

Assuming the heat conductivity coefficient after electroplasmolysis is $\lambda(x, z)$, analysis of the heating process may be divided into stationarity stages, when the temperature field of the medium heating depends on the parameter q_v/λ which determines the temperature gradient in a stable mode of heating per unit length of the region subject to heating. The characteristics of stationarity stages of the process are various heat sinks q_v described by a physical parameter of each of the several stages of heating: heating, boiling, evaporation, and frying of biological media. Here, we consider those cases of the heating process description by the solution of a one-dimensional equation of heat conductivity with boundary conditions for the simplest geometrical forms of the medium: the plane, cylindrical, or spherical forms. This approach allows fine optimization of the process under study by the heating mode and geometric dimensional parameter of the medium subject to heating. On the other hand, staging the description of the temperature field allows for the consideration of the classical processes of heat treatment: drying, boiling, and frying of biological media of certain geometrical forms. The most interesting forms are the plane–parallel cut slice, cylinder, hollow cylinder, and sphere. At different stages of the heat treatment process, the temperature fields of these geometrical forms have one dependence on the dimensional parameter. The only difference is the sink description parameter q_v/λ containing typical heat characteristics of the stage, electroplasmolysis level, and rate of processes.

Stages of the process of heat treatment of raw biological material in a stationary mode, determined by heat sinks and temperature, divide the process into stages with respect to the analytical form of the description of the heat absorption parameter. For example, at the raw material heating stage, the value q_v determines the heat energy $q_v = -C_m\rho_m b_m(T_C - T_m)$ absorbed by the medium of density ρ_m and heat capacity C_m (where T_C is the water boiling temperature and T_m is the initial temperature of the medium). The parameter b_m determines an average rate of medium heating measured in units of inverse time s^{-1}. At the stage of bulk evaporation of moisture, $q_v = -q\rho a$, where a is the value determining the rate of moisture evaporation in the raw bulk material [1].

The stage of raw material heating after moisture evaporation is determined by a modified sink $q_v = -C_n\rho_n b_n(T_0 - T_C)$, where ρ_n and C_n are the density and heat capacity of the dehydrated raw material. The value b_n determines the heating rate at the raw material dehydration stage.

At raw material frying, one should also determine the heating stage when the thermal transformation of the biological medium characteristics (coagulation, setting) takes place: $q_v = -q_k\rho_k a_k$, where q_k, ρ_k, and a_k are the values analogous to the moisture evaporation stage relating to the thermal transformation of the raw material albumen mass.

Thus, the study of the process of heat treatment of the raw biological material allows analytical and staging interpretation, making it possible to derive criteria for heat process efficiency and to optimize the process with respect to the level of minimal heat loss. Furthermore, the temperature field dependence on the coordinate, being characteristic of all stationarity stages, has a common character.

TEMPERATURE FIELD OF A CYLINDER

The heat conductivity equation for a cylinder with a constant isotropic coefficient of heat conductivity has the form

$$\frac{d^2T}{dr^2} + \frac{dT}{rdr} + \frac{q_v}{\lambda} = 0,$$

where q_v is the bulk density of the heat energy absorbed by sinks at evaporation in the moisture-containing bulk medium: $q_v = -q\rho a$, where ρ is the liquid density and a is the rate of change of the medium liquid fraction part. Assuming q_v/λ is constant in the cylinder bulk (homogeneous medium), let us write a solution for the temperature field $T(r)$ and the heat flow $\Phi(r)$ in the form

$$T(r) = -\frac{q_v r^2}{4\lambda} + C_1 \ln r + C_2,$$

$$\Phi(r) = -\lambda\left(-\frac{q_v r}{2\lambda} + \frac{C_1}{r}\right).$$

The temperature field and the heat flow are equal in value on isothermal surfaces of the cylindrical form (dependence on one coordinate r). The heat flow is equal to zero on the surface $r = r_S$, if the constant C_1 is determined by the ratio $C_1 = \frac{q_v r_S^2}{2\lambda}$. The temperature of the zero-flow surface $\Phi(r_S) = 0$ is determined by the formula

$$T_S = -\frac{q_v r_S^2}{4\lambda} + \frac{q_v r_S^2}{2\lambda}\ln r_S + C_2.$$

Hence, the cylinder temperature field may be expressed by the equation

$$T(r) = T_S - \frac{q_v}{4\lambda}(r^2 - r_S^2) + \frac{q_v r_S^2}{2\lambda}\ln\frac{r}{r_S}.$$

The temperature on the cylinder surface is equal to the heating temperature T_0, so

$$T_0 - T_S = \left(-\frac{q_v r_0^2}{4\lambda}\right)(1 - \gamma^2 + \gamma^2\ln\gamma^2), \quad \text{where } \gamma = \frac{r_S}{r_0}.$$

Let us obtain the isothermal surface of the zero flow $\Phi(r_S) = 0$ coinciding with the cylinder symmetry axis $r_S = 0$. Then, the temperature on the cylinder axis will be determined by the ratio $T_S = T_0 = \frac{q_v r_0^2}{4\lambda}$, and the cylinder temperature field for the optimal heating mode will take the form

$$T(r) = T_0 + \frac{q_v}{4\lambda}(r_0^2 - r^2).$$

An ideal agreement of the heating temperature T_0 of the raw material of the cylindrical form with the dimension characteristic of the cylinder radius r_0 will take place only in the case when the temperature on the cylinder axis is equal to zero. Thus, between the heating temperature and dimension of the raw material of the cylindrical form at drying, frying, or heating in a stationary mode there exists an agreement $T_0 = q\rho a r_0^2/4\lambda$. In other words, the mode of moisture evaporation inside the bulk of the cylindrical form is determined by the basic parameter of the heating mode T_0, dimension of the cylinder r_0, and heat characteristics of the raw material ρ, $\lambda(x, z)$, and $q : a = 4\lambda T_0/\rho q$.

If we consider the case when the heat flow on the surface $r = r_s$ is assumed to differ from zero ($\Phi(r_S) = \Phi_S$), then $C_1 = q_v r_S^2/2\lambda - r_S\Phi_S$. Analogously, the isothermal surface temperature may be introduced $T_S = -\frac{q_v r_S^2}{4\lambda} + \frac{q_v r_S^2}{2\lambda}\ln r_S - r_S\Phi_S\ln r_S + C_2$, and, then, for the cylinder temperature field we obtain the expression

$$T(r) = T_S - \frac{q_v}{4\lambda}(r^2 - r_S^2) + \left(\frac{q_v r_S^2}{2\lambda} - r_S\Phi_S\right)\ln\frac{r}{r_S}.$$

According to this formula, the temperature on the heating surface depends on the parameters of an arbitrary point of the surface $r = r_S$ and the flow on it

$$T_0 = T_S - \frac{q_v r_0^2}{4\lambda}(1 - \gamma^2) - \left(\frac{q_v\gamma r_0^2}{2\lambda} - r_0\Phi_S\right)\gamma\ln\gamma.$$

In the limit, when an arbitrary surface $r = r_S$ coincides with the cylinder axis, the temperature on the axis depends only on the heating temperature and cylinder radius through characteristics of the heat sinks and the medium heat conductivity coefficient, and it is expressed by the ratio $T_S = T_0 + q_v r_0^2/4\lambda$. It is characteristic that this formula does not contain the dependence on the heat-flow value on the axis.

In the absence of heat sinks ($q_v = 0$), for example, at raw material frying in oil, when the inner moisture has already evaporated, the surface temperature ($r = r_S$) becomes equal to the heating temperature T_0. The requirement for the surface r_S to coincide with the cylinder center leads to the known expression for the cylinder temperature field.

Heating of cylindrical tubes is of a special interest; e.g., for boiling of tubular macaroni or frying and baking rolls and buns in the form of a hollow cylinder. In this case, the obvious requirement $T_S = T_0$ leads to the ratio for the flow

$$\Phi_S = \frac{q_v r_S}{2\lambda} - \frac{q_v(r_0^2 - r_S^2)}{4\lambda r_S\ln(r_0/r_S)}.$$

The temperature field of a hollow cylinder is determined by the ratio

$$T(r) = T_0 - \frac{q_v}{4\lambda}(r^2 - r_S^2) + \frac{q_v}{4\lambda}(r_0^2 - r_S^2)\ln\frac{r}{r_S}/\ln\frac{r_0}{r_S}.$$

The temperature takes on a minimal value on the isothermal surface

$$r = r_m = \sqrt{\frac{r_0^2 - r_S^2}{\ln\left(\frac{r_0}{r_S}\right)^2}} = r_S\sqrt{\frac{\gamma^2 - 1}{\ln\gamma^2}}, \text{ where } \gamma = \frac{r_0}{r_S},$$

being equal to $T_m = T_0 - \frac{q_v}{4\lambda}\left(r_m^2 - r_S^2 - r_m^2\ln\left(\frac{r_m}{r_S}\right)^2\right)$.

TEMPERATURE FIELD OF RAW BIOLOGICAL MATERIAL OF THE SPHERICAL FORM

The temperature field and heat flow in raw material of the spherical form are determined by the solution of the Fourier stationary equation with spherical symmetry at different stages of heating. The heat conductivity equation for an isotropic sphere, its medium satisfying the condition of homogeneity of heat conductivity coefficients and the specific heat of sources, has the form

$$\frac{d^2(RT)}{RdR^2} + \frac{q_v}{\lambda} = 0.$$

The equation of the temperature field $T(R)$ and heat flow $\Phi(R)$ is determined by formulae

$$T(R) = -\frac{q_v R^2}{6\lambda} + C_1 + \frac{C_2}{R},$$

$$\Phi(R) = \lambda\left(\frac{q_v R}{3\lambda} + \frac{C_2}{R^2}\right).$$

The isothermal surface of the zero flow $\Phi(R_S) = 0$ is determined by choice of the integration constant $C_2 = -\frac{q_v R_S^3}{3\lambda}$.

As a result, the formula of the sphere temperature field takes the form

$$T(R) = -\frac{q_v R^2}{6\lambda} + C_1 - \frac{q_v R_S^3}{3\lambda R}.$$

The temperature of the zero-flow surface allows determination of the first constant of integration

$$T_S = -\frac{q_v R_S^2}{2\lambda} + C_1.$$

The sphere temperature field may be expressed by the formula

$$T(R) = T_S + \frac{q_v R_S^2}{2\lambda} - \frac{q_v R^2}{6\lambda} - \frac{q_v R_S^3}{3\lambda R}.$$

The temperature on the sphere surface correlates with the temperature of the zero-flow isothermal surface by the ratio

$$T_0 = T_S + \frac{q_v}{6\lambda R_0}(3R_S^2 R_0 - R_0^3 - 2R_S^3).$$

The temperature field depends on coordinates of the isosurfaces of heating and zero flow in the following way:

$$T(R) = T_0 + \frac{q_v R_0^2}{6\lambda}\left(1 - \frac{R^2}{R_0^2}\right) - \frac{q_v R_S^3}{3\lambda R}\left(1 - \frac{R}{R_0}\right).$$

When the heat treatment process is realized for a sample of the spherical form, maintaining the optimal mode requires meeting the condition $T(R_{\min}) = 0$, which leads to the necessity of keeping the criteria of heating at drying

$T_0 = -\frac{q_v R_0^2}{6\lambda}$ for raw material without stones, and

$T_0 = \frac{q_v R_0^2}{6\lambda}\left(-1 + 3\frac{R_S^2}{R_0^2} - 2\frac{R_S^2}{R_0^2}\right)$ for raw material with stones of the radius R_S.

The heating temperature for drying is equal to zero if $R_S = R_0$, which corresponds to the absence of mass for heating. Hence, heating intensification and the temperature gradient decrease depend on the thickness of the layer subject to heat treatment $\delta = R_0 - R_S$. Agreement of the heating temperature T_0 with the layer thickness δ is of principal importance for obtaining high quality foodstuffs by drying. In the most widespread case of drying, when full-scale evaporation takes place, the properties of the raw biological material capillaries should be taken into account.

Thus, the study of the processes of heat treatment of biological media, based on a stationary solution of the equation of heat conductivity with heat sinks, allows us to optimize heating stages and to derive criteria connecting the heating mode with dimensional parameters of the raw material geometry [1]. Practically, the evolution of the heat treatment stages must be described through the complex changes in time of both the heat field and the heat flow, and inner heat sinks. Staging of the heat treatment process makes it possible to consider stable parameters of heating at the treatment stages and to derive useful criteria. For example, in the case of raw biological material boiling, the heating temperature is always below 100°C, which indicates its decreased value inside the raw material in comparison with the boiling temperature.

The main aspect in the control of raw vegetable material heat treatment is the modeling of the heat transfer coefficient $\lambda(x, z)$ through electroplasmolysis. Modeling of the kinetic characteristics of transfer processes by electroplasmolysis of raw material cells is described in [2]. Modeled coefficients of electric conductivity $\sigma(x, z)$, heat conductivity $\lambda(x, z)$, and the specific diffusion $D(x, z)$ of biological media allow for the estimation of the duration of heat treatment stages, with their intensification determining heat energy saving and the improvement of the quality of the final product.

REFERENCES

1. Botosan, N.I., Bologa, M.K., and Berzoi, S.E., Intensification of Heat Exchange in Biological Medium by Electroplasmolysis, *Elektron. Obrab. Mater.*, 2005, no. 1, pp. 68–75.
2. Botosan, N.I., Bologa, M.K., and Berzoi, S.E., Model for Description of Electroplasmolysis of Two–Component Biological Raw Material, *Elektron. Obrab. Mater.,* 2005, no. 2, pp. 64–68.
3. Ginsburg, A.S., Gromov, M.A., and Krasovskaya, G.I., *Teplofizicheskie kharakteristiki pishchevykh produktov. Spravochnik* (Heat Physical Characteristics of Food Stuffs. Handbook), Moscow: Pishchevaya Promyshlennost', 1980.
4. *Tablitsy fizicheskikh velichin. Spravochnik* (Tables of Physical Quantities. Handbook), Acad. Kikoin, I.K., Ed., Moscow: Atomizdat, 1976.

ISSN 1068-3755, Surface Engineering and Applied Electrochemistry, 2007, Vol. 43, No. 1, pp. 59–64. © Allerton Press, Inc., 2007.
Original Russian Text © A.P. Malyushevskaya, P.P. Malyushevskii, 2007, published in Elektronnaya Obrabotka Materialov, 2007, Vol. 43, No. 1, pp. 76–81.

EQUIPMENT AND INSTRUMENTS

A Novel Method to Control Electrical-Discharge Nonlinear Bulk Cavitation

A. P. Malyushevskaya and P. P. Malyushevskii

Institute of Pulsed Processes and Technologies, Ukrainian National Academy of Sciences, Oktyabr'skii pr. 43 A, Nikolaev, 54018 Ukraine

Received September 18, 2006

Abstract—Experimental results from the study of cavitation generated in a liquid during underwater synchronous parallel discharges are presented. It is shown that only synchronous discharges permit the productions of large cavitation regions in a free liquid. The cavitation parameters may be controlled through variation of operational tensile stresses.

DOI: 10.3103/S1068375507010103

Earlier we described the generation of nonlinear bulk cavitation by electrical discharge [1, 2], which strongly depends (given identical parameters of the discharge circuit) on the discharge chamber geometry, the relative arrangement of the discharge reactor bottom, its walls, and the free liquid surface in it, the reactor's design rigidity, and the magnitude of the external static pressure in the liquid filling the reactor. In such electrical discharge reactors, cavitation is excited upon the reflection of primary pressure waves (the underwater electrical discharge is actually an electrical explosion) from the free liquid surface in the reactor and its walls, which confine the total liquid volume. Usually the conventional radius of analogous reactors is 2 to 3 times the radius of the post-discharge cavity.

Electrical discharge cavitation is generally used for the treatment of small objects, and at first inspection the small dimensions of the electrical discharge reactor do not play a decisive role. But this is so only for batch or continuous treatment of small volumes of materials. When the treatment of substantial volumes of materials in a large water (working fluid) quantity is needed, all the reflecting surfaces that confine the discharge zone should be placed at large distances (5–10 radii of the post-discharge cavity or greater). Their efficiency becomes insignificant.

Hence, the search for methods to excite an effective electrical discharge cavitation in large open volumes of a working fluid, for example, in the technological tanks of conveying units for processing fibrous materials, is an urgent problem.

One of the most convenient ways to reach this goal is to use converging pressure waves generated in the region of the underwater electrical discharge [3, 4].

A simple scheme for the interaction of underwater pressure waves is shown in Fig. 1.

When the converging pressure waves reach the position denoted by 3, conditions arise behind the intersection points of the fronts that favor excitation of cavitation. These conditions arise because upon the electrical explosion the depression (stretching, expansion) waves definitely follow the pressure (compression) waves that lead to the disruption of liquid continuity. These cavitation regions exist for a short time, but their role is very

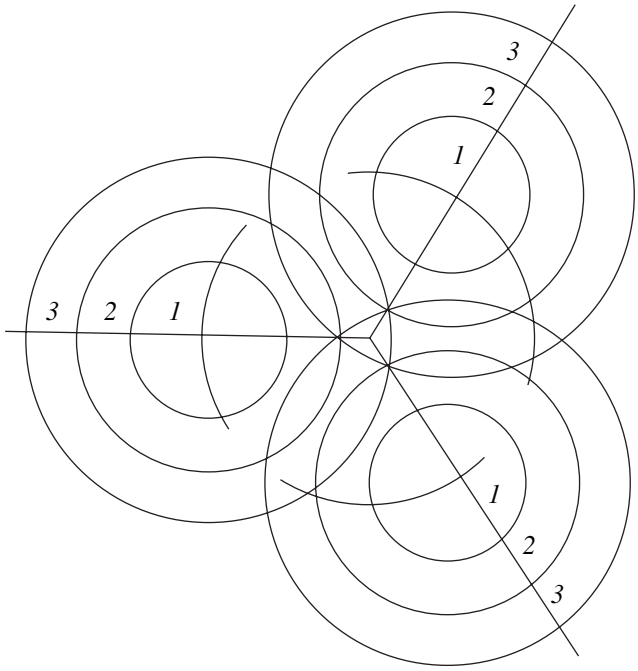

Fig. 1. Scheme of the interaction of three converging electrical discharge shock waves ("trishocks"). (*1*), (*2*), and (*3*) position of the shock waves in various time moments.

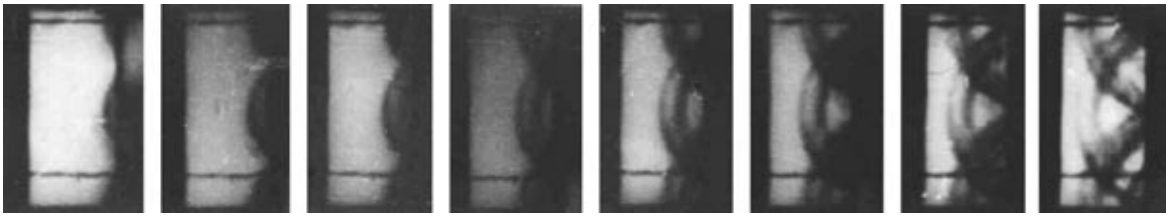

Fig. 2. Shadowgraph of the interaction process of three pressure-depression waves.

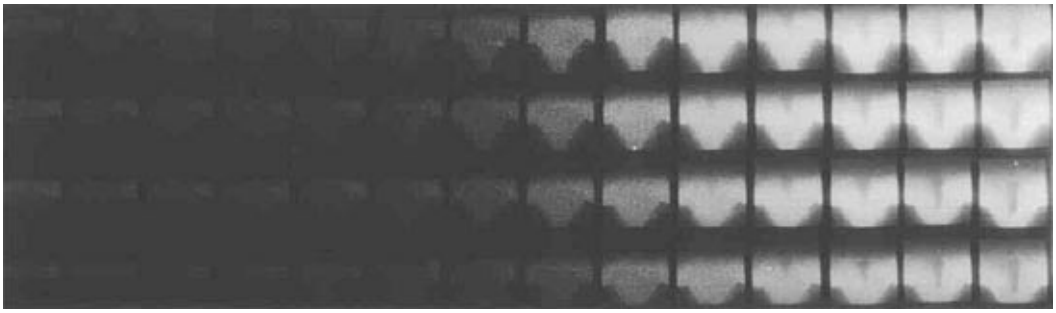

Fig. 3. Film record of the process of high-power cavitation excited in a large-volume reactor.

important as they activate the near-discharge space, thus generating numerous cavitation nuclei in it.

As it is known [5, 6], eventually the discharge channel transforms into a post-discharge vapor and gas cavity, which expands, and its subsequent collapse is initiated when the internal pressure in it decreases to the magnitude of the external pressure. Upon the motion of the cavity shell inward, tensile stresses arise in the medium that favor cavitation genesis.

The shadowgraph of the interaction process of three pressure–extension waves is presented in Fig. 2. The dark cavitation regions are clearly seen behind the points where the fronts intersect. As the cavitation process subsides, these regions become lighter because the basic mass of cavitation bubbles collapses in the pressure field leaving tiny cavitation nuclei. Cavitational disruptions of the liquid continuity should arise after the collapse of the post-discharge cavity on these cavitation nuclei alone.

Earlier we observed a similar phenomenon in a somewhat different situation [5]. This event occurred upon the interaction of the converging plane shock waves at a relatively large distance from the place where the electrical explosion was excited.

A film record is shown in Fig. 3 of the process of high-power cavitation excitation in a large-volume reactor due to the interaction of two plane shock waves that were produced in water using plasma accelerators; the accelerator end-walls can be seen at the frames (in each corner below). The characteristic feature of the experiments is the ability to obtain converging shock waves in a controllable manner in a strictly specified region of the discharge chamber, where they are directed from two accelerators at a pulse energy in each accelerator of 6–12 KJ. Such a technique allowed the generation of a relatively uniform cavitation region at a large distance from the solid boundaries relatively isolated from post-discharge vapor and gas cavities (i.e., avoiding direct contact). This provided the opportunity to investigate the electrical discharge cavitation in its pure form.

Over a period of approximately 55 μs after synchronized current pulses are applied on the plasma accelerators, in the bulk of the liquid (in a region centered approximately at the intersection point of the accelerators' axes) a local cavitation region arises (Fig. 3). It very quickly (in less than 10 μs) takes a tapered shape with characteristic dimensions such that the base width is 4–6 cm, the length is 4–6 cm and the variable height is 6–1 cm. This primary stable cavitation region in the form of a mist-like cloud of very fine ($r \le 3$ μm) high-density (up to 5×10^6 1/cm^3) cavitation bubbles is excited by the converging shock waves generated by plasma accelerators; the depression waves follow behind their front.

This detailed examination of the local cavitation region allows the observation that the region moves very quickly and changes its direction of motion. The velocity of motion of the head part of this primary cavitation region is equal to from 0.5 to 1.5 km/s, these pulsations last over 150–200 μs after the formation of the mist-like structure. These characteristics depend significantly on the convergence angle of the shock waves,

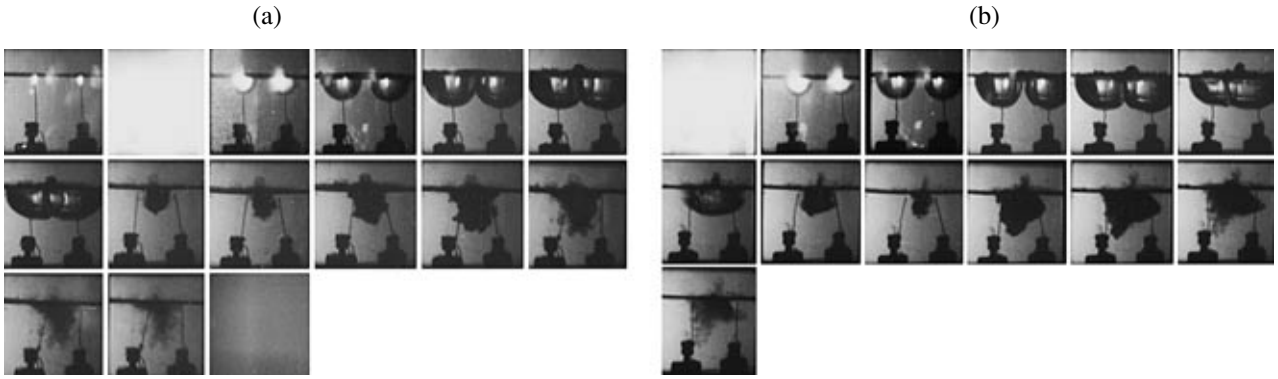

Fig. 4. Initiation and evolution of the cavitation region between thin rod-type electrodes for parallel electrical discharges: (a) strictly synchronous ($\Delta t = 0$); (b) when the initiation of one of the discharges is delayed ($\Delta t = 2$ μs).

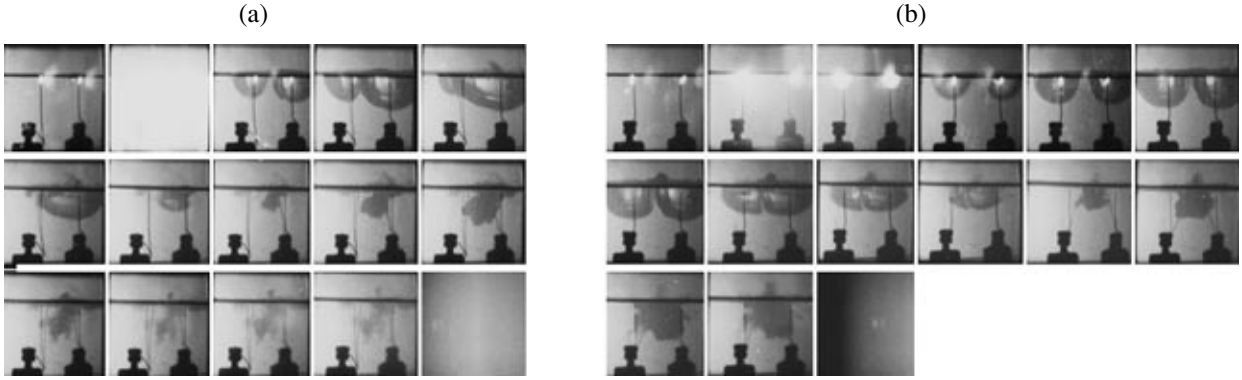

Fig. 5. Elements that control the cavitation region for parallel electrical discharges: (a) when initiation of one of the discharges is substantially delayed ($\Delta t = 8$ μs); (b) strictly synchronous discharges ($\Delta t = 0$), for working voltage $U_1 = 17.8$ KV (frames 11–14).

the pulsations of the post-discharge vapor and gas cavities, and on the compression waves in the plasma accelerators.

During the entire period of these pulsations in the primary cavitation region, a cavitation layer, whose thickness increases rather smoothly, emerges in the subsurface space due to excitation by primary shock waves of plasma accelerators reflected from the surface in the counterphase. Starting from frame 12 (about 50 μs after the local tapered cavitation region emerged), cavitation also becomes noticeable in the lower space of the discharge chamber that pulsates synchronously with the pulsations of the primary cavitation region.

Over 220–250 μs the shock wave reflected from the free surface returns as a depression wave into the region under examination and in the next 50–70 μs the bulk cavitation spreads over the entire liquid volume being studied (see Fig. 3), and then over the whole volume of the discharge chamber. At this point the dimensions of the cavitation bubbles increase substantially (up to 0.1–1.0 mm) compared with the dimensions of the cavitation bubbles in the local cavitation region.

Evidently, these converging plane shock waves are an effective means to generate cavitation in the discharge chamber. But this method cannot be considered cost-efficient, as the system of underwater plasma accelerators is very expensive, and additional energy costs are high. The search for other methods for control of the underwater electrical discharges that may provide maximal cavitation in a free volume per each discharge pulse is urgent. Therefore, the unique possibilities of converging and diverging underwater pressure waves operating as generators of cavitation processes should be studied.

EXPERIMENTAL STUDIES

We studied the processes of genesis of cavitation region in a free volume of a liquid upon the interaction of two post-discharge cavities. These cavities were generated by discharges produced in parallel manner taking the adopted hypothesis into account. The following parameters of the discharge circuits were chosen: the working voltage U_0 was 25 KV, electrical capacitance C was 1 μF, the discharge gap l_d was 10 mm, the dis-

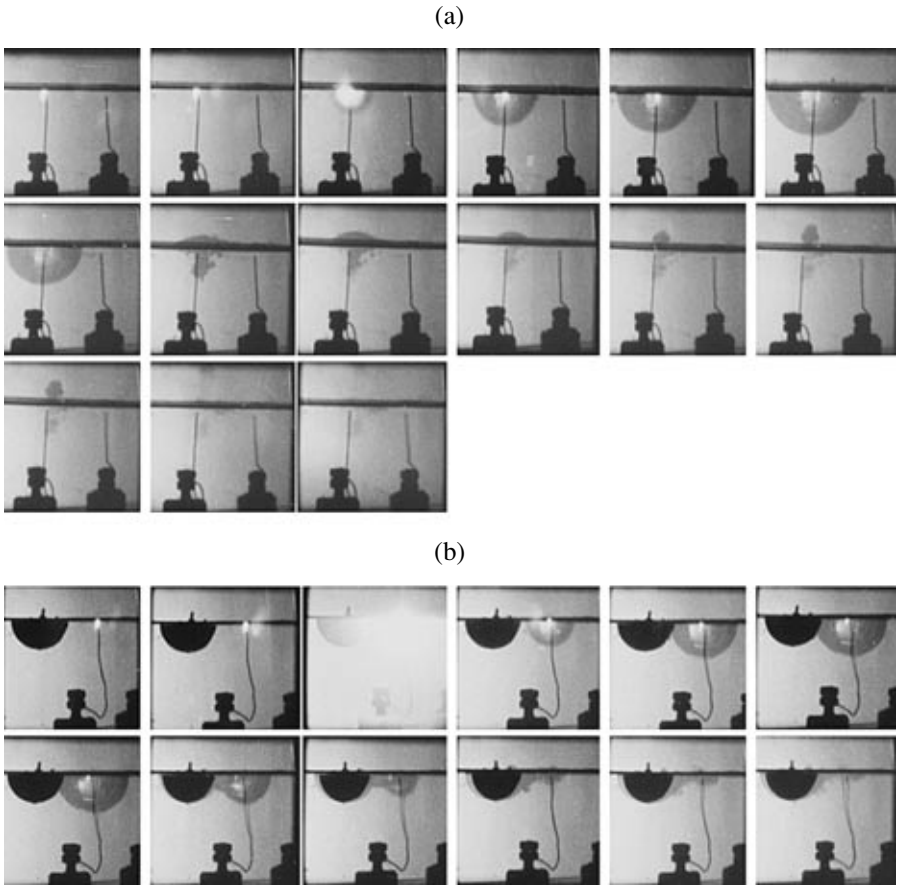

Fig. 6. Minimization of cavitation region between thin rod-type electrodes at individual discharges: (a) parallel rods; (b) a solid hollow hemisphere is placed in the imaginary center of generation of the second post-discharge cavity.

charge gap was initially closed with a copper wire with a diameter d of 5 μm, and the interelectrode spacing A was 100 mm.

The electrodes (d_e = 3 mm) were made of titanium wire and, apart from their primary function, served to indicate the appearance of the lower pressure (appearance of tensile stresses in water) by deflecting in the direction of the lower pressure region.

With the aim of assessing the relationship between the variation in working voltage and the cavitation region, the voltage was decreased by a factor of 1.4, i.e., up to U_1 = 17.8 KV (for a constant pulse energy magnitude).

All the stages of the genesis of the parallel electrical discharges in water were registered using a high-speed VFU-1 optical filming system in the "time magnifying" regime. The time intervals between the frames in the film records shown here was mt = 1.28 ms.

Photographic images that show the genesis and evolution of the cavitation region in water generated by two interacting parallel discharges are presented in Fig. 4. The images shown in Fig. 4a correspond to discharges produced strictly in a synchronous manner ((t = 0), the images shown in Fig. 4b correspond to the case where one of the discharges was initiated at a very short time interval delay (Δt = 2 μs).

The first photographic image (see Fig. 4a) shows that both the post-discharge cavities are developing symmetrically and weakly influence each other at the stage of active growth. They do not change their shape, which retains its regular character. The pressure field in the interelectrode gap remains symmetrical (the electrodes remain parallel) up to the moment when the vapor and gas cavities reach their maximal dimensions (frames 1–7). But exactly at the moment when the collapse of the post-discharge cavities begins, a region of lower pressure arises in the water between the parallel electrodes; the electrodes deflect toward the center of the interelectrode gap (frame 8), and actual cavitation is initiated, which evolves strictly between the electrodes (frames 8–14). The cavitation index in this region is rather large ($K \approx 0.7$).

The second photographic image (Fig. 4b) shows that even a small break in the synchronous character of the parallel discharges results in obviously asymmetric development of the cavitation region, although only small changes in its volume, as well as the cavitation index, occur. Electrodes operating as indicators of the decrease in pressure clearly register (frames 8–11) the presence of the lower pressure region in the interelectrode gap. But the lower pressure region exists over a noticeably shorter time (3.84 ms compared with 8.96 ms for the strictly synchronous regime).

The photographic images in Fig. 5 show the initiation and evolution of a cavitation region in the water generated by two interacting parallel discharges under substantially modified conditions. Fig. 5a corresponds to discharges, where the initiation of one of the discharges is delayed for a substantial time interval (Δt = 8 μs), while Fig. 5b corresponds to discharges with U_1 = 17.8 KV produced strictly synchronously ($\Delta t = 0$).

When the initial stages of the discharges are significantly asynchronous (Fig. 5a), the dimensions of the post-discharge cavities differ dramatically (frames 1–7). This leads to their asymmetrical contraction, a decrease in pressure lowering in the interelectrode gap, and, consequently, to an asymmetrical shape of the cavitation region (frames 8–14) with considerably less density of cavitation bubbles ($K \approx 0.2$) that degrades rapidly (frames 11–14).

When the working voltage decreases to U_1 = 17.8 KV, the magnitude of tension stresses in the interelectrode gap decreases, even if the discharges follow strictly synchronously (frames 1–10). The volume of the cavitation region and the cavitation intensity (cavitation index $K \approx 0.4$) also decrease.

The photographic images in Fig. 6 show the genesis and evolution of a cavitation region in the water that is generated by individual discharges under substantially modified conditions. Figure 6a corresponds to discharge in parallel electrode systems; however, the second discharge is excluded. Fig. 6b also corresponds to the discharge in parallel electrode systems, where the second discharge is excluded, but a solid hollow hemisphere whose dimensions are the same as those of the corresponding post-discharge cavity is inserted into the discharge region.

As may be seen in the photographic image in Fig. 6a, even a well-developing individual underwater discharge (in the parallel electrode system discussed above) does not lead to the excitation of a noticeable cavitation region. Only a slight cavitation appears near the electrode tip after the collapse of the post-discharge hemisphere (frames 8–13). In this region the cavitation index is $K \approx 0.5$.

For the case where a solid hollow hemisphere is inserted near an individual underwater discharge, whose dimensions are the same as the averaged dimensions of the post-discharge cavity of the parallel discharge, the cavitation situation differs substantially from the cavitation for a free individual discharge. As soon as the post-discharge cavity, having reached its maximal dimensions, begins to collapse (frame 8), the surrounding liquid flows into it with a speed high enough to excite cavitation in the liquid layers adjacent to the hemisphere. A part of this liquid stream enters the region of the collapsed post-discharge hemispherical cavity (frames 9–12) also forming a small cavitation region centered in the discharge gap.

Quantities of cavitation bubbles are also simultaneously generated in water layers adjoining the entire surface of the solid hemisphere (frames 8–14).

It should be noted, that when the post-discharge cavity expands sufficiently fast, the diverging liquid streams do not generate cavitation near the solid hemisphere (frames 4–7). This occurs because the liquid in these streams is compressed, and there are no any tensile stresses in it.

As a whole, the liquid volume where the cavitation process takes place upon individual discharge and with a hemispherical imitator is comparable with the cavitation volume that occurs with a free linear discharge, although the shape and geometry of this cavitation region better suits the requirements for practical applications.

CONCLUSIONS

The experimental results obtained allow us to conclude that in a free volume only parallel underwater electrical discharges generate high-power cavitation regions.

The cavitation intensity in such regions strongly depends on the synchronization of the initiation of parallel discharges and their corresponding post-discharge vapor and gas cavities, as well as on the magnitude of the working voltage in the discharge circuits. Hence, the electrical discharge cavitation described above is a controllable process.

Individual electrical discharges with exactly the same energy parameters do not lead to the generation of high-power cavitation regions.

REFERENCES

1. Malyushevskii, P.P., Malyushevskaya, A.P., and Levda, V.I., Nonlinear Electrodetonative Bulk Cavitation in Process Reactors. Part 1. Electrical Discharge Gener-

ation of Gas Phase as Cavitation Nucleus, *Elektron. Obrab. Mater.*, 2004, no. 1, pp. 46–53.

2. Malyushevskii, P.P., Malyushevskaya, A.P., and Levda, V.I., Nonlinear Electrodetonative Bulk Cavitation in Process Reactors. Part 2. Analysis of the Structure of the Cavitation Regions, *Elektron. Obrab. Mater.*, 2004, no. 2, pp. 40–46.
3. Malyushevskii, P.P., Gorovenko, G.G., and Petyur, L.G., Combining Underwater Electrical Detonation and Embedded Hydroacoustic Transducer. Part 1. (Investigation of Physical Efficiency of Pulsed Acoustic Field Generation, *Elektron. Obrab. Mater.*, 2003, no. 2, pp. 68–75.
4. Malyushevskii, P.P., Petyur, L.G., and Kataev, N.M., Some Anomalous Characteristics of an Acoustic Pulse Emitted from the Region of Interaction of Three Converging Shock Waves, *Elektron. Obrab. Mater.*, 1996, no. 2, pp. 40–42.
5. Malyushevskii, P.P., *Osnovy razryadno-impul'snoi tekhnologii* (Fundamentals of Pulse-Disharge Technology), Kiev: Naukova Dumka, 1983.
6. Vovchenko, A.I., Kucherenko, V.V., and Shamko, V.V., Characteristic Features of Space–Time Evolution of Vapor and Gas Cavities Generated by Underwater Electrical Discharge, *Zhurn. Prikl. Mekhan. Tekh. Fiz.*, 1978, pp. 58–64.

ISSN 1068-3755, Surface Engineering and Applied Electrochemistry, 2007, Vol. 43, No. 1, pp. 65–67. © Allerton Press, Inc., 2007.

OPERATING EXPERIENCE

Experimental Research on Ultrasonic Softening in Cold-Rolled Steel Strips[1]

M. M. Susan[a], P. G. Dumitras[b], and V. G. Iliescu[c]

[a] *Gh. Asachi Technical University, Bd. D. Mangeron 63, 700050, Iasi, Romania*

[b] *Institute of Applied Physics, Academy of Sciences of the Republic Moldova, ul. Academiei 5, Chisinau, MD-2028, the Republic of Moldova*

[c] *S.C. Cablero S.A., Iasi, Romania*

Received June 1, 2006

Abstract—The possibility of obtaining the effect of ultrasonic softening through laboratory experiments in hardened cold-rolled steel strips has been shown. The rolling of metal strips using ultrasonic activation is promising for increasing the deformation degree in comparison with conventional rolling as well as for the growth of the rolling rate, which supposes greater productivities.

DOI: 10.3103/S1068375507010115

1. INTRODUCTION

Ultrasound of high energy produces two major effects in metals, which influence their mechanical and structural properties: an ultrasonic softening and ultrasonic hardening. Ultrasonic softening may be observed during ultrasonic activation, and it appears due to a reduction in the external static strains needed for plastic deformation. Ultrasonic hardening may be considered as a residual effect after ultrasonic activation [1, 2]. This effect occurs due to the growth of external static strains needed for the plastic deformation of metals. The effects that appear at ultrasonic activation in metals were studied previously.

B. Langenecker and other researchers consider ultrasonic softening and ultrasonic hardening in metals as "volume effects," because they take place in the metal volume under the action of ultrasonic waves. In Langenecker's theory, these processes occur due to ultrasound that produces in metals components of a tangential strain large enough to move dislocations from their positions blocked by obstacles and forward through the crystal.

It is thought that the ultrasonic action leads to hardening in soft crystals up to a certain saturation value, after which the hardened crystals become softer.

The success of softening technology for the treatment of metal products in a hardened state depends on the ultrasound intensity or the amount of energy induced in the metal. The ultrasonic energy must be high enough to produce modifications in the adjacent structure. Therefore, high-energy ultrasound should be used. While propagating through a metal, ultrasound leads to an interaction with the crystal lattice and lattice defects. This supposes different absorption of the vibrational amplitude of ultrasonic waves.

At very small amplitudes (Fig. 1, region I), there is no irreversible deformation in the medium through which ultrasound propagates, but only some minor losses occur due to the absorption of ultrasonic waves.

This happens in the case of passive actions: determining different physical properties, flaw detection, etc. For small amplitudes (region II), a softening process takes place; then, in the case of large amplitudes, a hardening process occurs, when a linear dependence is observed for the absorption vs. the length of the region activated by ultrasound [3].

The purpose of the work is to assess the possibility of obtaining the effect of ultrasonic softening in cold-rolled (hardened) metal strips through laboratory experiment. The hardened steel strips were subjected to ultrasonic action in the rolling process. Four rolls were used in the rolling process simulation.

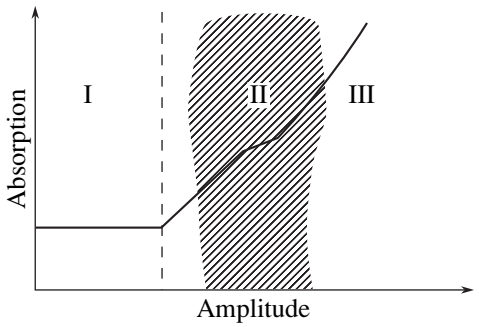

Fig. 1. Ultrasound absorption in metals.

[1] The text was submitted by the authors in English.

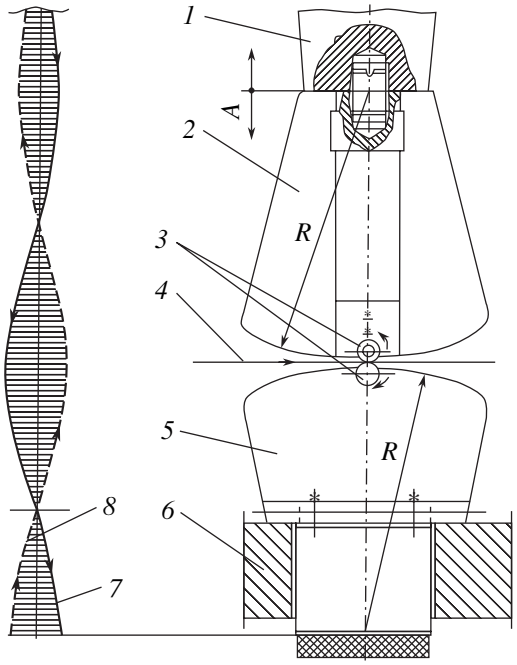

Fig. 2. Scheme of the metal strip rolling with ultrasonic activation. *1*—transductor PMS 15A-18; *2*, *5*—segments of back-up rolls; *3*—workings rolls; *4*—metal strip; *6*—fastening element; *7*—forward wave; *8*—backward wave.

The obtained results have been estimated through a comparative study of test bars sampled from a steel strip hardened and worked with ultrasound using the tensile strength test according to STAS SR.EN 10002-1/1995.

2. INVESTIGATION METHOD AND EXPERIMENTAL RESULTS

For testing, cold-rolled strips were used hardened according to OL 60-STAS 500/2 (St6/GOST 380)–88, with cross-sectional dimensions of 31.5 mm × 1.0 mm and the following values for the mechanical parameters: metal flow limit $R_{p0.2}$ = 996 MPa, tensile strength R_m = 1090 Mpa, and elongation A_{80} = 1.80%. The rolling of the metallic strip with ultrasonic activation was performed according to the scheme (Fig. 2).

Vibrations of the working upper roll are produced that activate the segment roll 2 using a PMS 15A-18 transductor, whose active part consists of the pack of nickel plates fed with a high-frequency current from a UZ G2-4M ultrasound generator. We obtain the different values of vibrational amplitude (10, 15, and 20 μm) through the variation of a magnetization current in the oscillatory system.

The dimensioning of the oscillatory system is characterized in the "$n\lambda/2$" scale, when the resonant frequency is 18 000 Hz. The rolling rate of the metal strip (ν_r) is 5 m/min. For the given testing conditions, the strip cross section reduces by 10% at the activation of the upper roll transversely to the rolling direction.

The vibrational amplitude can be controlled using a special device, which includes "a microphone with electret" (with capacitor functions) as the activating element [4].

Rolling with ultrasonic activation was performed for three different values of the vibrational amplitude of the upper working roll: US_1, A = 10 μm; US_2, A = 15 μm; and US_3, A = 20 μm.

An assessment of the results obtained was made through the comparative study of the test bars sampled from the hardened and treated with ultrasound strips for three values of the vibrational amplitude using the tensile strength test according to STAS 1002-1/1995.

The tensile strength test was carried out in a special computer-aided MTS 810-24 installation, accuracy class 0.5, with the extension rate of the test bars 20 MPa/s. To determine the elongation A_{80}, a digital MTS 810-24 extensometer was used, accuracy class B1. For the test bars sampled from cold-rolled strips, initial stage "0," it was found out that breaking is achieved at very small extensions, which proves their hardened state.

In the ultrasonic activation process for the three aforementioned working conditions US_1, US_2, and US_3, the ultrasonic softening effect was studied as a function of vibrational amplitude (Fig. 3). Great ultrasonic softening was obtained for A = 5 μm; the effect was less for A = 10 μm, but for A = 20 μm, the extension was much smaller than for A = 15 μm, although the vibrational

Table

No.	Test bar symbol	Technological characteristics		Mechanical characteristics						Obsv.
		V_r, m/min	A, μm	$R_{p0.2}$, MPa	$\Delta R_{p0.2}$, %	R_m, MPa	ΔR_m, %	A_{80}, %	ΔA_{80}, %	
1	0	5	–	996	–	1090	–	1.28	–	Hardened stage
2	US_1	5	10	910	8.63	990	9.17	2.20	41.81	Softening process
3	US_2	5	15	899	9.73	987	9.44	3.20	60.0	Greater softening
4	US_3	5	20	926	7.02	1006	7.70	2.40	46.6	Ultrasonic softening and hardening

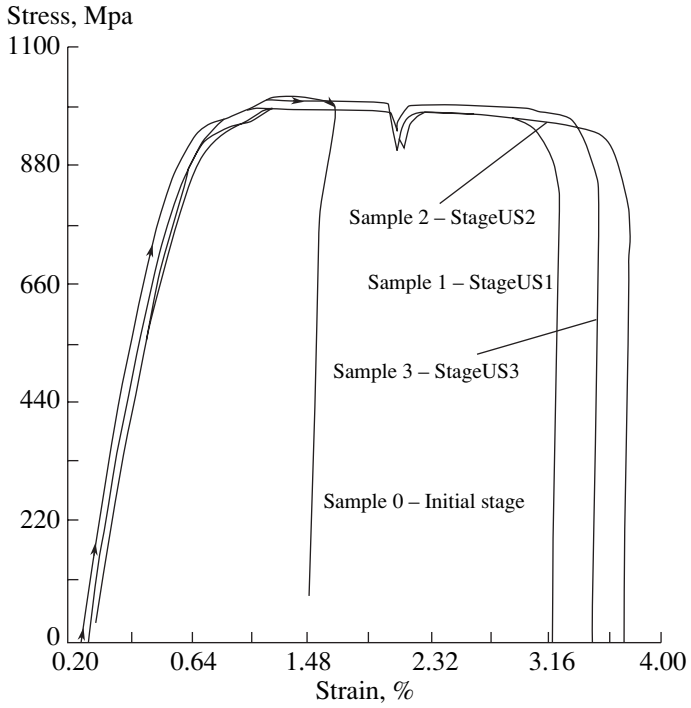

Fig. 3. Stress–strain diagram.

amplitude increases. This gives evidence that, for the working condition US_3, the vibrational amplitude is too large for the speed of motion of the metal strip, which is 5 m/min. That is, besides the softening effects, the ultrasonic hardening process also occurs.

It was found out that the rolling rate has to grow proportionally to the vibrational amplitude. That is why, in the authors' opinion, it is possible to perform the rolling with ultrasonic activation with much greater rates than conventional processing. In this case, there is the dependence between the vibrational rate (ν_v) and the rolling rate of the metal strip (ν_r).

The ratio (ν_r/ν_v) may be used as an optimization criterion for the given rolling process. Variation of mechanical characteristics $R_{p0.2}$, R_m, and A_{80} can be determined according to the following relationship (an example for R_m is given): $R_m = [(R_{m0} - R_{mUS1,2,3})/R_{m0}] \times 100\%$. Experimental results are summarized in the table.

3. CONCLUSIONS

Laboratory experiments have demonstrated the possibility of obtaining the ultrasonic softening effect in previously hardened cold-rolled steel strips. The process passes under the influence of ultrasonic energy through the several stages: hardening, softening, and, possibly, a new hardening depending upon the amount of the energy induced in the metal and on the vibrational amplitude of the deformation tool. The rolling of metal strips with ultrasonic activation is promising in terms of the increase of the deformation degree and the rolling rate in comparison with conventional rolling, providing much greater productivity.

For the potential application of this method on a large scale, it is necessary to continue experiments through the development of basic and applied research.

REFERENCES

1. Dragan, O., et al., *Ultrasound of High Energy*, Bucuresti: Editura Academiei, 1983 [in Romanian].
2. Susan, M., et al., *Special Plastic Working*, Iasi: Editura "Gh. Asachi," 2000 [in Romanian].
3. Kralik G. and Weiss, B., Über die Ultraschallverfestigung von Kubisch flachenzentrierten Metallen and Legirungen, *Zeitschrift fur Melall-Kunde*, 1967, vol. 58, no. 7, pp. 471–475.
4. Susan, M., Research Concerning Steel Ball Bearing Wire Drawing in an Ultrasonic Field, *PhD Thesis*, Iasi: Asachi Technical University, 1996 [in Romanian].

ISSN 1068-3755, Surface Engineering and Applied Electrochemistry, 2007, Vol. 43, No. 1, pp. 68–71. © Allerton Press, Inc., 2007.
Original Russian Text © A.A. Aliev, 2007, published in Elektronnaya Obrabotka Materialov, 2007, Vol. 43, No. 1, pp. 84–87.

OPERATING EXPERIENCE

The Effect of Electric Discharges on Polyolefin Compositions in the Region of Small Admixtures of One of the Components

A. A. Aliev

Institute of Radiation Problems, National Academy of Sciences of Azerbaijan, ul. F. Agaeva 9, Baku, Az 1143 Republic of Azerbaijan

Received June 21, 2006

DOI: 10.3103/S1068375507010127

INTRODUCTION

One of the reasons for the breakdown of high-voltage insulation is related to the development of electric discharges in sites that contain gas inclusions [1]. A second reason is related to the onset and development of a partial breakdown in segments where the channel field is strongly nonuniform. Such a breakdown develops under the long-term effect of an electric field, i.e., dendrites and treeing, resulting in gradual loss (erosion) of the material, as well as to local reduction in its thickness and, eventually, in complete breakdown.

Therefore, to increase the service life of plastic high-voltage insulation, a material is needed that is characterized by a continuous structure (with a minimum number of gas inclusions and nonuniformity areas) and resistance to the effect of electric discharges.

Recently, researchers have been turning their attention to polymer mixtures. The produced materials exhibit a set of new properties that the original plastics do not possess [2].

Polypropylene–polyethylene (PPPE) mixtures have been actively studied with the aim of increasing the impact resistance of polypropylene (PP), reducing its temperature, brittleness, etc.; however, information on studies of PPPE mixtures is almost nonexistent.

The properties of plastic mixtures whose components do not chemically interact with each other significantly depend on the mixture structure. The latter is determined, in turn, by the relative concentrations of the components. If the content of one component in the matrix of another component increases, the mixture structure sequentially passes through a number of stages: solution, interphase solution region, disperse microheterogeneous structure, coagulation net, and inversion structure [3, 4].

One may assume that the mechanism of disintegration of polymer mixtures under the effect of external factors will also essentially depend on the relative concentration of the mixture components.

EXPERIMENTAL

The study was devoted to electric ageing of films made of PPPE mixtures in the range of small concentrations (up to 5–10 wt %) of one of the components. The PPPE mixtures were made from uninhibited isotactic PP powder (weight-average molecular weight $\overline{M}_\omega = 2.86 \times 10^5$ and number-average molecular weight $\overline{M}_n = 6.23 \times 10^4$; $\overline{M}_\omega / \overline{M}_n = 4.6$; degree of crystallinity $\chi = 64$) and PE powder (weight-average molecular weight $\overline{M}_\omega = 4.15 \times 10^4$ and number-average molecular weight $\overline{M}_n = 2.71 \times 10^4$; $\overline{M}_\omega / \overline{M}_n = 1.53$; degree of crystallinity $\chi = 49$) by grinding in a ball mill for 60 minutes. Afterward the mixture was passed through a microextruder with three controllable temperature zones (140, 160, and 190°C). The isotropic films were made by pressing the extrudate for 30 min at 200°C and a pressure of 200 atm on a polyimide-film substrate. The films were 100–120 μm thick. Immediately after pressing, the films were water tempered at 30°C.

The effect of electric discharges was studied in an asymmetric test cell consisting of a flat metallic electrode on which were placed a tested polymer-foil specimen, a 1.5-mm air slit, and a glass plate with the same thickness. High electric voltage (U = 9 kV) with the power-line frequency was applied to the external surface of the glass plate.

Before and after the electric test, the specimens were weighed with VLR-200 scales with an accuracy of up to 0.01 mg. The oxidation process was monitored via the carbonyl group ($C = 0$) band at 1720 cm^{-1} with a UK spectrophotometer. Electric strength E_{st} was determined for the current with the power-line frequency as a mean arithmetic value of ten independent measurements of the U_{br}/h ratio, where U_{br} is the breakdown voltage, which was increased with a rate of 1 kB/s, and h is the average thickness around the breakdown site. The tangent of the angle of dielectric losses

Table 1. Characteristics of PPPE polymer compositions

Characteristic	Specimen				
	PE	PE + 0.5%PP	PE + 1%PP	PE + 2%PP	PE + 5%PP
E_{st}, kV/mm	118	116	120	118	116
$\tan\delta \times 10^{-4}$	7	6	5	4	5
ε	2.2	2.4	2.8	2.9	2.7
$\log\rho_v(\Omega\,m)$	14.5	13.8	14.6	14.3	14.2

Table 2. Characteristics of polymer compositions after electric aging

Characteristic	Specimen				
	PE	PE + 0.5%PP	PE + 1%PP	PE + 2%PP	PE + 5%PP
E_{st}, kV/mm	43.0	38.0	60.0	64.0	32.0
$\tan\delta \times 10^{-4}$	95.0	80.0	26.0	32.0	78.0
ε	3.2	3.8	4.7	4.8	4.2
$\log\rho_v(\Omega\,m)$	9.3	9.5	11.6	10.6	9.4
Δm, mg	7.5	6.6	0.9	0.9	14.8
$\Delta D_c = 0$	3.8	3.6	0.03	0.02	1.5

(tanδ) and capacity of foils ε were measured with an R-589 bridge.

RESULTS AND DISCUSSION

Table 1 contains results of the tests of polymer PPPE compositions. One can see that addition of PP (in an amount of 0–5%) to PE results only in insignificant changes in the electric characteristics of the obtained compositions.

Polyethylene and polypropylene are incompatible polymers. PE crystallizes into a more stable orthorhombic lattice, and PP, into a monoclinic form. However, both components affect the process of crystallization and formation of a low-molecular structure [5, 6].

Addition of small (1–2 wt %) amounts of PP to PE increases the resistance of the latter polymer to erosion and oxidation caused by the effect of electric discharges (Fig. 1 and Table 2).

PP is known to be less resistant to the effect of electric discharges than PE, this feature being explained by the presence of tertiary carbon atoms in the polymer's macromolecules. Indeed, over 20 hours of electric ageing in the conditions described above, the mass loss for "pure" PP was 20 mg and for "pure" PE it was only 8 mg. One might assume that addition of PE to PP should have increased the resistance of the latter polymer to the effect of electric discharges, and addition of PP to PE should have had the opposite effect; however, none of the expected phenomena has been observed in the range of small addition amounts. The extreme behavior of the mass loss and oxidation rate in the ranges of PE addition to PE of 0.5–1 wt % and 1–2% may be explained by hypothesizing existence of an interphase layer.

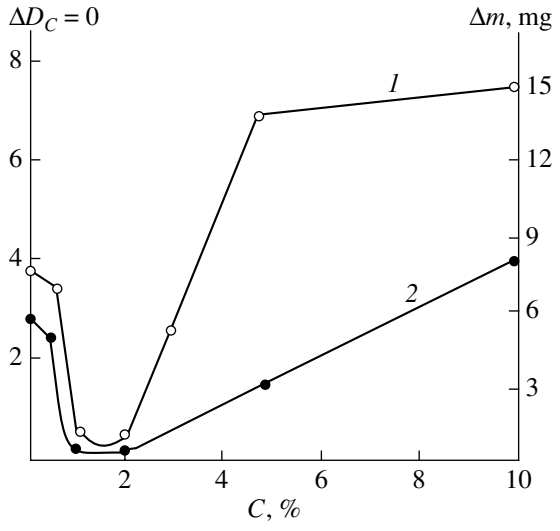

Fig. 1. Mass loss Δm(*1*) and (*2*) degree of oxidation of PE specimens as a function of PP content. $U_{ag} = 9$ kV; $t_{ag} = 20$ h.

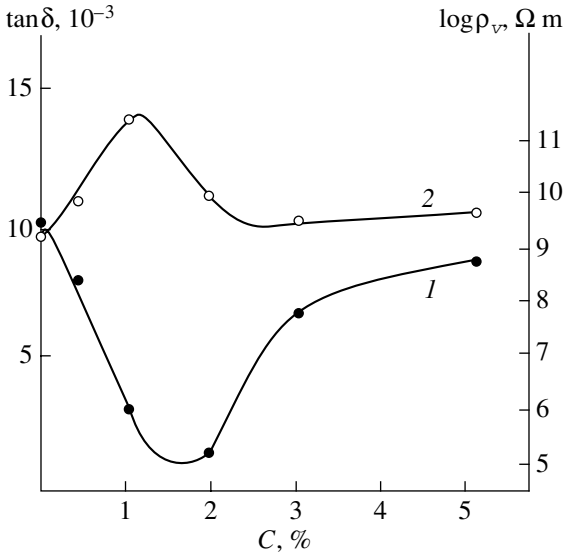

Fig. 2. Variation of the tangent of dielectric-loss angle tanδ (*1*) and $\log\rho_v$, (*2*) of PE specimens as a function of PP content.

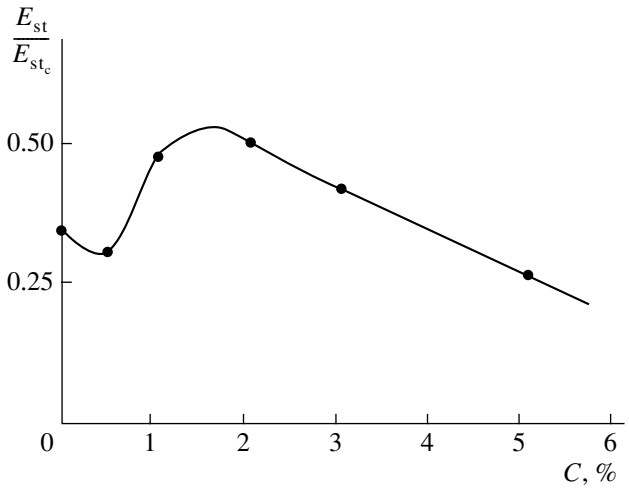

Fig. 3. Dependence of electric strength E_{st} of PE specimens with different content of PP. U_{ag} = 9 kV; t_{ag} = 10 h.

According to [7, 8], the extreme behavior of the changes in the properties of polymer compositions in the range of vary small additions of one of the components (modifier) is explained by layering of the polymeric solution for a certain content of the modifier, separation of the modifier into a disperse phase, and formation of an interphase layer with specific properties. The modifier may form a reinforcing frame or fill the structure defects of a polymer matrix; i.e., it may ensure a finer and single-phase structure of that matrix or, on the contrary, loosen the matrix's structure and increase the content of defects.

Thus, if small quantities of PP are added to PE, the free volume decreases; the interphase layer becomes denser, and resistance to electric ageing reaches a maximum (Table 2).

These phenomena are indicated by a steep increase in the volume resistivity of polyethylene foils after addition of 1–2 volume (weight) percent of polypropylene, as well as by a decrease in the tangent of the angle of electric losses of PE foils containing a PP additive (Fig. 2, curve *1* and *2*).

At the moment of interphase layering, a large number of modifier particles with small dimensions appear and the interphase layer reaches a maximum. If the modifier content increases further, the particle dimensions grow; their concentration decreases, and the interphase layer shrinks. Indeed, if, in the case considered, the PP concentration in PP exceeded 1 wt %, a sharp decrease in oxidation and mass loss under the effect of particle discharges, as well as an increase in electric strength, was observed (Fig. 3) [9].

The experiments reconfirm the assumptions made above according to which for all mixtures of polymers in two-, three-, or multicomponent systems (whether compatible or not), there is a modifier fraction (0–100 wt %) that results in a steep, collapselike change in the structure and electrophysical properties of the system that may either become better or worse [10, 11].

It should be noted that studies of polymer mixtures, including polymer composites, which are of great importance for science and practice, enable the creation of new polymer materials that exhibit valuable properties without the need to develop new, expensive technologies.

REFERENCES

1. Bagirov, M.A. and Malin, V.P., *Elektricheskoe starenie polimernykh dielektrikov* (Electric Ageing of Polymer Dielectrics), Baku: Azerneshr, 1987.
2. Popov, A.A., Gusak, A.V., Gladilin, M.P., and Zaikov, G.Ye., Mixture Compositions of High-Strength Polypropylene and Polyethylene. Properties of Isotropic Specimens, *Vysokomol. Soed.*, 1986, vol. A28, no. 5, pp. 1083–1088.
3. Lipatov, Yu.S., *Kolloidnaya khimiya polimerov* (Colloid Chemistry of Polymers), Kiev: Naukova Dumka, 1984.
4. Kuleznev, V.I., *Smesi polimerov* (Polymer Compositions), Moscow: Khimiya, 1984.
5. Aliev, A.A., An Effect of the Content of PPPE Polyolefin Compositions on the Structure and Electric Properties of Polymer Compositions, *Bilqi*, 2003, no. 3, pp. 9–14.
6. Kerimov, M.K. and Aliev, A.A., Polymer Mixtures and Composites, *Dokl. NAN Azerbaijan*, 2003, vol. 59, nos. 3–4, pp. 55–67.

7. Lipatov, Yu.S. and Lebedev, Ye.V., Colloidal and Chemical Specific Properties of Polymer-Polymer Systems, *Physical and Chemical Mechanics and Lyophilic Property of Disperse System*, *Respubl. Mezhved. Sb.*, Kiev: Naukova Dumka, 1982, no. 14, pp. 3–13.

8. Kuleznev, V.N., Klykova, V.D., et al., Behavior of Binary Polymer Mixtures in the Area of Phase Separation, in *Fiziko-khimicheskaya mekhanika i liofil'nost' dispersnykh system* (Physical and Chemical Mechanics and Lyophilic Property of Disperse System), *Respubl. Mezhved. Sb.*, Kiev: Naukova Dumka, 1982, no. 4, pp. 14–20.

9. Aliev, A.A., Bagirov, M.A., Malin, V.P., Popov, A.A., and Guseinova, N.D., USSR Inventor's Certificate no. 1515203, 1989.

10. Aliev, A.A., Interphase Phenomena in Polymer Mixtures, *Bilqi*, 2004, no. 3, pp. 9–21.

11. Aliev, A.A., Electrets on the Basis of Polymers, Polymer Mixtures, and Composites, *Bilqi*, 2005, no. 2, pp. 15–29.

ISSN 1068-3755, Surface Engineering and Applied Electrochemistry, 2007, Vol. 43, No. 1, pp. 72–76. © Allerton Press, Inc., 2007.
Original Russian Text © B.E. Egamberdiev, B.Ch. Holliev, A.S. Mallaev, M.E. Zoirova, A. Eshonkhonov, 2007, published in Elektronnaya Obrabotka Materialov, 2007, Vol. 43, No. 1, pp. 88–92.

OPERATING EXPERIENCE

Obtaining Films of $CoSi_2$/Si (100) and the Analysis of Their Morphology and Stoichiometry through Molecular-Beam, Solid-Phase and Reactive Epitaxy Methods

B. E. Egamberdiev, B. Ch. Holliev, A. S. Mallaev, M. E. Zoirova, and A. Eshonkhonov

Tashkent State Technical University, ul. Universitetskaya 2, Tashkent 700095, Republic of Uzbekistan

Received July 29, 2006

Abstract—The results of studying the processes of thin $CoSi_2$ film formation on Si (100) surfaces by MBE, SPE, and RE methods are presented. The regularities of the initial stage of $CoSi_2$ film growth are studied. Stoichiometry of $CoSi_2$ film is analyzed by the Auger electron spectroscopy method. The results of investigation show strong dependence of the morphological and electrophysical properties of $CoSi_2$/Si (100) structures on the growth conditions. The measurements of the surface resistance show that the resistance of the $CoSi_2$ film grown at $T > 600$°C changes under different growth conditions.

DOI: 10.3103/S1068375507010139

At present, the problem of the formation of thin epitaxial metal layers on semiconductors with high perfection of the structure draws much attention among researchers. There exists a very restricted set of combinations of "metal semiconductors" allowing for the realization of the epitaxial growth of a metal film on a semiconductor substrate.

The study of epitaxial structures $CoSi_2$/Si and $NiSi_2$/Si is of great importance for understanding the electrophysical processes taking place at the metal-semiconductor interface, because these structures are the only ones for which theoretical expressions for the Schottky barrier height may be obtained directly from calculations based on atomic location in a real structure [1].

The practical application of epitaxial silicides in microelectronics is promising, first of all, for the design of a silicon-permeable base SHF transistor, the formation of the Schottky barriers, ohmic contacts, and interconnections of IC. The possibility of designing a photodiode with the Schottky barrier based on the $CoSi_2$/Si structure is very attractive.

The relevance of this work is connected with the existence of a number of unsolved problems from the viewpoint of both epitaxial growth technology and an understanding of the physics of growth and structure influence on the physical properties of silicide films, with their application opening new possibilities for the design of device structures with unique technical characteristics.

The further development of microelectronics requires new and unusual materials favoring an increase in the degree of microcircuit integration and functional electronics development. In this aspect, silicides are more promising.

The main aim of this work is to reveal the mechanisms of silicide structure formation at the molecular-beam epitaxy (MBE), solid-phase epitaxy (SPE), and reactive epitaxy (RE), and to obtain films, as well as morphology and stoichiometry. This paper presents the results of the investigation of $CoSi_2$/Si (100) epitaxial structures formed by the MBE, SPE, and RE methods. Layers of cobalt silicide were grown on substrates of the KEF-4,5, KDB-7,5, and KDB-12 types. The films were grown in an ultrahigh vacuum installation of MBE. Before the epitaxial growth, the substrate surface was subjected to chemical washing and special cleaning in a vacuum. The MBE installation and cleaning methods are described in detail in [2]. The thickness of the deposited cobalt in all cases was 100 Å, and a $CoSi_2$ film of thickness ~380 Å was formed as well. The processes of one-stage and two-stage growth were studied. At the two-stage growth, the film increase took place in two stages with different growth conditions.

At present, various methods of vacuum epitaxy of silicides on silicon are proposed. Among them, MBE, SPE, and SE should be mentioned. MBE is a simultaneous deposition of a metal and silicon from two beams on a heated silicon substrate. SPE is a metal deposition on a cleaned surface of silicon with subsequent heating to silicide formation temperatures. RE is a metal deposition on a heated silicon substrate.

Analysis of films grown by different methods shows that morphology and stoichiometry of the films crucially depend on the growth conditions.

Growth conditions, results of AES analysis of stoichiometry and morphology of the surface resistance of $CoSi_2$/Si (100) films

No.	Substrate type	h_{CoSi_2}, Å	Epitaxy type	T_s, °C	t_{ann}, min	Deposition rate, Å/s	I_{Co}/I_{Si}	$I_{Si}/I'_{Si\ II}$	θ	R_S, μΩ cm
1	KDB-7.5	105	RE	633	–	2	0.52	0.93	0.43	18
		105	RE	660	–	2				
2	KDB-7.5	210	TFE	575	5	2	0.47	0.88	0.87	25
3	KEF-4.5	210	TFE	610	7	2	0.54	0.87	0.83	25
4	KEF-4.5	105	RE	580	–	2	0.89	0.78	0.95	8
		105	RE	562	–	2				
5	KDB-12	210	TFE	630	7	2	0.65	0.94	0.29	23

Note: Designations: h_{CoSi_2} is the thickness of the cobalt layer deposited on substrates; T_s is the substrate temperature at epitaxy; t_{ann} is the time of structure annealing at SPE.

From the viewpoint of the morphology of $CoSi_2$/Si films, three main types can be found:

1) continuous films of $CoSi_2$;

2) films with microscopic holes; and,

3) discontinuous films.

In contrast, in $CoSi_2$ stoichiometry, two phases are distinguished [3]:

1) $CoSi_2$ enriched with silicon ($CoSi_2$–S); and,

2) $CoSi_2$ enriched with cobalt ($CoSi_2$–C).

Finding the relation between the morphology, stoichiometry, and growth conditions of $CoSi_2$/Si structures is very important for the design of device structures based on the given epitaxial layers. In most cases, the aim is to obtain maximally homogeneous layers; however, in a number of applications, the formation of films with submicron holes with controlled morphological characteristics is of interest. In [4], a method for the fabrication of a permeable-base transistor was proposed, wherein the role of holes in the metal base is played by natural submicron holes in the $CoSi_2$ film. The expression connecting the transistor current gain α and degree of covering θ in $CoSi_2$/Si system is proposed as

$$\alpha = \frac{\xi}{\gamma + \xi}, \quad (1)$$

where

$$\gamma = \frac{1 - \theta}{\theta},$$

$$\varepsilon = \kappa T / e\Delta_0 [\exp(e\Delta_0/kT) - 1].$$

Here, Δ_0 is the variation of the Schottky barrier value in the hole center ($\Delta_0 = f(x)$; x is the average diameter of the holes). Thus, by changing the conditions for $CoSi_2$ film growth, one can adjust values x and θ and, therefore, control the current gain α.

Stoichiometry of $CoSi_2$ films influences the electrophysical properties, the Schottky barrier height, and, in particular, resistivity.

The surface structure in the growth process was controlled by the method of high-energy electron diffraction (HEED) for reflection geometry. The grown samples were analyzed by Auger electron spectroscopy (AES). The surface resistance R_S was measured by the four-point probe method. Ratios of the intensities of Auger signals for cobalt and silicon in $CoSi_2$ film, as well as silicon in $CoSi_2$ and silicon of the substrate, were determined by the Auger profiles of the samples. The latter are shown in Fig. 1, while the conditions of silicide growth and analytical results are given in the table.

Taking the Auger spectroscopy data into account, an attempt was made to estimate the degree of substrate covering with cobalt silicide film. The expression connecting the intensities of the Auger signals of cobalt and silicon was obtained by

$$\theta = 3(1 - I_{Si}/I_{sin})I_{sin}/I_{Co}, \quad (2)$$

where I_{Co} is the intensity of the cobalt Auger signal in $CoSi_2$ (765 eV), I_{Si} is the intensity of the silicon Auger signal in $CoSi_2$ (91 eV), and I_{sin} is the intensity of silicon Auger signal in the substrate (91 eV).

The values of the ratios of the intensities I_{Co}/I_{Si} and I_{Si}/I_{sin}, as well as the value θ calculated by formula (2), are given in the table.

It should be noted that formula (2) was obtained on the basis of very rough approximations; in particular, stoichiometry variation does not destroy the bulk (and surface) density of atoms (i.e., when the stoichiometry is broken, a substitution of atoms of one type by others takes place in the crystal lattice sites, while the probability of the atomic presence in interstitial sites is not taken in account). Thus, in the case of the samples *a* and *e*, the formula obviously gives underestimated values of the degree of covering. On the other hand, the lower value of sample *e* is confirmed by the HEED data. Besides reflexes from the $CoSi_2$ single crystal surface, the reflexes corresponding to the reconstructed surface of Si (100) 2×1 were observed on the diffraction pattern. This testifies to a significant area of the silicon

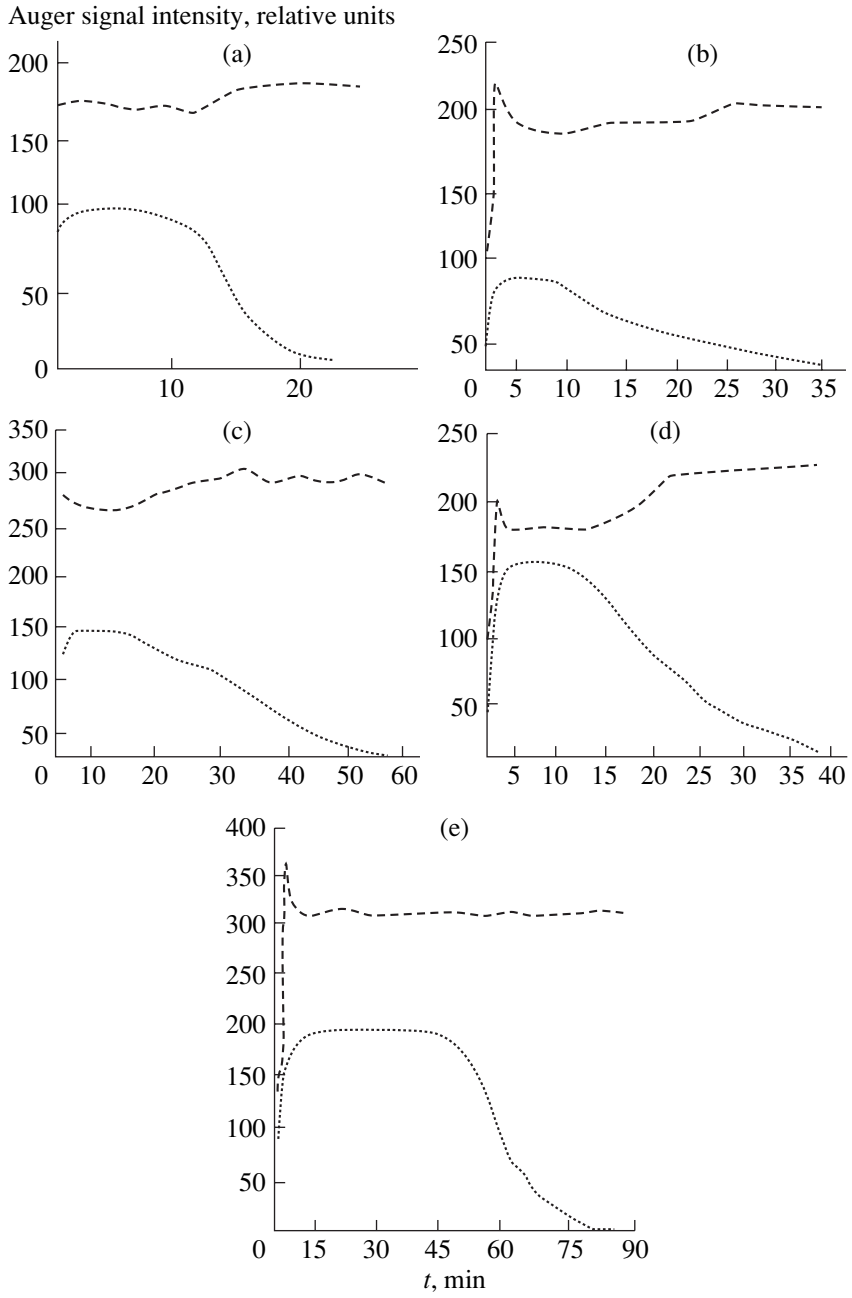

Fig. 1. Growth condition and Auger profiles of $CoSi_2$/Si samples (sample numbers 1–5 in the table correspond to the Auger profiles in Fig. 1).

substrate being free from the silicide film. Thus, formula (2) allows qualitative analysis of the degree of covering obtained under different growth conditions.

The Auger profiles (Fig. 1) testify to the formation of a thin layer of pure silicon on the surface of cobalt silicide under certain growth conditions. The given effect may be determined either by diffusion of cobalt atoms in the direction from the surface to the depth of the sample or by diffusion of silicon atoms from the substrate to the surface [5]. The first mechanism seems to be more probable. In any case, the silicon layer formation on the silicide surface is energetically advantageous, because the free surface energy of Si is less than that of $CoSi_2$. The formation of the pure silicon layer on $CoSi_2$ may be a useful effect in the fabrication of a transistor with a metal base, where it is necessary to grow a silicon epitaxial layer above the $CoSi_2$/Si structure. We found that, in this case, the presence of a thin buffer layer of silicon on the $CoSi_2$ surface improves the crystal perfection of the silicon epitaxial film. As seen from the profiles in Fig. 1, the layer of surface silicon is

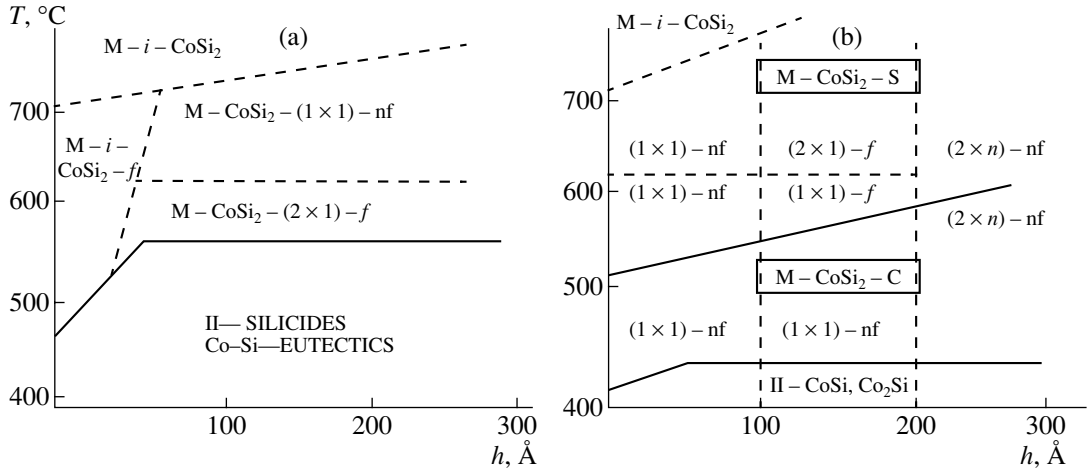

Fig. 2. Diagrams of the structure state of $CoSi_2$/Si (100) at BME (a) and SPE (b).

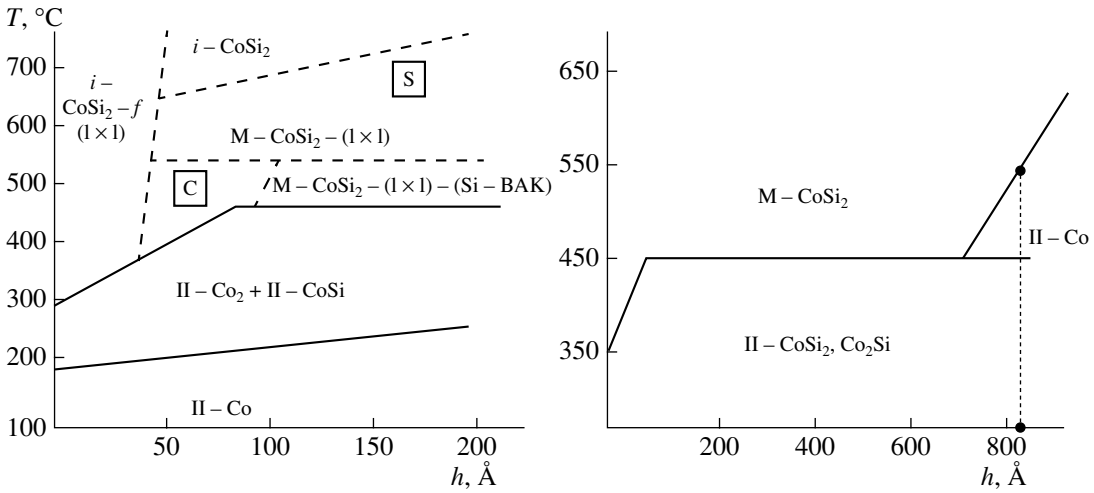

Fig. 3. Diagrams of the structure state of $CoSi_2$/Si (100) RE film.

formed only under certain growth conditions. Thus, there is a possibility of controlling this process.

Measurements of the surface resistance have shown that the growth of $CoSi_2$ films at $T > 600$°C (sample 4) results in a decrease in resistance by a factor of three. The AES data show that, under the given conditions, $CoSi_2$ enriched with cobalt, $CoSi_2$–C, is formed. The preferential formation of $CoSi_2$–C at low temperatures of reaction was also mentioned in [3]. The anomalously low value of the $CoSi_2$ resistivity (sample 4) indicates that the electric properties of the $CoSi_2$–C phase differ considerably from those of $CoSi_2$ and $CoSi_2$–S.

The classical diagrams of the Co–Si system state are considered in the reference book by Khansen [6]. The diagrams of the structure state of thin film systems $CoSi_2$/Si (100) formed by MBE, SPE, and RE are given in Figs. 2 and 3.

The structure identification was carried out using the HEED data. According to these diagrams, the intermetallic compounds $CoSi_2$ and CoSi are formed at temperatures above 1000°C. At the same time, the epitaxial growth of $CoSi_2$/Si films takes place at relatively low temperatures T_S = 400–600°C.

Divergence between the results on $CoSi_2$/Si epitaxy and the classical phase diagrams is explained by the following: (i) small thickness of films of Co and $CoSi_2$ at epitaxy; (ii) especially pure growth conditions, suggested by the formation of a pure Si surface, UHV processes, and the absence of intermediate layers on reacting surfaces decreasing the energy of activation of silicide formation process; and (iii) the single crystal character of silicon substrate.

The results of the investigations carried out show strong dependence of the morphological and electrophysical properties of the $CoSi_2$/Si structure on the growth conditions. Understanding of the regularities of cobalt silicide formation allows for the optimization of

the technological processes of the fabrication of concrete device structures.

REFERENCES

1. Tung, R.T. and Schreg, F., Epitaxial $CoSi_2$/Si (111) Interfaces, *Appl. Surf. Sci.*, 1989, vol. 41/42, pp. 223–229.
2. Egamberdiev, B.E., Electron-Spectroscopic Investigations of the Physical Properties of Epitaxial Combinations and Ion–Implanted Layers in Silicon, *Extended Abstract of Dr. Sci. (Phys.–Math.) Dissertation*, Tashkent, 2003.
3. Handerbache, L., et al., Identification of Three Distinct $CoSi_2$ (111) (1×1) Surface Structure, *Appl. Surf. Sci.*, 1989, vol. 41/42, pp. 257–261.
4. Tung, R.T, et al., Control of a Natural Permeable $CoSi_2$ Base Transistor, *Appl. Phys. Let.*, 1986, vol. 48, no. 10, pp. 635–637.
5. d'Heurle, F.M. and Thomas, O., Comment on Evidence for Si Diffusion through Epitaxial $NiSi_2$ Grown on Si (111), *Appl. Phys. Let.*, 1989, vol. 52, no. 26, pp. 2269–2272.
6. Khansen, M. and Anderko, R., *Struktury dvoinykh splavov* (Structures of Binary Alloys), Moscow: Metallurgizdat, 1962.